Structural architecture of mineralized veins in a Cenozoic orogenic gold deposit along the North Cycladic Detachment System, Greece

Laurence Hamel

Thesis submitted to the University of Ottawa in partial fulfillment of the requirements for the

Master of Science in Earth Sciences

Department of Earth and Environmental Sciences

Faculty of Sciences

University of Ottawa

Abstract

The Kallianos Au-Ag-Te deposit, a Cenozoic post-orogenic ore deposit on Evia island (NW Aegean Sea), is hosted in the high-pressure Cycladic Blueschist Unit (CBU). Whereas Cycladic ore deposits are broadly related to late Miocene granitoids, magmatism of this age is undocumented on southeastern Evia. Integrated field observations and isotopic data illustrate a connection between the structural architecture that hosts mineralization in the deposit and the regional stress field associated with a crustal-scale detachment, the North Cycladic Detachment System (NCDS), implying a first-order paragenetic relationship to post-orogenic extension. Mineralized and unmineralized veins occur alongside parallel faults and joints in two distinct orientations, each locally defining conjugate or en-echelon sets. Two younger sub-vertical tension gash sets (V_2, V_3) cross-cut older transposed and boudinaged mineralized veins (V_1) parallel to the metamorphic foliation. Sulfide mineralization is hosted in steeply-dipping, cm-scale qz ± cal ± ab V_3 veins. Structural relationships show clear cross-cutting of V_2 (NW-striking) by V_3 (NNW-striking). Veins of the deposit opened orthogonal to the NE-trending stretching lineations, synchronous with brittle-ductile shear bands that indicate top-NE kinematics, further demonstrating their relationship to crustal extension accommodated by the detachment system. Vein arrays developed within the brittle-ductile zone below the exposed detachment plane are parallel to those observed deeper in the footwall (within the deposit) and were likely induced by a coaxial strain component with maximum shortening perpendicular to the detachment plane. C-O isotope data from vein calcite ($\delta^{13}C$: -3.31-0.40‰ and $\delta^{18}O$: 14.43-20.78‰) reflect fluid mixing with the graphite-bearing CBU wall rock. White mica $^{40}Ar/^{39}Ar$ and in-situ $^{87}Rb/^{87}Sr$ geochronology suggests host rock greenschist facies deformation between c. 20-31 Ma, whereas vein halo hydrothermal mica reveals slightly younger fluid flow at c. 21-26 Ma, indicating vein formation occurred during the early Miocene. Zircon (U-Th)/He dates provide the timing of host rock cooling to <200°C at c. 11-14 Ma, corresponding to the exhumation of the deposit into the brittle crust. The comprehensive study of this younger, mostly undeformed post-orogenic deposit can help elucidate the structural controls of older polydeformed orogenic gold deposits.

Table of contents

Acknowledgements

Field work and analyses for this project were supported by an NSERC Discovery Grant awarded to D.A. Schneider, along with the Society of Economic Geologist Canada Foundation Student Research Grant and the Geological Society of America Graduate Student Research Grants awarded to L. Hamel. We thank A. Camacho (University of Manitoba), J. Metcalfe (University of Colorado Boulder), K. Larson (University of British Columbia-Okanagan), G. Poirier (University of Ottawa), P. Middlestead (University of Ottawa), E. Gomes-Reissmann (University of Ottawa), and A. Mauviel (University of Ottawa) for their assistance in sample preparation and data acquisition.

I would like to thank my thesis supervisor David Schneider for his incredible guidance throughout not only this thesis, but my undergrad as well. Thank you for the indispensable scientific and soft skill training and knowledge, as these will undoubtedly remain with me for the rest of my life. Additionally, thank you for the incredible opportunities you have offered me throughout the years.

A massive thank you to Taylor Ducharme for your mentorship (and patience) with me for this thesis. The skills and knowledge you have shared will certainly follow me throughout my career.

To the DAS group, I am eternally grateful for the talks, study breaks, travels and lifelong friendships.

Last, but definitely not least, I would like to thank my parents, family and partner for their unwavering, unconditional love and support throughout not only this thesis, but my entire academic career.

Introduction

Orogenic gold deposits are among the most productive styles of gold mineralization, and are distinguished by an intrinsic structural control on orebody geometry (Goldfarb et al., 2001; Goldfarb and Pitcairn 2023; Goldfarb and Groves, 2015; Groves et al., 1998; Groves et al., 2020; Lawley et al., 2023; Pettke et al., 1999; Phillips and Powell, 2010). Dominant ore-hosting structures are typically quartz (± carbonate) veins and subordinate faults and fractures, whose spatial distributions and orientations are often controlled by a crustal-scale fault or shear zone system. Gold is released principally via metamorphic devolatilization reactions and transported as sulphide complexes before being concentrated in shallower parts of the crust, typically within the brittle-ductile transition zone (Goldfarb et al., 2001; Goldfarb and Groves, 2015; Goldfarb and Pitcairn, 2023; Pettke et al., 1999; Phillips and Powell, 2010; Stüwe, 1998). The preferential localization of orogenic gold mineralization is likely due to availability of suitable structural or geochemical traps (Goldfarb et al., 2001; Goldfarb and Groves, 2015; Groves et al., 2020; Phillips and Powell, 1993, 2010; Powell et al., 1991; Stüwe, 1998). Some recent models envision orogenic gold mineralization as the product of remobilization spanning multiple generations of tectonometamorphic and related hydrothermal events over tens of millions of years (Henley et al., 1976; Lawley et al., 2020, 2023; Molnár et al., 2018; Stüwe et al., 1993). These studies emphasize that the reactivation of structures is crucial for concentrating gold within the traps. Consequently, post-orogenic collapse, which frequently exploits pre-existing syn-orogenic structures like thrusts and detachments, may be an important part of the orogenic cycle for generating deposits of this type (Bickford et al., 2005; Lawley et al., 2023; Phillips and Powell, 2010; Schneider et al., 2007).

The Cycladic islands in Greece host a variety of base and precious metal deposits generated during Hellenic orogenesis, including vein-hosted, epithermal, carbonate replacement, and skarn-

type, which together constitute the Cycladic Mineral District (CMD, Skarpelis, 2002; Voudouris et al. 2019; Wind et al., 2020). The islands expose remnants of previously subducted crust, the Attic-Cycladic Crystalline Belt (ACCB), which was exhumed as a result of extension accommodated by bivergent crustal-scale detachment faults (Gautier et al., 1993; Grasemann et al., 2012; Jolivet et al., 2010; Lister et al., 1984). Late Miocene plutons are spatially and temporally linked to these low-angle normal fault systems across the Cyclades, and this magmatism is genetically related to many of the deposits within the CMD (Berger et al., 2013; Ducoux et al., 2017; Menant et al., 2013; Scheffer et al., 2017).

The Kallianos Au-Ag-Te deposit, situated on the far southeastern part of Evia Island, is one example of an orogenic-style vein-hosted deposit (Figure 1). Similar to many deposits in the CMD, the Kallianos deposit formed during the Miocene within intercalated schists and marbles belonging to the high-pressure metamorphic nappe of the ACCB, the Cycladic Blueschist Unit (CBU; Latsoudas et al., 1997; Ring et al., 2007; Tombros et al., 2021; Xypolias et al., 2012). Whereas mining is currently inactive, the Kallianos area was intermittently mined for gold- and silver-rich ores until the 1940s (Tombros et al., 2021), with evidence of mining on southern Evia dating back to the 8th century BCE (Keller, 1984). The Kallianos deposit reportedly consists of numerous isolated vein- and fault-hosted occurrences spanning an area of 50 km^2, with grades up to 5-10 g/t Au, 40 g/t Ag, 2% Pb, 0.7% Zn, and 0.7% Cu, and an estimated mineral resource of 500,000 tonnes (Alexouli-Livaditi, 1978; Katsikatsos, 1978; Vavelidis and Michailidis, 1990; Tombros et al., 2021).

Paragenetic models highlight a complex, multi-stage development of the Kallianos deposit, including diverse sulphide mineral assemblages and accessory telluride mineralization (Tombros et al., 2021; Vavelidis and Michailidis, 1990; Voudouris et al., 2011). Recently, Tombros et al.

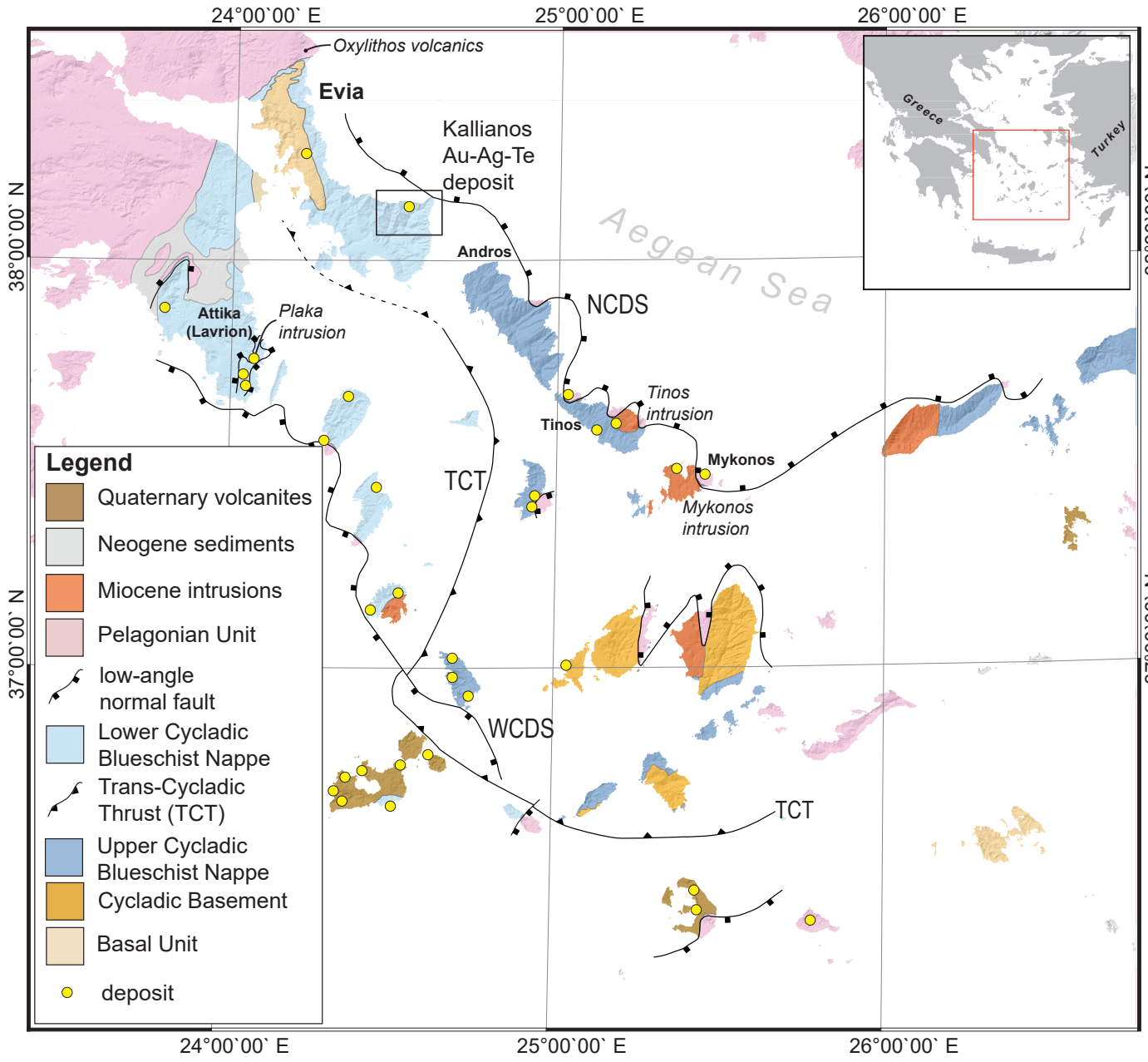

Figure 1. Simplified geological map of the Cyclades, Greece. Ore deposits (yellow circles) include epithermal, carbonate replacement, skarn, vein type and hydrothermal vent type deposits hosting Au, Pb, Zn, Bi, Te and other base metals; see summaries in Voudouris et al. (2019) and Wind et al. (2020). Black box indicates location of the study area (Figure 2). Modified after Ducharme et al. (2022) and Wind et al. (2020).

(2021) reported a vein-hosted pyrite $^{87}Rb/^{87}Sr$ date of c. 8 Ma from within the deposit, attributing a magmatic origin to the mineralizing fluids due to stable isotopic constraints and an overlap of the late Miocene pyrite age with the timing of regional plutonism. However, the apparent absence of Miocene plutons near the deposit required invoking fluid channeling from intrusions far afield (e.g., Lavrion, Tinos) along the structural architecture developed in relation to Miocene extensional detachment faulting (e.g., Jolivet et al., 2010; Grasemann et al., 2012; Tombros et al., 2021). The influence of these structures on Evia may extend considerably earlier, to at least c. 25 Ma (Ducharme et al., 2022, 2024; Jolivet and Patriat, 1999; Jolivet et al., 2010; Katzir et al., 2000; Shaked et al., 2000). Although substantial geochemical research has been conducted on the Kallianos deposit (Skarpelis, 2002; Tombros et al., 2021; Vavelidis and Michailidis, 1990; Voudouris et al., 2011; Wind et al., 2020), there is limited field-based investigation of its structural architecture. Here, we have conducted extensive field-based reconnaissance to better document the styles of deformation associated with the structural controls of the Kallianos Au-Ag-Te deposit. These structural data are compared with observations from an exposure of a major low-angle detachment fault on Evia, the North Cyclades Detachment System, whose record of brittle-ductile deformation is remarkably similar to that documented in the Kallianos deposit that occupies its footwall. New $^{40}Ar/^{39}Ar$ and $^{87}Rb/^{87}Sr$ dating, performed on host rock and vein-proximal white mica, indicate active hydrothermal systems and brittle-ductile vein formation since the early Miocene. Veins developed in the host rock that underwent brittle-ductile deformation, with lower age limits resolved by new zircon (U-Th)/He dates in the footwall and at the NCDS structurally above. These data, alongside new C- and O-stable isotope data from vein calcite, indicate a potentially earlier paragenesis for the Kallianos deposit that originated principally from interaction of metamorphic fluids with graphite-bearing marbles. This integrated approach refines the

structural architecture and paragenesis of the Kallianos Au-Ag-Te deposit, and provides a useful analogue with which to compare older, polydeformed orogenic gold deposits.

Geological setting

The Cycladic archipelago in the Aegean Sea exposes rock formed during the late Mesozoic to early Cenozoic Hellenic Orogeny through multiple cycles of ocean closure, microcontinent collision, and imbricate stacking of continental slivers (Figure 1; Doustos et al., 1993; Jacobshagen, 1986). Tectonism resulted in the formation of high-pressure/low-temperature (HP/LT) metamorphic rocks now exposed in the Cyclades, reaching peak metamorphic conditions of 10 kbar to 20 kbar and 400°C to 500°C during the late Paleocene to early Eocene (e.g., Grasemann et al., 2017; Jacobshagen, 1986). A two-step tectonic model has been established for the exhumation of the HP/LT rocks in the Cyclades, beginning with middle to late Eocene syn-orogenic wedge extrusion (Brichau et al., 2006; Ring and Layer, 2003). Subsequently, in the early Miocene, slab-rollback of the African plate created a back-arc setting (Jolivet and Faccenna, 2000; Rosenbaum et al., 2002). Widespread extension across the Aegean region caused crustal thinning accommodated by low-angle, bivergent regional-scale detachment systems that resulted in the exhumation of the once deep-seated rocks as metamorphic core complexes (Gautier et al., 1993; Grasemann et al., 2012; Jolivet et al., 2010; Lister et al., 1984).

One such structure, the North Cycladic Detachment System (NCDS), accommodated northeast-directed extension along several branches of ductile-then-brittle low-angle normal faults, spanning at least ~130 km between Samos and Evia (Figure 2, Jolivet et al., 2010). The NCDS is locally exposed throughout the northern Cyclades (Laurent et al., 2015; Mehl et al., 2005; Menant et al., 2013), which typically consist of metre-thick, shallowly-dipping mylonites, overprinted at

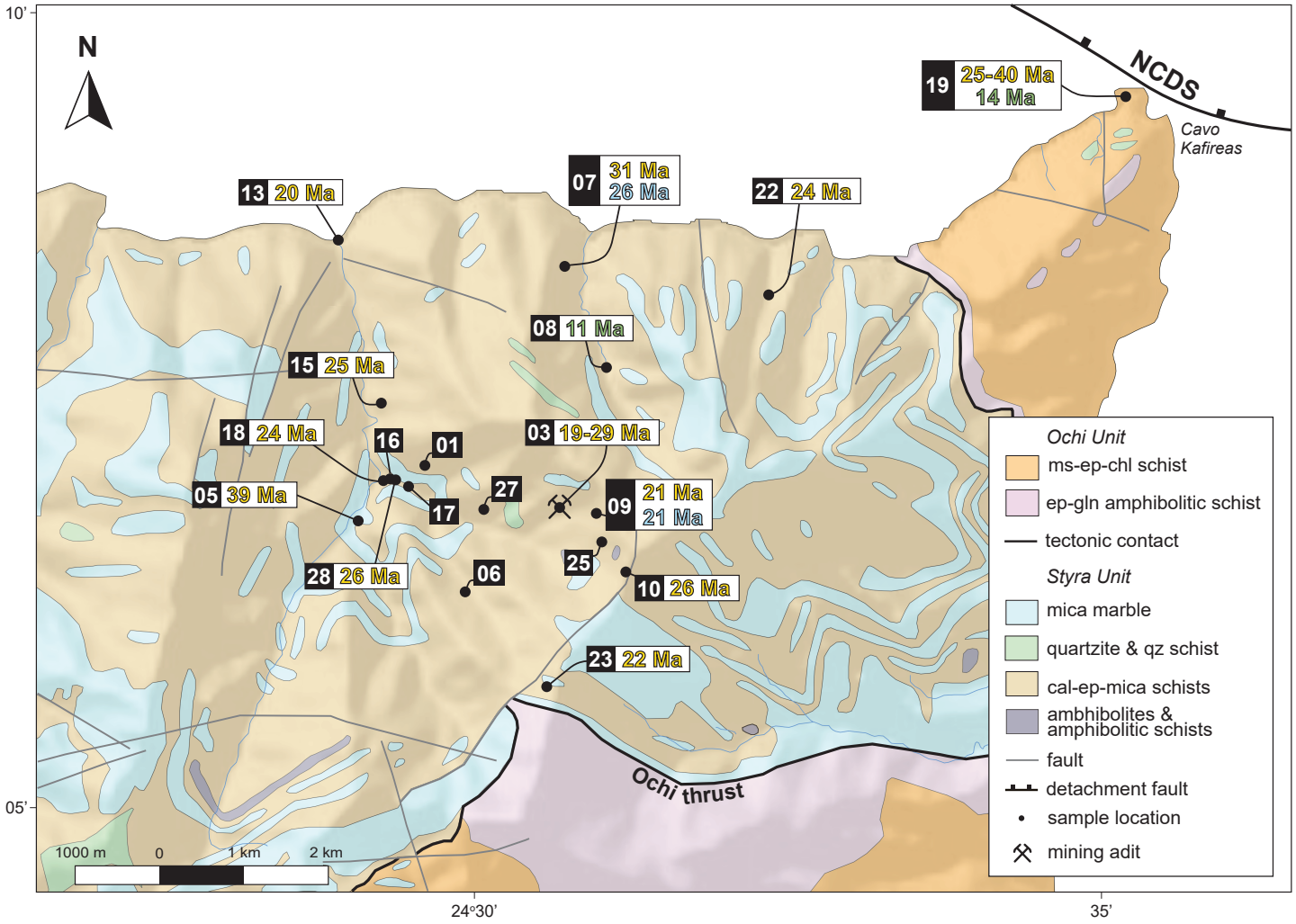

Figure 2. Geological map of the Kallianos ore deposit on southern Evia, Greece. Map highlights locations of samples; see Table 1 for details of station number (black boxes). Colored font associated with geochronology: white mica $^{40}Ar/^{39}Ar$ (yellow), white mica $^{87}Rb/^{87}Sr$ (blue) and zircon (U-Th)/He (green) geochronology. Modified after Latsoudas et al. (1997). Abbreviations: cal, calcite; chl, chlorite; ep, epidote; gln, glaucophane; ms, muscovite.

their top by cataclasite and a terminal knife-sharp detachment plane. The hanging wall of these structures displays intense brittle deformation and hydrothermal alteration (Jolivet et al., 2010; Grasemann et al., 2012). Widespread exhumation of the Cycladic Blueschist Unit (CBU) was accommodated by the top-to-NE extension along the NCDS and assisted by top-to-SW extension along the West Cycladic Detachment System (WCDS), as well as top-to-S shear along the Santorini and Folegandros detachment systems (Bakowsky et al., 2023; Grasemann et al., 2012; Jolivet et al., 2010; Schneider et al., 2018). The detachments structurally separate the CBU from overlying klippen of un- to weakly metamorphosed Pelagonian Zone (Jolivet et al., 2010). Preserved Pelagonian rocks are comprised of serpentinite, gabbros and basalts interpreted to be Jurassic ophiolitic material overlying Paleozoic and Mesozoic marbles, gneisses and amphibolites (Bonneau, 1982, 1984; Jacobshagen, 1986; Jolivet et al., 2010; Maluski et al., 1987). Structurally underlying the CBU and the Pelagonian Zone is the late Carboniferous Cycladic Basement, which consists primarily of highly deformed para- and ortho-gneisses metamorphosed from upper greenschist to upper amphibolite facies (Dürr et al., 1978; Flansburg et al., 2019; Henjes-Kunst and Kreuzer, 1982; Poulaki et al., 2019). Northeast-directed shear likely related to displacement along the NCDS has been reported from southern Evia, but the brittle plane of the detachment has not been documented in detail (Jolivet et al., 2010; Gautier and Brun, 1994; Jolivet and Patriat, 1999; Xypolias et al., 2012). Extension was occurring unambiguously at c. 23 Ma, with some models arguing for extension starting as early as 30 Ma (e.g., Huet et al., 2015; Jolivet et al., 2010). Middle to late Miocene plutons were emplaced in the Cyclades between 14 Ma (e.g., Tinos, Mykonos) and 9 Ma (e.g., Lavrion, Serifos; Brichau et al., 2007; Denèle et al., 2011; Jolivet et al., 2010; Iglseder et al., 2009; Skarpelis and Lüders, 2007). Moreover, rhyolitic pyroclastic rocks on Skyros (to the east of Evia) and dacitic subvolcanic intrusions near Oxylithos and tuffs in the Kymi

supradetachment basin of central Evia are of a similar age (c. 14 Ma), and were generated during crustal decompression related to extensional opening of the Aegean basin (Bradley et al., 2013; Pe-Piper and Piper, 1994).

Southernmost Evia is composed mainly of HP/LT metamorphic rocks that are correlated with the CBU, and record Eocene HP metamorphism (Figure 1; Lister et al., 1984; Schneider et al., 2011; Tomaschek et al., 2003; Uunk et al., 2022). The massif is subdivided into the Ochi and Styra units (Figure 2, Avigad et al., 1997; Xypolias et al., 2012). The Ochi Unit structurally overlies the Styra Unit along the Ochi Thrust, and comprises a partly ophiolitic sequence of ultramafic to felsic igneous rocks, quartzites, and iron stones (Xypolias et al., 2012). The underlying passive margin sequence of the Styra Unit is a series of interspersed marbles, calc- and mica schists mixed with of quartzite and manganese cherts (Ring et al., 2007; Xypolias et al., 2012). The schists are deformed by multiple generations of variably open to isoclinal folds, structures consistent with those reported by Xypolias et al. (2012). At the map scale, folds define a type-3 interference pattern with two fold generations with subparallel fold axes and refolding of axial planes of the first generation (Figure 2; Xypolias et al., 2012).

The CBU underwent greenschist facies overprinting during its aforementioned two-stage exhumation history. On Evia, the CBU likely experienced this greenschist facies event at c. 21-25 Ma, following metamorphic conditions of ~400°C to 460°C and ~13 kbar (Ducharme et al., 2022; Katzir et al., 2000; Shaked et al., 2000). Low-temperature geochronology from central Evia reveals the CBU there cooled below ~200°C by 15-17 Ma (Ducharme et al., 2022; Ring et al., 2007). Those dates suggest relatively early cooling for Evia in comparison with the low-temperature geochronological picture from throughout the Cyclades, which indicates cooling below such

temperatures between c. 8-14 Ma (Berger et al., 2013; Coleman et al., 2020; Schneider et al., 2018; Shin, 2014; Soukis and Stockli, 2013).

The Cycladic Mineral District

The Cycladic Mineral District (CMD) is an extensive and historically important metallurgical area, with economically significant deposits known from many Cycladic islands (Vaxevanopoulos et al., 2022; Wind et al., 2020). The CMD hosts a panoply of deposit types, including intrusion-related, carbonate replacement, vein-type, low- to high-sulfidation epithermal, and skarn deposits (Skarpelis, 2002; Voudouris et al., 2019, Wind et al., 2020). Wind et al. (2020) demonstrated variations in the source of the fluids within the CMD based on differences in Pb-isotope signatures of galena in the deposits. Galena in the north-central Cyclades, such as on Evia, Andros, Tinos and Syros, have a less radiogenic signature, suggesting fluids sourced from, and interacted with, the Cycladic Basement, whereas the Pb-isotope signatures in the western Cyclades, such as in Lavrion, Serifos and Milos, have a higher radiogenic signature, likely tapping one of the structurally higher nappes of the CBU (i.e., Lower Cycladic Blueschist Nappe; Grasemann et al., 2017). These data revealed separation of the metal sources across a boundary that is parallel to the proposed trace of the Trans-Cycladic Thrust (TCT), a major syn-orogenic nappe boundary (Figure 1; Grasemann et al., 2017; Wind et al., 2020).

The Kallianos Au-Ag-Te mineral deposit of southern Evia consists of numerous vein- and fault-hosted Au-Ag-Te occurrences (Tombros et al., 2021). The veins occur in the interbedded schists and marbles within the Styra Unit that were complexly deformed during subduction. Previous work on the deposit focused on characterizing the vein geochemistry and mineral paragenesis (Tombros et al., 2021; Vavelidis and Michailidis, 1990; Voudouris et al., 2011).

Mineralization is hosted in tension gashes, which may extend 500-700 m vertically with widths of up to 3 m, and contain milky to clear quartz and calcite. Pyrite is the dominant sulphide phase, with subordinate galena, arsenopyrite, chalcopyrite, sphalerite, lollingite, tellurides, and sulphosalts with gold and silver (Tombros et al., 2021; Vavelidis and Michailidis, 1990; Voudouris et al., 2011). The vein system cross-cuts older, layer-parallel carbonate replacement-style mineralized veins, described as hosting calcite and pyrite mineralization. The combination of H_2S and CH_4/CO_2 geothermometers and fluid inclusion microthermometry suggests precipitation temperatures between 120°C to 260°C, and a trapping pressure of the fluid inclusions within the vein quartz of ~220 bars to ~145 bars (<1 km depths). Fluid inclusion microthermometry also indicates fluid salinities of 2.2 to 15.8 wt% NaCl equivalent, and sulfur isotopes reveal a mineralizing fluid pH between 5.4 to 5.8. Tombros et al. (2021) proposed a magmatic source for the Kallianos mineralizing fluids, supported by the stable and radiogenic isotope data detailed above. Rb-Sr isochron data from vein-hosted pyrite yielded dates between 8.1 ± 0.2 Ma and 7.6 ± 0.2 Ma, which those workers note is consistent with the timing of magmatism in the Cyclades. Due to the apparent absence of magmatism proximal to the deposit, and extremely limited magmatism on Evia overall (Pe-Piper and Piper, 1994), Tombros et al. (2021) proposed a link either to a hitherto undiscovered Miocene intrusion on southern Evia, or else speculated that mineralizing fluids were channeled along detachment faults from distal plutons. Proposed candidates (Figure 2) include the c. 9 Ma Plaka granodiorite of Lavrion (~60 km SW of Kallianos), or the c. 19-14 Ma Tinos granodiorite-leucogranite (~85 km E of Kallianos).

Many other deposits in the CMD have been linked to magmatic processes (Figure 1). Magmatic fluids generated from the Plaka intrusion of Lavrion were invoked as the source of the Plaka Pb-Ag-Zn (Fe-Cu) deposit due to its C-, O-, and S- isotope signatures (Berger et al., 2013;

Bonsall et al., 2011; Scheffer et al., 2017). Calcite C- and O-isotopes indicated variable interaction between the CBU wall rock and the magmatic fluids (Berger et al., 2013; Bonsall et al., 2011; Scheffer et al., 2017). Sulfide S-isotope signatures are consistent with a magmatic source, but may also be consistent with reduced seawater sulfate (Bonsall et al., 2011). Structurally, the mineralized veins forming the deposits on Attica, oriented WNW-ESE, are perpendicular to the SSW-directed extension in the area driven by the WCDS (Figure 1; Berger et al., 2013; Coleman et al., 2020; Scheffer et al., 2017). Low-temperature geochronology from Berger et al. (2013) revealed cooling of the WCDS footwall through ~200°C by c. 7-8 Ma, thus indirectly dating the brittle-ductile veins hosting the Lavrion mineralization. The tectonic relationships between the migration of the Plaka intrusion fluids in the veins and crustal-scale ductile-brittle structures accommodating displacement along the WCDS is unequivocal (Berger et al., 2013; Scheffer et al., 2017; Skarpelis and Lüders, 2007). The implied coincidence of mineralization and exhumation facilitated by the WCDS prompted Berger et al. (2013) to interpret the detachment as a major structural control on the mineralizing fluids, similar to the role inferred by Tombros et al. (2021) for the post-orogenic structures at the Kallianos deposit.

Our investigation of the deposit's structural architecture, timing, and fluid sources employed multiple complementary approaches. Field mapping and structural measurements revealed the deformation mechanisms and structural relationships between the veins and host rock. To constrain the timing of vein formation, we conducted $^{40}Ar/^{39}Ar$ geochronology on white mica from both the host rock and vein halos using a multiple, single-grain total fusion approach. A key advantage of this particular method is that it constrains age heterogeneity within a sample (meso-scale), across multiple samples (macro-scale), and is particularly useful for polydeformed terranes as age variations within samples may be the product of repeated heating and deformation that is not

captured by the step-heating method. We supplemented this with white mica $^{87}Rb/^{87}Sr$ geochronology, which enabled laser-based, micrometre-scale, in-situ sampling, and allows for the intentional selection and comparison of vein-proximal mica with microstructurally different white mica in the host rock. Mineralogical and geochemical analyses included back-scattered electron (BSE), scanning electron microscopy (SEM), and electron microprobe analysis which provided base metal element mapping of selected pyrite grains. These analyses build upon previously documented fluid stages and evolution patterns of the deposit (Tombros et al., 2021). To trace fluid pathways and sources, we analyzed calcite C- and O-stable isotopes in qz ± cal veins, comparing the Kallianos deposit signatures with those of the surrounding CBU host rock and other regional deposits. This includes deposits in the Lavrion area, where mineralization has been linked to plutonic events associated with major crustal-scale detachment faults. Summary of sample collection and data for the Kallianos ore deposit are located in Table 1.

Analytical Methods

Mineral chemical analysis

Thin sections were examined and imaged with back-scattered electron (BSE) scanning electron microscopy (SEM) on the JEOL 6610LV SEM at the University of Ottawa (Canada). Working distance was set to 10 mm, spot size was set to 5 µm, and voltage was set to 20 kV. Major element analyses were conducted on polished thin sections of samples using the JEOL JXA-8230 Superprobe at the University of Ottawa (Canada). The microprobe was operated with a voltage of 20 kV and a beam current of 300 nA. Pixel size was 1 × 1 µm, and counting time was 133 ms/pixel. A combination of natural and synthetic standards were used for calibration and analyses were corrected using a ZAF matrix correction routine. Elemental maps of pyrite were collected over an

Table 1. Summary of sample information, Kallianos ore deposit, Evia, Greece

sample	UTM (zone 35)	lithology	sample type	mica $^{40}Ar/^{39}Ar$ date (Ma)	mica $^{87}Rb/^{87}Sr$ date (Ma)	zircon (U-Th)/He date (Ma)	$\delta^{13}C$‰ (VPBD)	$\delta^{18}O$‰ (SMOW)	petrography	element map
23-01C	E 280208 N 4221852	quartz-chlorite-mica schist	vein	-	-	-	-	-	✓	-
23-03A	E 281778 N 4221317	carbonate-mica schist	host rock	19-29 ± 1	-	-	-	-	✓	-
23-03B			mineralized vein	-	-	-	-	-	-	✓
23-03D			mineralized vein	-	-	-	-0.73	14.43	-	-
23-05A	E 279411 N 4221195	chlorite schist	mineralized vein with host rock	39 ± 1	-	-	-1.96	15.81	✓	-
23-06A	E 280704 N 4220358	quartz-chlorite-mica schist	orientend mineralized vein	-	-	-	-0.58	15.13	✓	-
23-07A	E 281854 N 4224153	quartz-mica-epidote schist	host rock	31 ± 1	26 ± 3	-	-	-	✓	-
23-07C			mineralized vein	-	-	-	-	-	✓	-
23-08A	E 282335 N 4222998	mica schist	host rock	-	-	11 ± 1	-	-	-	-
23-09A	E 282241 N 4221304	quartz-mica pyrite schist	mineralized vein with host rock	21 ± 1	21 ± 3	-	-0.13	19.31	✓	-
23-10A	E 282563 N 4220586	quartz-carbonate-mica schist	host rock	26 ± 1	-	-	-	-	✓	-
23-10B			oriented vein	-	-	-	-	-	✓	-
23-10C			vein	-	-	-	-	-	✓	-
23-13B	E 279183 N 4224502	quartz-carbonate-mica schist	host rock	20 ±1	-	-	-	-	✓	-
23-15A	E 279643 N 4222577	quartz-mica schist	vein with host rock	25 ± 1	-	-	-	-	✓	-
23-16A	E 279814 N 279814	quartz-chlorite-mica schist	vein	-	-	-	-0.77	18.63	✓	-
23-17A	E 280055 N 4221579	quartz-chlorite-mica schist	mineralized vein	-	-	-	-3.31	20.78	✓	-
23-18A	E 279741 N 4221680	schistose marble	host rock	24 ± 1	-	-	-	-	✓	-
23-19A	E 288436 N 4226169	quartz-mica schist	host rock	25-40 ± 1	-	14 ± 1	-	-	✓	-
23-19B			Mineralized cataclasite	-	-	-	-	-	✓	-
23-19C			oriented vein	-	-	-	-	-	✓	-
23-22A	E 284235 N 4223873	chlorite-mica schist	vein with host rock	24 ± 1	-	-	-	-	✓	-
23-22B			vein with host rock	-	-	-	-0.89	17.33	✓	-
23-23A	E 281649 N 4219222	quartz-mica schist	mineralized vein with host rock	-	-	-	0.40	17.31	✓	-
23-23B			mineralized vein with host rock	22 ± 1	-	-	-	-	✓	-
23-25A	E 282305 N 282305	quartz-chlorite-mica schist	mineralized vein	-	-	-	-	-	✓	-
23-27A	E 280900 N 4221309	quartz-chlorite-mica schist	mineralized vein	-	-	-	-0.55	14.86	✓	-
23-27B			mineralized vein	-	-	-	-	-	✓	✓
23-28A	E 279886 N 4221645	quartz-chlorite-mica schist	mineralized vein	26 ± 1	-	-	-	-	✓	-

area of ~400 μm^2, and the elements that were analyzed include As, Co, Cu, Fe, Ni, S, Sb, Se, Si, and Zn. Processing of the data was performed using XMapTools 4.3 (Lanari et al., 2014, 2019).

Sample preparation for geochronology

Conventional procedures were used to extract and select the most appropriate minerals from rock samples in preparation for (U-Th)/He and $^{40}Ar/^{39}Ar$ dating. Each sample was cleaned with a wire brush and water to remove any surface contamination. The sample was allowed to air dry and was then crushed to a size fraction of ≤1 cm with the use of a standard jaw crusher. The material was then passed through a series of sieves to obtain grain size fractions >250 μm, 63-250 μm and <63 μm. The 63-250 μm fraction was then rinsed through a decantation process to remove any remaining fine powder adhering to the grains and dried for 24 h at a temperature of 30°C using a heat lamp. Heavy mineral separation was then conducted using methylene iodide (SG: 3.0 g/cm^3) in order to obtain a more concentrated fraction of zircon. The heavy mineral separates were then individually passed through a Frantz magnetic mineral separator as needed to further isolate zircon. White mica was obtained from the >250 μm size fraction using a mortar and pestle to further crush the sample while preserving the integrity of the mica. Samples were sieved to obtain a 150 μm-250 μm size fraction. In the case of white mica and zircon grains were then picked using tweezers under a binocular microscope.

$^{40}Ar/^{39}Ar$ geochronology

Once mica samples were picked and characterized, $^{40}Ar/^{39}Ar$ analytical work was performed at the University of Manitoba (Winnipeg, Canada) using a multi-collector Thermo Fisher Scientific ARGUS VI mass spectrometer, linked to a stainless steel Thermo Fisher Scientific

extraction/purification line and Photon Machines (55 W) Fusions 10.6 CO_2 laser. Argon isotopes (from mass 40 to 37) were measured using Faraday detectors with low noise 1 x 10^{13} Ω resistors and mass 36 was measured using a compact discrete dynode detector. The sensitivity for argon measurements is ~6.312 x 10^{17} moles/fA as determined from measured aliquots of Fish Canyon sanidine (Dazé et al., 2003; Kuiper et al., 2008).

Standards and unknowns were placed in 2 mm deep wells in 18 mm diameter aluminum disks, with standards placed strategically so that the lateral neutron flux gradients across the disk could be evaluated. Planar regressions were fit to the standard data, and the $^{40}Ar/^{39}Ar$ neutron fluence parameters, J, interpolated for the unknowns. Uncertainties in J are estimated at 0.1-0.2% (1σ), based on Monte Carlo error analysis of the planar regressions (Best et al., 1995). All specimens were irradiated in the cadmium-lined, in-core CLICIT facility of the Oregon State University TRIGA reactor. The duration of irradiation was 12 h and using the Fish Canyon sanidine (Kuiper et al., 2008) and GA1550 biotite (Spell and McDougall, 2003) standards.

Irradiated samples were placed in a Cu sample tray, with a KBr cover slip, in a stainless steel high vacuum extraction line and baked with an infrared lamp for 24 h. Single crystals were either fused or step-heated using the laser, and reactive gases were removed, after ~3 min, by three GP-50 SAES getters (two at room temperature and one at 450°C) prior to being admitted to an ARGUS VI mass spectrometer by expansion. Five argon isotopes were measured simultaneously over a period of 6 min. Measured isotope abundances were corrected for extraction-line blanks, which were determined before every sample analysis. Line blanks averaged ~5 fA for mass 40 and ~0.022 fA for mass 36.

Mass discrimination was monitored by online analysis of air pipettes, which gave during two separate sessions mean of D: 1.0063 ± 0.0001 and D: 1.0089 ± 0.0005 per amu, based on 67

aliquots interspersed with the unknowns. A value of 295.5 was used for the atmospheric $^{40}Ar/^{36}Ar$ ratio (Steiger and Jäger, 1977) for the purposes of routine measurement of mass spectrometer discrimination using air aliquots, and correction for atmospheric argon in the $^{40}Ar/^{39}Ar$ age calculation. Corrections are made for neutron-induced ^{40}Ar from potassium, ^{39}Ar and ^{36}Ar from calcium, and ^{36}Ar from chlorine (Roddick, 1983; Renne et al., 1998; Renne and Norman, 2001). Results are reported in Table S1 in the supplementary information.

(U-Th)/He geochronology

The analytical portion of the (U-Th)/He experiments was conducted at the TRaIL (Thermochronology Research and Instrumentation Laboratory) facility at the University of Colorado (Boulder, USA). Individual mineral grains are handpicked using a Leica M165 binocular microscope equipped with a calibrated digital camera and capable of both reflected and transmitted, polarized light. The grains are screened for quality, including crystal shape and the presence of inclusions. The dimensions of the crystals are measured and converted to equivalent spherical radius (ESR) as this value is more readily incorporated into the equations that govern the diffusion of He throughout the grain; from this point forward in the paper references to grain size are measurements of ESR. After characterization, grains are placed into small Nb tubes that are then crimped on both ends. This Nb packet is then loaded into an ASI Alphachron He extraction and measurement line. The packet is placed in the UHV extraction line (~$3x10^{-8}$ torr) and heated with a diode laser to ~800-1100°C for 5 to 10 m to extract the radiogenic ^{4}He. The degassed ^{4}He is then spiked with ~13 ncc of pure ^{3}He, cleaned via interaction with two SAES getters, and analyzed on a Balzers PrismaPlus QME 220 quadrupole mass spectrometer. Degassed grains are then removed from the line, and taken to a Class 10 clean lab for dissolution. Zircons are dissolved

using Parr large-capacity dissolution vessels in a multi-step acid-vapour dissolution process. Grains (including the Nb tube) are placed in Ludwig-style Savillex vials, spiked with a ^{235}U-^{230}Th tracer, and mixed with 200 µl of Optima grade HF. The vials are then capped, stacked in a 125 mL Teflon liner, placed in a Parr dissolution vessel, and baked at 220°C for 72 h. After cooling, the vials are uncapped and dried down on a 90°C hot plate until dry. The vials then undergo a second round of acid-vapour dissolution, this time with 200 µl of Optima grade HCl in each vial that is baked at 200°C for 24 h. Vials are then dried down a second time on a hot plate. Once dry, 200 µl of a 7:1 HNO_3:HF mixture is added to each vial, the vial is capped, and cooked on the hot plate at 90°C for 4 h. Once the minerals are dissolved, regardless of the dissolution process, they are diluted with 1 to 3 mL of doubly-deionized water, and taken to the ICP-MS lab for analysis. Mineral standards of Durango apatite (31.5 Ma) and Fish Canyon Tuff zircon (28.2 Ma) are routinely analyzed (degassed and dissolved) in conjunction with the samples with each run to ensure data integrity. Sample solutions, along with standards and blanks, are analyzed for U, Th, and Sm content using a Thermo Element 2 magnetic sector mass spectrometer. Once the U, Th, and Sm contents have been measured, He dates and all associated data are calculated on a custom spreadsheet made by TRaIL staff. Results are reported in Table S2 in the supplementary information.

In-situ Rb-Sr geochronology

Two 30 µm-thick polished sections were prepared from samples 23-07A and 23-09A for in-situ $^{87}Rb/^{87}Sr$ geochronology. Procedures follow Zack and Hogmalm (2016) and Hogmalm et al. (2017) using an Agilent 8900 triple-quadrupole inductively coupled plasma mass spectrometer equipped with a reaction cell paired to an ESL 193 Excimer laser with a TwoVol3 ablation cell in

the Fipke Laboratory for Trace Element Research at University of British Columbia-Okanagan (Kelowna, Canada). The analyses followed the basic procedures outlined in Larson et al. (2023) with the white mica ablated using a 50 μm diameter spot, a repetition rate of 10 Hz and a laser fluence of 4 J/cm^2.

Analyses of secondary reference materials include an in-house white mica MA1 (c. 350 Ma, A. Camacho, unpublished data), white mica MA2 (c. 350-360 Ma, A. Camacho, unpublished data), white mica 1B (c. 990 ± 5 Ma, Camacho et al., 2012), white mica 1O (c. 986 ± 5 Ma, Camacho et al., 2012), a nano-powdered biotite, Mica-Fe (305.4 ± 2.0 Ma, Rösel and Zack, 2022), and a nano-powered tablet, Mica-Mg (c. 519 ± 7 Ma, Hogmalm et al., 2017). The dates of the reference material analyses overlap within error of those expected (355 ± 3 Ma, 355 ± 3 Ma, 994 ± 8 Ma, 979 ± 18 Ma, 306 ± 2 Ma, and 512 ± 3 Ma, respectively). Results and reference material are reported in Table S3.1 and Table S3.2 in the supplementary information. Isochron calculations excluded analyses with high uncertainty, using a >30% (2 standard error of the mean) cut-off that resulted in no data exclusion. Data processing and visualization were performed using the online version of the IsoPlotR package (Vermeesch, 2018).

Stable isotope geochemistry

Calcite from veins was extracted via a Dremel tool and analyzed at the Ján Veizer Isotope Laboratories (University of Ottawa, Canada) following the Thermo Finnigan Gas Bench II protocols. The samples and standards are first weighed to 0.5 mg ± 10% into exetainers. Two samples of a blind in-house standard (C-44) for calcite and three international standards (C-35, C-38, C-43) were analyzed as the first and last runs. A sample duplicate is applied to a sample at the center of the list. A 0.1 mL drop of H_3PO_4 (SG: 1.91 g/cm^3) is added to the inside lip of the

horizontal exetainer. The exetainers are capped and helium-flushed while horizontal, and calcite samples are reacted upright at 25°C for 24 h to produce CO_2. This is followed by extraction in a continuous flow of helium via a Thermo Finnigan Gas Bench II connected to a Thermo Finnigan Conflo IV. Six peaks are measured on a Thermo Finnigan Delta XP and then an average is calculated. Analytical precision (2σ) is ±0.1‰. Analytical errors are ±0.4‰ and data are reported as per mil (‰) relative to Vienna Standard Mean Ocean Water (V-SMOW) for oxygen and as per mil (‰) relative to Vienna Pee Dee Belemnite standard (V-PDB) for carbon (Coplen et al., 2022). Results are reported in Table S4 in the supplementary information.

Structural observations

Kallianos ore deposit

New bedrock mapping, structural data, and microstructural analysis of the Kallianos ore deposit have revealed a relative timing of the different vein sets and their respective parageneses. Schists with a qz + wm ± cal ± chl mineral assemblage are the dominant lithology of the Kallianos deposit, and exhibit a penetrative foliation and well-developed stretching lineation defined by elongate aggregates of white mica (250-400 μm) that comprise up to 25% of the rock volume (Figure 3a, 4a). Quartz (50-200 μm) in the schists comprises 30-40% of the rock, displays low-amplitude bulging of the grain boundaries and undulose extinction (Figure 3a). Anhedral calcite in the schists (100 μm-1 mm) constitutes up to 30% of the rock, has irregular, jagged grain boundaries, and exhibits a shape-preferred orientation (SPO) parallel to the micaceous foliation. Calcite twins are of type II and III (Passchier and Trouw, 2005), and range between 2-5 μm in thickness. Subordinate minerals include epidote, apatite, zircon, rutile, pyrite and chalcopyrite.

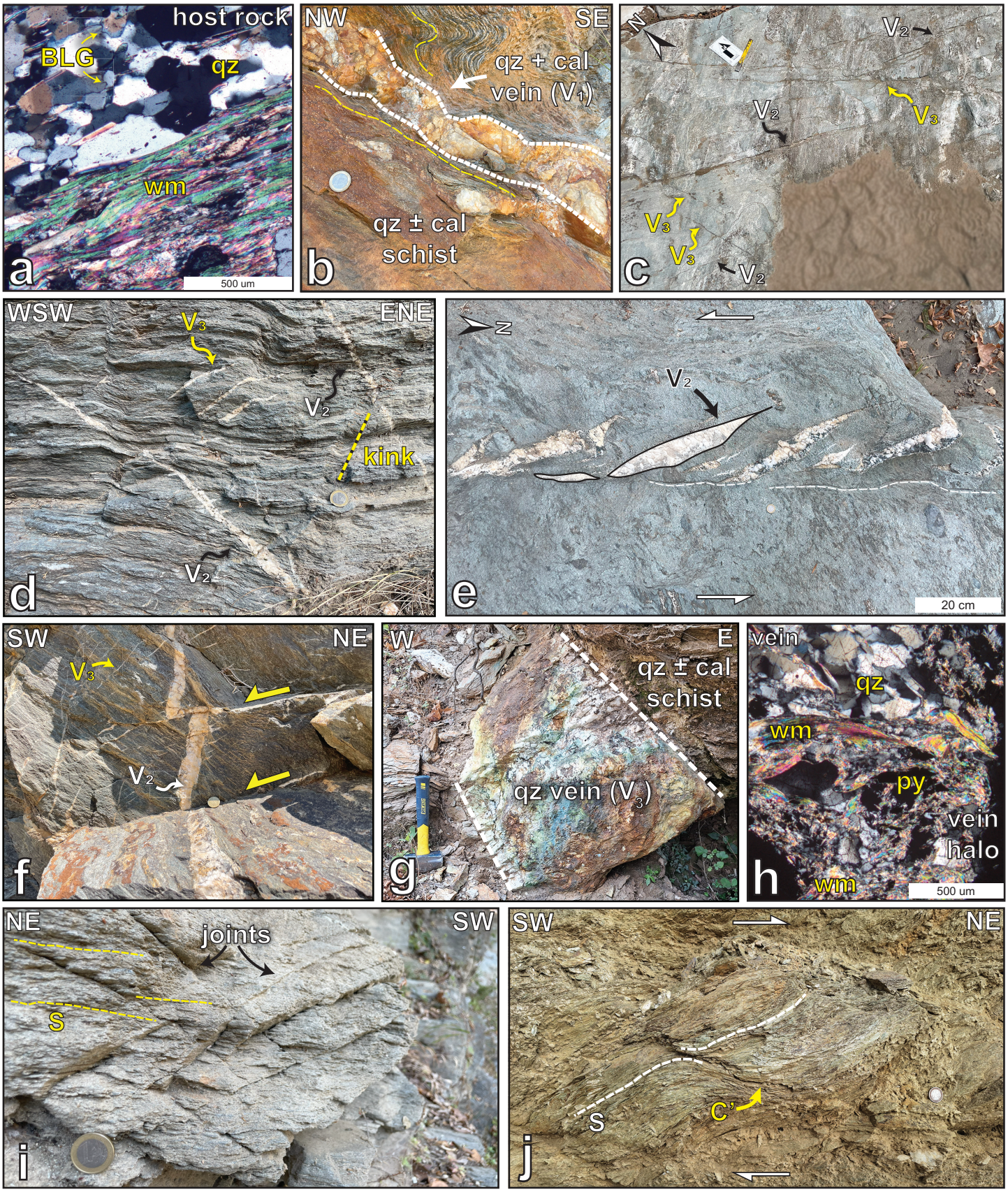
host rock
BLG
qz
wm
500 um
a
NW
SE
qz + cal
vein (V1)
qz ± cal
schist
b
N
V2
V2
V3
V3
V3
V2
c
WSW
ENE
V3
V2
kink
V2
d
z
V2
20 cm
e
SW
NE
V3
V2
f
W
E
qz ± cal
schist
qz vein (V3)
g
vein
qz
wm
py
vein
halo
wm
500 um
h
NE
SW
joints
S
i
SW
NE
S
C'
j

Figure 3. Field photos and photomicrograph of the veins of the Kallianos ore deposit on Evia, Greece. (a; E 282563, N 4220586) Photomicrograph (cross-polarized light) of the host rock, a qz ± cal schist, of the Kallianos ore deposit from sample 23-10A, showing homogenous foliation-defining mica and quartz showing minor incipient grain boundary bulging (BLG). (b; E 284235 N 4223873) Photo of layer-parallel, pyrite-bearing carbonate replacement qz + cal vein showing pinch-and-swell structure, hosted in qz ± cal schists (white dashed lines). Yellow dashed line represents foliation. Note folding above the vein. (c; E 279741 N 21711) Plan view of cross-cutting relationships between NNW-striking veins (V_3) and NW-striking veins (V_2). (d; E 280900 N 4221309) Section view of the same two vein generations hosted in qz ± cal schist of the Styra Unit: the E-dipping, NNW-striking set (V_3) cross-cuts a SW-dipping, SE-NW-striking vein set (V_2); both examples here are unmineralized. Kink bands (kink, yellow and black dashed line) strike parallel to V_2 but dip toward W. (e; E 279886 N 4221645) Plan view of sigmoidal en-echelon, unmineralized qz ± cal veins. Minor rotation and a bounding shear plane suggests the veins opened during sinistral shear along a NNW-striking plane. (f; E 281538 N 4221446) Unmineralized shallow-dipping NNW-striking veins (V_3) cross-cutting a larger NW-striking vein (V_2) displaced by top-to-SW brittle faults. (g; E 279183 N 4224502) Photo of the Agia Barbara mineralized qz vein (white dashed lines) hosted in qz ± cal schists of the Styra Unit. The vein cross-cuts foliation with a NNW strike. (h; E 281854 N 4224153) Photomicrograph (cross-polarized light) of vein halo white mica adjacent to the vein used for Ar-Ar and Rb-Sr geochronology of sample 23-07A. (i; E 279886 N 4221645) Conjugate joint sets observed in the Kallianos ore deposit location striking NW-SE (300-320°). Yellow dashed lines (S) represent foliation of the qz + wm ± cal schist. (j; E 280704 N 4220358) C'-type shear band showing top-to-NE shear sense deep in the footwall of the NCDS. Abbreviations: BLG, grain boundary bulging; cal, calcite; kink, kink band; py, pyrite; qz, quartz; wm, white mica; S, foliation.

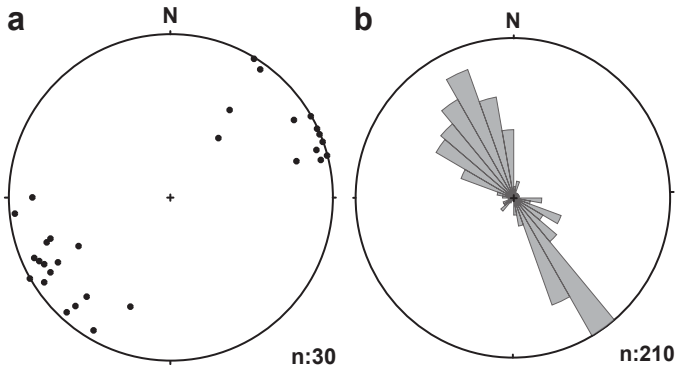

Figure 4. (a) Stereonet showing NE-SW trending stretching lineations measured in the Kallianos area. (b) Rose diagram summarizing vein and joint orientations associated with the Kallianos deposit, striking dominantly NW-SE to NNW-SSE.

Mica-bearing marbles consist of mostly (≥70%) subhedral calcite (100 μm-2 mm) exhibiting a foliation-defining SPO, with the remaining rock volume composed of quartz (30 μm-1 mm) showing undulose extinction and bulging of grain boundaries, as well as fine-grained white mica (~75 μm). The quartzites are composed of 70% quartz (200 μm-1 mm) that likewise exhibit undulose extinction and bulging of grain boundaries, lesser (~20%) anhedral calcite (200 μm-1.5 mm), and bundles of white mica (30-70 μm) defining a weak foliation.

Rocks in the Kallianos deposit do not preserve obvious mineralogical evidence of HP-LT metamorphism that is documented elsewhere in the Styra Unit, despite retaining macroscopic structural features developed during this event (Xypolias et al., 2012). Conversely, quartz and calcite microstructures, and qualitative evaluations of host rock mineral assemblages, suggest comprehensive greenschist facies retrogradation of the mineralization-hosting lithologies.

Three vein sets are present throughout the deposit. The oldest veins are foliation-parallel carbonate replacement veins (V_1), often exhibiting pinch-and-swell or boudinage structure, which were documented by Tombros et al. (2021; Figure 3b). These veins are composed of qz + cal and are 10-50 cm thick with distinct and sharp vein boundaries. The layer-parallel veins have strongly chloritized and ankeritized halos (20-100 cm), and contain trace amounts of fine-grained (~200 μm) subhedral pyrite. Quartz in V_1 carbonate replacement veins exhibits quartz microstructures such as undulose extinction, serrated grain boundaries and low-amplitude grain boundary bulging. The microstructures are consistent with dynamic recrystallization possibly via subgrain rotation and bulging grain boundary. The two younger vein sets (V_2, V_3) are mode I tension gashes that cross-cut foliation and strike NW-SE and NNW-SSE, respectively (Figure 3c-f). Consistent cross-cutting relationships permit us to establish V_2 as the older of the two tension gash populations, consisting of NW-SE striking veins whose dips range from subvertical to 45° toward NE or SW

(Figure 3c,d,f). Dip directions of V_2 veins are generally consistent within a given exposure. Individual veins are 5 mm to 30 cm wide with sharp boundaries to the wall rock, and no obvious alteration halos. Veins are composed of qz ± cal ± ab with a minor degree of ankeritization.

The youngest vein set (V_3) consists of NNW-SSE striking veins, dipping shallowly to moderately E and W, that host the bulk of the mineralization (Figure 3c-g). These veins range from 5 mm to 1 m in width, are in some cases weakly to moderately ankeritized, and have planar boundaries with their micaceous wall rock margins (Figure 3d-g). White mica is commonly present at V_3 margins, where it is often, but not always, coarser than foliation-defining white mica in the host rock. These vein-proximal mica are tabular, variable in size (5-500 μm in thickness), and possess no systematic orientation (Figure 3h). The V_3 veins are composed of qz ± cal ± ab, and in contrast to V_2 veins, may impart diffuse chlorite halos up to a metre from the vein that produced trace pyrite mineralization. Although numerous mineralized veins and faults are reported from the Kallianos deposit (Tombros et al., 2021), we documented volumetrically significant sulphide mineralization only in the Agia Barbara vein (23-03B, Figure 2, 3g). The Agia Barbara qz + ab vein cross-cuts foliation with a NNW strike (i.e., parallel to V_3), dipping 50° to E with a width of 60 cm. The Agia Barbara vein contains a sulphide assemblage including pyrite, chalcopyrite, galena, and covellite (more detailed description below).

In addition to the veins described here, several other structures systematically overprint the dominant metamorphic foliation of the Kallianos area. Joint sets that are co-planar with the V_2 and V_3 vein sets occur throughout the deposit, and are often more numerous than their co-planar veins (Figure 3i). Kink band sets parallel to V_2 and V_3 are common throughout the study area, and induce abrupt cm-scale deflection of the foliation (Figure 3d). En-echelon sigmoidal tension gashes, ostensibly parallel to V_2, are locally developed between bounding brittle-ductile shear planes

oriented parallel to V_3, implying some veins are related to brittle-ductile transcurrent shear. Vein geometries associated with these structures indicate a sinistral shear sense with a left-lateral strike slip component (Figure 3e). Structures preserved occasionally throughout the Kallianos deposit, mainly quartz sigmoids (Figure 3e) and brittle-ductile C'-type shear bands (Figure 3j), demonstrate top-to-NE brittle-ductile dip-slip shear consistent with observations from southern Evia (Ducharme et al., 2022, 2024; Jolivet et al., 2004; Xypolias et al., 2012). Finally, late top-to-SW brittle low-angle faults, striking NW-SE, locally dismember all older structures (Figure 3f).

North Cycladic Detachment System

The new field observations confirm the proposed exposure of the NCDS at the tip of Cavo Kafireas, the northeastern promontory of southern Evia (Figure 2). There, a 0.5 m wide brittle fault plane that dips ~30° toward NE separates a hanging wall consisting of heavily altered, locally talc-bearing mafic schists, from the Ochi Unit footwall composed of comparatively less altered, pelitic and quartzitic rocks (Figure 5a). Rocks in the immediate footwall include qz + wm schists and phyllonites, with well-developed stretching lineations trending NE-SW. The schists exhibit an intensification of brittle deformation toward the brittle fault plane. Brittle-ductile shear bands documented up to 100 m below the detachment record top-to-NE shear (Figure 5b). At still lower structural levels, near the mapped contact between the Styra Unit and overlying Ochi Unit (i.e., the northern exposure of the Ochi Thrust, Figure 2; Latsoudas et al., 1997; Xypolias et al., 2012), ultracataclasites occupying this tectonized boundary display SCC' fabrics indicating a synthetic sense of displacement to the structures documented both structurally above and below (Figure 5c).

Quartz (10-200 μm) in the qz + wm schists occurs in equigranular polycrystalline aggregates exhibiting serrated grain boundaries and low-amplitude grain boundary bulging, with quartz

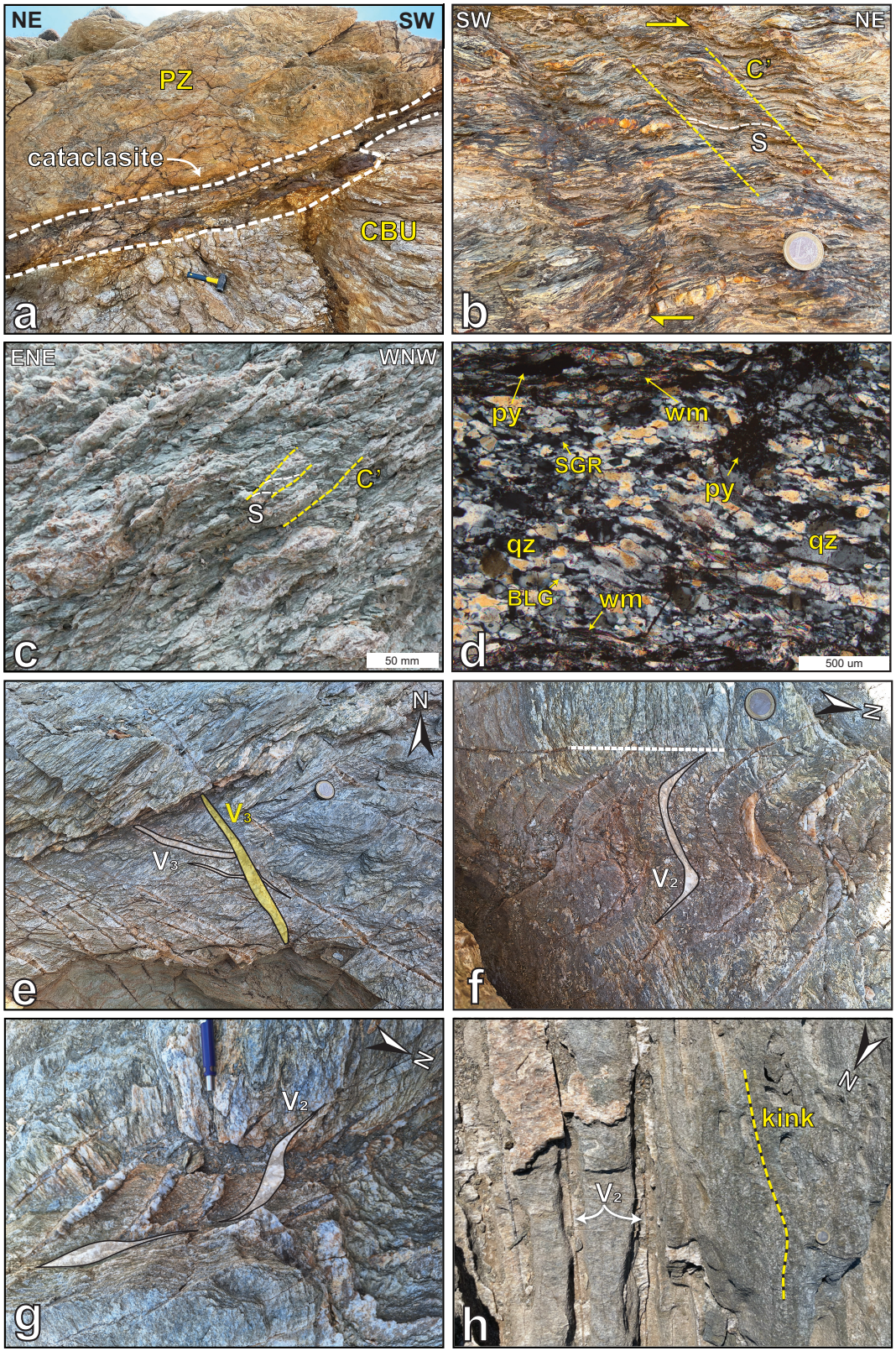
NE
SW
PZ
cataclasite
CBU
a
SW
NE
C'
S
b
ENE
WNW
S
C'
50 mm
c
py
wm
SGR
py
qz
qz
BLG
wm
500 um
d
N
V3
V3
e
N
V2
f
N
V2
g
N
kink
V2
h

Figure 5. Field photos and photomicrographs from the exposed segment of the NCDS on southern Evia. (a; E 288436 N 4226169) Brittle NCDS detachment plane exposure in the southeast of Evia. The NCDS divides schists of the Cycladic Blueschist Unit (CBU) from a heavily altered hanging wall, possibly the Pelagonian Zone (PZ). (b; E 288224 N 4224570) SCC' shear band fabric ~100 m structurally below the brittle NCDS detachment plane indicating top-to-NE shear sense. (c; E 286484 N 4223228) SCC' shear band fabric adjacent to the Styra-Ochi Unit contact. (d; E 288436 N 4226169) Photomicrograph (cross-polarized light) of a qz-wm schist from the NCDS (23-19A). (e; E 288436 N 4226169; plan view) Unmineralized qz veins striking NNW (V_3) cross-cutting NW-striking set (V_2) in the footwall of the NCDS, fewer than 10 m structurally below the brittle detachment plane. (f, g; E 288436 N 4226169; plan view) Sigmoidal quartz tension gashes (V_2) showing progressive anticlockwise rotation from initially NW-SE toward NE-SW orientations, indicating sinistral ductile deformation coinciding with vein opening and sealing. Note V_2 cross-cut by fine linear V_3 vein. (h; same location as f, g) Kink bands (yellow and black dashed line) strike parallel to V_2 in the immediate footwall of the NCDS. Abbreviations: BLG, bulging grain boundary; king, kink band; py, pyrite; qz, quartz; SGR, sub-grain rotation; wm, white mica.

locally pinned by phyllosilicates (Figure 5d). The microstructures observed show weak sub-grain rotation that was potentially recrystallized by bulging (Passchier and Trouw, 2005). White mica (50-250 μm) constitutes up to 30% of the rock volume, and defines a pervasive undulating foliation. Accessory minerals include euhedral pyrite, zircon, and hematite (Figure 5d). Subjacent to the detachment plane, a boudin-like cataclastic quartzite is likely dynamically recrystallized by sub-grain rotation and forms quartz ribbons, with grain sizes of 5-250 μm. It is mineralized, containing up to 3% euhedral pyrite (20-600 μm, Figure S1-a,b; see supplementary information). Additionally, a separate decametre-scale metatuff(?) block within the schist contains glaucophane (30-600 μm), white mica (100-300 μm), dynamically recrystallized quartz aggregates (20-300 μm) and subhedral plagioclase porphyroblasts (400-800 μm) with trace amounts of subhedral pyrite and zircon (Figure S1-c,d).

Structures documented proximal to the detachment plane are strikingly similar to those observed structurally below in the Kallianos deposit. Rock in the footwall within ~50 m of the trace of the fault hosts qz ± cal ± ab veins (0.5-2 cm thickness) and joints, including both NW-SE (i.e., parallel to V_2) and NNW-SSE striking structures (i.e., parallel to V_3; Figure 5e). Kink bands are also present parallel to, and interspersed with, the joint sets (Figure 5h). Additionally, en echelon sigmoidal tension gashes record apparently continuous rotation of veins during ductile deformation, resulting in vein tips that are oriented NW-SE (i.e., parallel to V_2) connected to cores that have undergone up to 90° anticlockwise rotation toward a NE-SW orientation (Figure 5f, g). The joints and tension gashes striking NNW-SSE (V_3) cross-cut all of the aforementioned structures (Figure 5e). Alongside similarities in quartz microstructures described both here and in the deposit, structures preserved at this local exposure of the NCDS broadly parallel those documented structurally below in the footwall.

Vein petrography and mineralization of the Kallianos ore deposit

Quartz forms the bulk of the vein content from the deposit, with grain sizes ranging from ~100 μm to ~5 mm. The polycrystalline quartz exhibits undulose extinction, interlobate grain boundaries showing recrystallization mechanisms such as bulging and sub-grain rotation consistent with low pressures and temperatures during crystallization of the vein (Figure 6a).

Calcite twin geometry can serve as a proxy for temperature during vein deformation (Passchier and Trouw, 2005). Calcite in the Kallianos veins is anhedral with serrated grain boundaries, ranges from 1-5 mm in diametre and is weakly ankeritized (Figure 6b). Twin geometry shows needle-like to elongate tabular twins, with twin size ranging from <1 μm to 10 μm in thickness. Thin twins dominate in the majority of samples. According to Ferrill et al. (2004), these observations categorize the calcite as type I to type II, with <20% of samples showing a small number of grains with type III to IV twins. The grains are generally blocky, with some thinner veins (<1 cm in thickness) showing elongated crystals. Vein boundaries with the wall rock are mostly irregular and indistinct, and smaller grains are generally found at the vein extremities and with larger grains at the center. These vein microstructures are consistent with syntaxial-biaxial vein growth, indicating that vein growth initiated from both sides of the vein along the vein-wall contact (Passchier and Trouw, 2005).

The mineralization analysis herein is mostly derived from the ~60 cm-wide mineralized Agia Barbara vein (V_3). The Agia Barbara vein is composed primarily of quartz, which displays low-amplitude serrated grain boundaries and grain boundary bulging. The microstructures are consistent with dynamic recrystallization possibly initially via sub-grain rotation and bulging recrystallization. Mineralization is present as inter-grain phases (Figure 6a, c-f), including pyrite, chalcopyrite, galena, covellite, anglesite ($PbSO_4$) and wulfenite ($PbMoO_4$) as well as

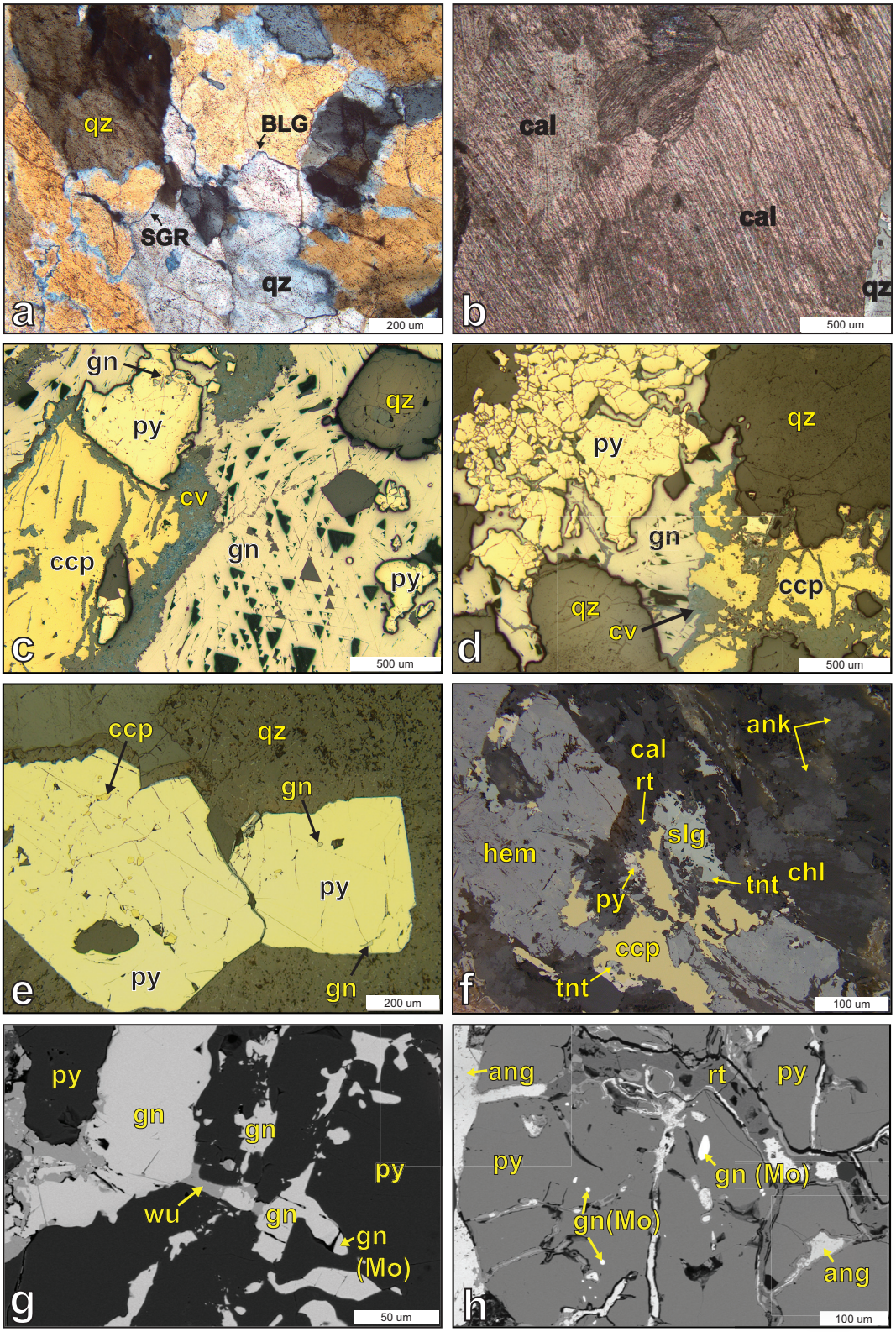
qz
BLG
SGR
qz
a
200 um
cal
cal
qz
b
500 um
gn
py
qz
cv
ccp
gn
py
c
500 um
py
qz
gn
ccp
qz
cv
d
500 um
ccp
qz
gn
py
py
gn
e
200 um
ank
cal
rt
slg
hem
chl
tnt
py
ccp
tnt
f
100 um
py
gn
gn
py
wu
gn
gn
(Mo)
g
50 um
ang
rt
py
py
gn (Mo)
gn(Mo)
ang
h
100 um

Figure 6. Transmitted and reflected light photomicrographs and back-scattered electron photomicrographs from Kallianos ore deposit. (a; E 281778 N 4221317; cross-polarized light) Image of the Agia Barbara (23-03B) vein composed primarily of quartz showing weak bulging. (b; E 280704 N 4220358; cross-polarized light) Calcite in a qz + cal vein of the deposit with thin calcite twins deformation (23-06A). (c, d; same location as a; reflected light) Images showing representative Agia Barbara mineralization (23-03B) with galena, chalcopyrite, pyrite and covellite. (e; E 280055 N 4221579; reflected light) Pyrite with chalcopyrite and galena inclusions of a NNW (V_3) striking vein (23-17A). (f; E 282305 N 282305; reflected light) Mineralization observed in a NNW (V_3) striking veins containing seligmannite, tennantite, chalcopyrite, pyrite, hematite and rutile surrounded by calcite, chlorite and ankerite (23-25A). (g; same location as a; back scatter) Inclusions of molybdenum-rich galena in pyrite within the Agia Barbara vein (23-03B). Galena inclusions are locally bridged by wulfenite. (h; same location as a; back scatter) Mineralization in the Agia Barbara vein (23-03B), showing galena inclusions in pyrite, locally altered to anglesite. Abbreviations: ang, anglesite; ank, ankerite; BLG, bulging grain boundary; cal, calcite; ccp, chalcopyrite; chl, chlorite; cv; covellite; gn, galena; gn (Mo), galena with molybdenum; hem, hematite; py, pyrite; qz, quartz; rt, rutile; SGR, sub-grain rotation; slg, seligmannite; tnt, tennantite; wu, wulfenite.

molybdenum-rich galena, determined via SEM/EDS analysis (Figure 6c-e, g, h). Native gold and silver were not observed in the samples, despite native gold reported from the Agia Barbara vein by Tombros et al. (2021). Mineralized vein samples collected from elsewhere in the deposit hosted an abundance of pyrite containing high amounts of chalcopyrite inclusions, with <40% of the grains containing galena inclusions (Figure 6e, g, h). Sample 23-25A (V_3) possesses a unique mineralization consisting of pyrite, chalcopyrite, hematite, seligmannite ($PbCuAsS_3$) and tennantite ($[Cu, Ag, Zn, Fe]_{12}As_4S_{13}$) (Figure 6f).

Electron microprobe analysis (EMPA) elemental maps were produced to investigate geochemical differences in vein-hosted pyrite of the Kallianos deposit (Figure 7). Two samples were selected that best represent the pyrite observed from the mineralized NNW-striking veins (V_3). Two regions of interest were chosen for pyrite in the Agia Barbara vein; the first (Figure 7, 23-03A[1]) to observe elemental differences in brittle deformed pyrite, and a second (Figure 7, 23-03A[2]) was selected to investigate potential zoning revealed by inclusion-rich chalcopyrite and galena rims observed in this pyrite sample. Sample 23-27A , a separate mineralized NNW-striking V_3 vein, was analyzed to investigate possible compositional differences between finer (20-100 μm) euhedral and coarser (>250 μm) subhedral pyrite clusters.

Pyrite 23-03A[1] exhibits little to no zoning. Concentration of Cu increases in the fractures, with irregular and fanning gradational changes of Co and Ni in the grains, but the chemical maps lack evidence of systematic zoning. No resolvable spatial variations with respect to As, Fe, S, Sb, Se, Si and Zn concentrations were observed. In contrast, pyrite 23-03A[2] shows clear zoning, most notably with the Ni content. Some bands of higher Ni content correspond to zones of elevated Co, and Ni is inversely correlated with Fe. The outermost zones of the pyrite grain possess high

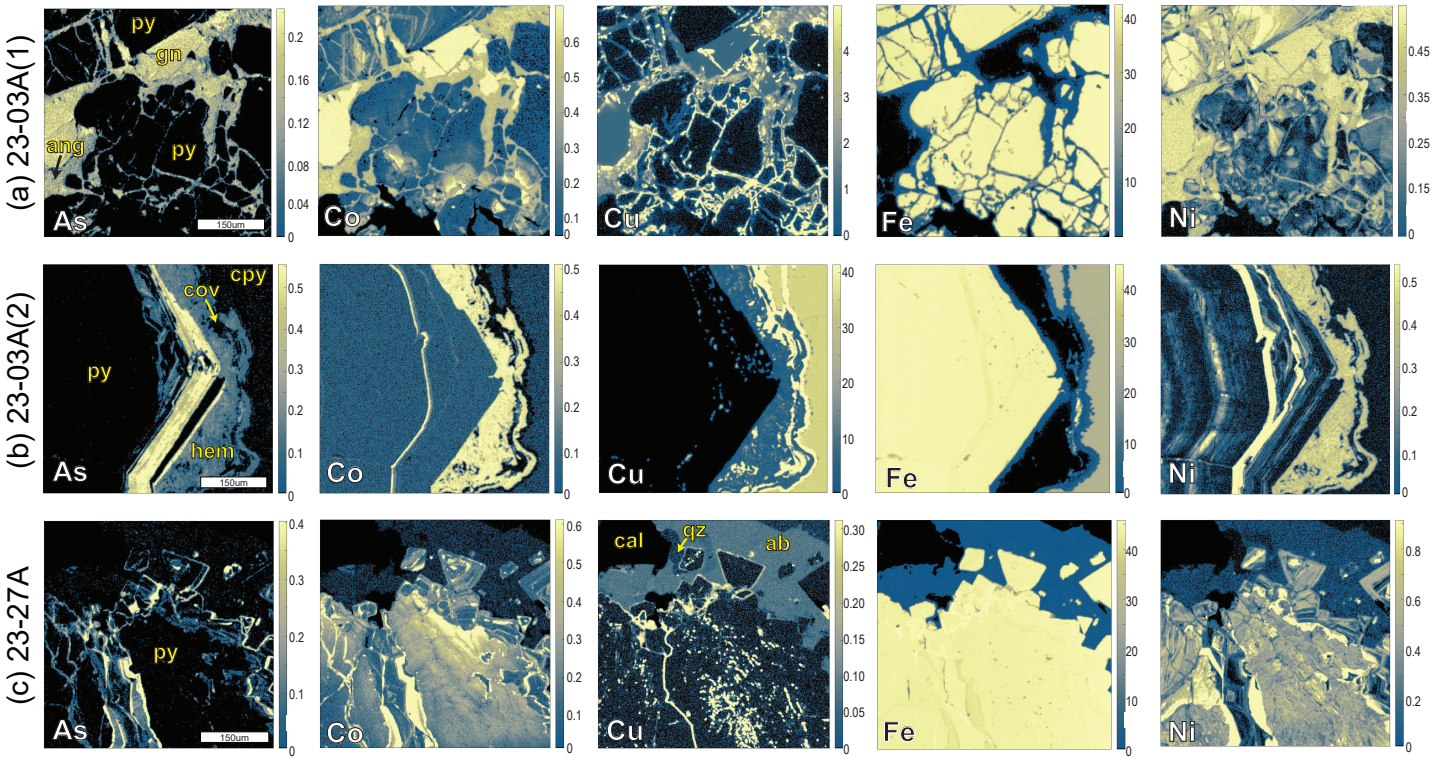

Figure 7. Elemental chemical maps of pyrite grains found in qz ± cal ± ab veins of the Kallianos ore deposit for samples 23-03A and 23-27A showing zoned pyrite with inclusions. Scale bars are in wt% and are different for each map, and black represents areas where element concentrations are below detection limits. Abbreviations: ab, albite; ang, anglesite; cal, calcite; ccp, chalcopyrite; cv; covellite; hem, hematite; qz, quartz; py, pyrite.

concentrations of As associated with an abundance of inclusions. No systematic variation of S, Sb, Se, Si and Zn are evident. The Ni and Co concentrations in sample 23-27A display irregular weak zoning along with As-rich rims, whereas smaller euhedral grains exhibit an abundance of narrow zones; larger subhedral clusters reveal both sweeping gradational zoning and larger bands on the cluster extremities. Inclusions are preferentially distributed toward the center of the large subhedral grain. Concentrations of S, Sb, Se, Si and Zn lack notable differences across the grains.

Two stages of paragenesis were deduced from the qz ± cal ± ab vein chemical mapping and microstructures of the V_3 veins (Figure 8). Stage I is defined by the formation of coarse-grained pyrite (py1), chalcopyrite (cpy1), and galena (gn1), whereas stage II is associated with the formation of a nearly identical assemblage of pyrite (py2), chalcopyrite (cpy2), galena (gn2), but includes several additional trace minerals. Minerals belonging to stage 2 are challenging to visually differentiate from their stage 1 counterparts, and are most easily distinguished using mineral chemistry for the two pyrite phases. The distinction between py1 and py2 is most clearly obvious in the elemental composition maps, where py2 forms a rim on py1 (Figure 7).

In stage I, py1 is subhedral, exhibits poor 2-direction cleavage planes and is relatively inclusion-poor relative to py2 (Figure 6c-e, 7). Inclusions of cpy1 and gn1 are present on the cleavage planes of py1. Cpy1 is usually intergrown with py1 and is only clearly observed in the Agia Barbara vein (23-03B) and in sample 23-25A (Figure 6c-d, f). Grain size of cpy1 is difficult to determine due to near-comprehensive replacement by covellite, but remnants of cpy1 range between 200 µm-1 mm. Coarse grained, subhedral gn1 (500 µm-3 mm) displays weak 2-direction cleavage and irregular boundaries (Figure 6c-d).

In stage 2, py2 is As-rich, comparatively euhedral, generally contains abundant cpy2 and gn2 inclusions and is finer grained than py1 (Figure 6e, 7). Cpy2 is present as spherical inclusions

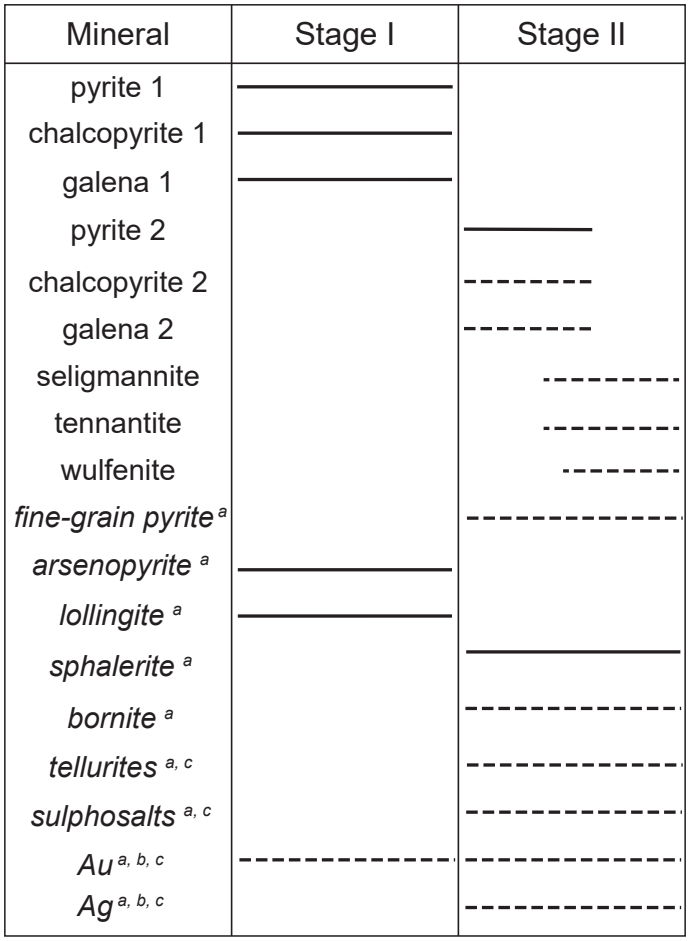

Figure 8. Summary of paragenetic relationships documented for the mineralized (V_3) qz ± cal veins of the Kallianos ore deposit. Dashed lines represent trace occurrences minerals. Additional minerals identified by [a]Tombros et al. (2021); [b]Valvelidis and Michailidis (1990); [c]Voudouris et al. (2011). See text for detailed descriptions.

ranging from 3-40 μm (Figure 6e). Gn2 (1-25 μm) is rich in Mo and forms spherical to blocky inclusions in py2 and cpy2 grains (Figure 6e, g-h). Seligmannite and tennantite were only observed in sample 23-25A (Figure 6f). Seligmannite (20-100 μm) is subhedral, sometimes acicular, and associated with rutile and tennantite, the latter is blocky and ~10 μm in diameter. Trace wulfenite, ~20 μm in diameter, appears between galena inclusions in the Agia Barbara sample (Figure 6g). Oxide and alteration minerals also occur, such as hematite (Figure 6f), anglesite ($PbSO_4$, Figure 6h), rutile (Figure 6f) and covellite (Figure 6c,d).

Geochronology and stable isotope geochemistry

$^{40}Ar/^{39}Ar$ geochronology

White mica $^{40}Ar/^{39}Ar$ geochronology was performed to resolve the timing of brittle-ductile deformation and mineralization of the Kallianos deposit (Table 2). White mica were taken from both the host rock and the vein halos of the qz ± cal ± ab veins. Six host rock samples and six vein samples (one V_1 and five V_2/V_3) were selected for multiple single-grain total fusion $^{40}Ar/^{39}Ar$ analysis (Schneider et al., 2018; Uunk et al., 2018), with eight mica grains analyzed per sample. Mineralized veins were prioritized over barren veins, where the white mica show no preferred orientation and are heterogenous in size (5-500 μm in thickness). All but one host rock sample are quartz-mica schists, with foliated elongated white mica aggregates (250-400 μm), whereas the other host rock sample (23-18A) is a schistose impure marble within the qz-wm schists.

White mica from vein haloes yielded weighted mean ages between 20.9 ± 0.3 Ma and 25.8 ± 0.4 Ma, with sample 23-05A providing more dispersed single crystal dates between c. 28 Ma and c. 42 Ma (Figure 9). This single vein displays highly irregular and non-planar boundaries, corresponding to V_1. Thin section observations revealed the sample contained an abundance of

Table 2. Summary of white mica $^{40}Ar/^{39}Ar$, and zircon (U-Th)/He geochronology from the Kallianos ore deposit, Evia, Greece

	sample	mica $^{40}Ar/^{39}Ar$ age (Ma)[a]	2σ (Ma)[b]	MSWD[c]	mica $^{87}Rb/^{87}Sr$ date (Ma)[a]	2σ (Ma)	MSWD[c]	zircon (U-Th)/He date (Ma)[a]	2σ (Ma)	MSWD[c]
vein	23-05A	38.7	0.6	13	-	-	-	-	-	-
	23-09A	20.9	0.3	7.9	21.3	2.9	1.0	-	-	-
	23-15A	25.3	0.4	0.8	-	-	-	-	-	-
	23-22A	23.6	0.4	3.8	-	-	-	-	-	-
	23-23B	22.1	0.4	2.7	-	-	-	-	-	-
	23-28A	25.8	0.4	1.2	-	-	-	-	-	-
host rock	23-03A	19.3 - 29.4	0.4 - 0.6	-	-	-	-	-	-	-
	23-07A	30.5	0.5	3.8	25.7	2.7	1.2	-	-	-
	23-08A	-	-	-	-	-	-	10.8	0.3	8.1
	23-10A	25.9	0.5	4.9	-	-	-	-	-	-
	23-13B	20.3	0.3	1.2	-	-	-	-	-	-
	23-18A	23.7	0.3	10.0	-	-	-	-	-	-
	23-19A	25.4 - 39.6	0.5 - 0.8	-	-	-	-	14.1	0.5	6.8

[a] Ages noted as a weighted mean of multiple grain analyses. [b] 2σ error was calculated as 2% of each data samples and reported as weighted mean. [c] Weighted mean calculations for sample ages which yield MSWD ≤ 13 are reported as a single weighted mean age, and calculations returning MSWD >13 are presented as ranges of single-grain dates.

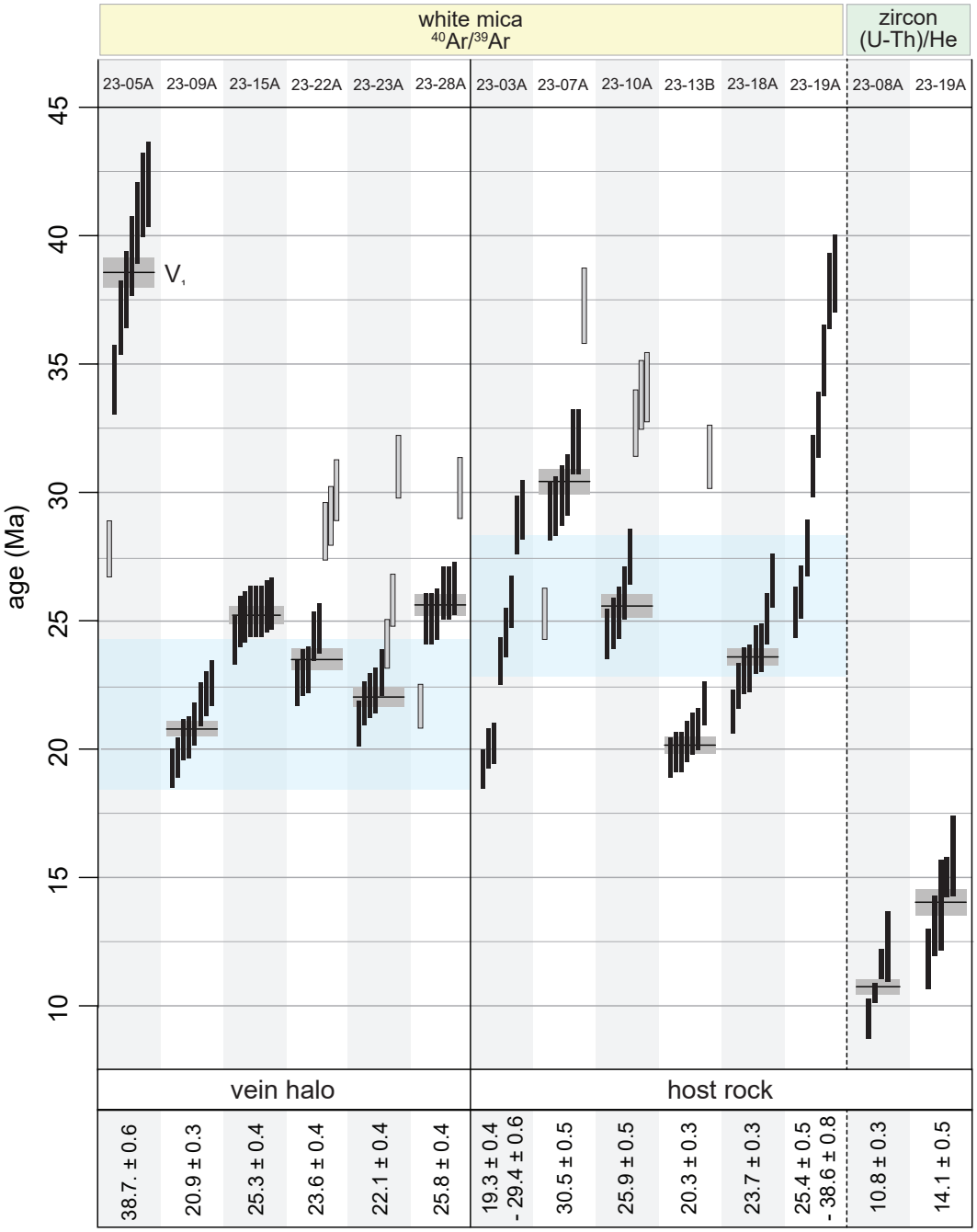

Figure 9. Summary of new white mica $^{40}Ar/^{39}Ar$ and zircon (U-Th)/He data from the Kallianos ore deposit in southern Evia. Mica $^{40}Ar/^{39}Ar$ data are divided into vein halo hydrothermal mica (left) and metamorphic mica forming part of the host rock (right). Each vertical bar represents a single analysis at 1σ. Light grey bars were not included in the weighted mean calculation. Horizontal black lines for each sample represent the weighted mean ages, where applicable, whereas grey horizontal boxes show propagated analytical and systematic errors for the weighted mean ages. Horizontal blue bars show white mica $^{87}Rb/^{87}Sr$ isochron dates calculated for samples 23-09A (vein-hosted) and 23-07A (host rock) (Figure 10).

chlorite and low quantities of white mica; therefore, analysis of finely intergrown chlorite-mica may account for the dispersion of dates in this sample. However, Ca/K and Cl/K values for this sample do not differ considerably from those obtained from white mica in other samples.

White mica from the host rocks produced considerably more variable dates, with sample weighted mean ages between 20.3 ± 0.3 Ma and 30.5 ± 0.5 Ma. White mica from samples 23-03A and 23-19A yielded more dispersed dates, ranging from c. 20 Ma to c. 40 Ma. Dispersion in some samples, where the older spurious single crystal dates were not included in the weighted average calculation such as 23-22A and 23-10A, likely indicate analysis of mixed age populations, but additional data are required to substantiate this hypothesis (Figure 9).

$^{87}Rb/^{87}Sr$ geochronology

Two samples were selected for in-situ white mica $^{87}Rb/^{87}Sr$ geochronology (Table 2; Figure 10). The in-situ approach allowed for deliberate targeting and comparison of foliation-defining white mica in the host rock and microstructurally distinct vein-proximal mica. Sample selection for $^{87}Rb/^{87}Sr$ analysis was informed using the $^{40}Ar/^{39}Ar$ data. Two representative samples were chosen to produce $^{87}Rb/^{87}Sr$ isochrons from vein-proximal mica (23-09A) and from a schistose host rock (23-07A). The vein halo in sample 23-09A also displayed euhedral-subhedral pyrite (30-700 μm) mineralization alongside abundant, randomly oriented white mica (10-100 μm in thickness). The sample yielded a $^{87}Rb/^{87}Sr$ isochron date of 21.3 ± 2.9 Ma (MSWD: 1.0; n: 79). The sample selected to represent host rock white mica (23-07A) contained comparatively coarse grained mica (100-300 μm), and yielded an isochron date of 25.7 ± 2.7 Ma (MSWD: 1.2; n: 70).

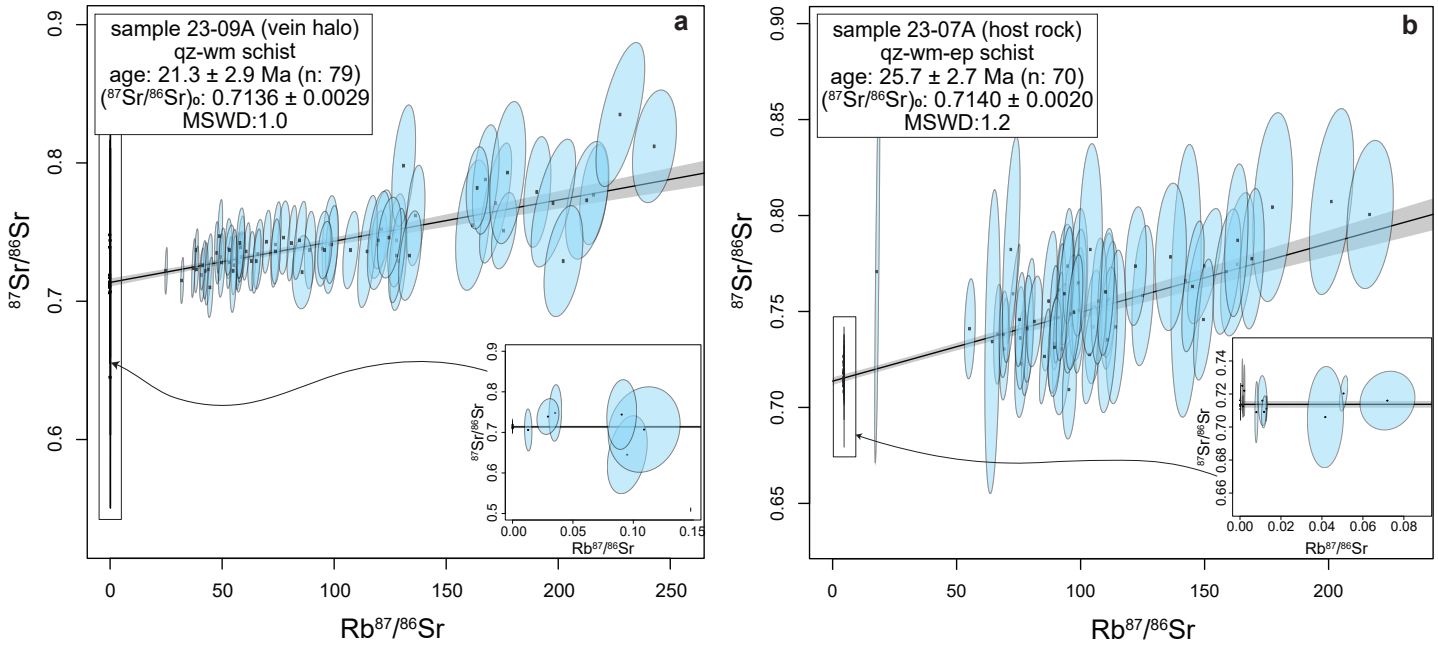

Figure 10. In situ white mica $^{87}Rb/^{87}Sr$ isochrons from the Kallianos deposit. (a) Hydrothermal white mica for a qz ± cal vein halo (23-09A); (b) White mica in a qz-wm-ep schist host rock (23-07A). Inset shows analyses at the origin.

(U-Th)/He geochronology

Zircon (U-Th)/He (ZHe) geochronology was used to determine the timing of cooling of the host rocks below ~200°C (Reiners et al., 2004), at which most rocks deform via brittle mechanisms. Two samples produced viable zircons for analysis (Table 2; Figure 9). Sample 23-08A is a mica schist from the Kallianos deposit. Zircons from this sample were subhedral, with rough surfaces and moderate staining, and an average size of 110 μm in length and 60 μm in width. Four single grain analyses yielded ZHe dates between 9.6 ± 0.4 Ma and 12.4 ± 0.7 Ma, producing a weighted mean age of 10.8 ± 0.3 Ma (MSWD: 8.1). Sample 23-19A is a quartz-mica schist collected directly structurally below the NCDS. The sample yielded euhedral, translucent zircon with minimal fracturing or staining and an average length of 138 μm and width of 80 μm. Five single grain analyses yield ZHe dates between 11.9 ± 0.6 Ma and 15.9 ± 0.8 Ma, and a weighted mean age of 14.1 ± 0.6 Ma (MSWD: 6.8). Effective uranium (eU) values range between 200 and 900 ppm for both samples, and the average effective spherical radii (ESR) is slightly smaller (~38 μm) for 23-19A compared to 23-08A (~51 μm). Nonetheless, neither eU nor ESR exhibit a strong correlation with measured ZHe dates.

Carbon and oxygen isotope geochemistry

Carbon and oxygen stable isotope geochemistry of vein-hosted calcite was conducted to help elucidate the potential source of fluids in the qz + cal veins of the Kallianos deposit. Carbon and oxygen isotopes are used to indirectly resolve the fluid source and the evolution of the fluid-rock interaction of the vein, since different fluid reservoirs are isotopically distinct (Bowman, 1998). Seven mineralized and two unmineralized vein samples were selected, including the Agia Barbara vein (Figure 11), which supplements the six calcite samples reported in Tombros et al. (2021).

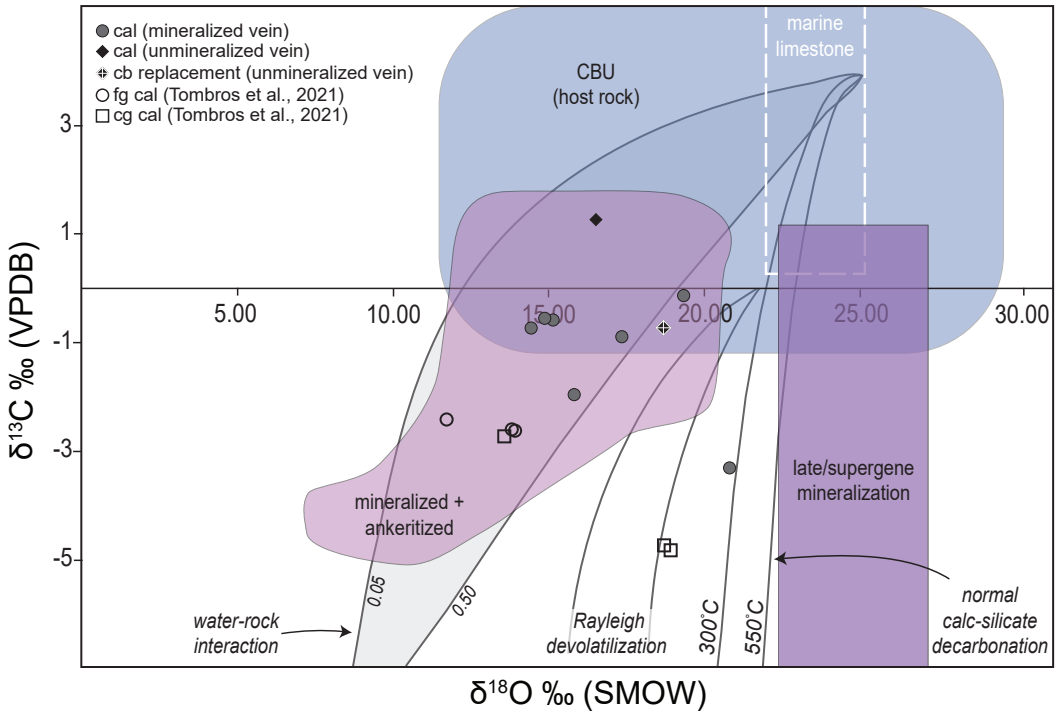

Figure 11. Oxygen vs carbon isotope composition of calcite from the Kallianos ore deposit. Grey filled circles are calcite from mineralized qz-cal vein samples, black diamonds are calcite from unmineralized veins, and a white cross indicates a carbonate replacement sample (23-22B). Black open circles represent fine-grained calcite (fg cal) and open squares represent coarse-grained calcite (cg cal) from the deposit reported in Tombros et al. (2021). Dashed marine limestone box is from Bowman (1998). Blue CBU (host rock) box combines data of the Cycladic Blueschist Unit on Naxos, Tinos, and Sifnos from Baker and Matthews (1995), Ganor et al. (1994), Ganor et al. (1996), Matthews et al. (1999) and Schliestedt and Matthews (1997). Pink and purple polygons depicting mineralized + ankeritized and late/supergene mineralized veins at Lavrion from Bonsall et al. (2011) and Berger et al. (2013). Grey polygon highlights the range of $\delta^{13}C$ and $\delta^{18}O$ trends (0.05-0.5 fraction) produced by continuous magmatic water-carbonate rock interaction from Bowman (1998). Straight and curved lines represent the calculated Rayleigh devolatilization and batch devolatilization from Baumgartner and Valley (2001). Curved solid black lines are normal calc-silicate decarbonation lines at 300°C and 550°C from Bowman (1998). See Table 1 for $\delta^{13}C$ V-PDB (‰) and $\delta^{18}O$ V-SMOW (‰) values.

Calcite analyses resulted in $\delta^{18}O$ values (VSMOW) ranging from 14.43‰ to 19.31‰, and $\delta^{13}C$ values (VPDB) from -1.96‰ to 0.40‰, with the exception of sample 23-17A which yielded a $\delta^{18}O$ value of 20.79‰ and a $\delta^{13}C$ value of -3.31‰ (Table 1). The calcite in sample 23-17A contains a high degree of ankeritization and type III to IV twins (Ferrill et al., 2004). The samples broadly overlap with the mineralized and ankeritized field of veins from the Lavrion deposit (Berger et al., 2013; Scheffer et al., 2017), the continuous magmatic water-carbonate rock exchange trends of Bowman (1998), and with data from CBU marbles on Naxos, Tinos and Sifnos (Baker and Matthews, 1995; Ganor et al., 1994; Ganor et al., 1996; Matthews et al., 1999; Schliestedt and Matthews, 1987).

Discussion

Structural evolution

Field observations of the Kallianos Au-Ag-Te deposit are broadly consistent with an interpretation that its formation coincided with extensional tectonics influenced by regional low-angle normal faulting. Brittle-ductile shear bands recording top-to-NE kinematics are present throughout the Kallianos deposit, consistent with structures observed elsewhere in the footwall of the NCDS (Jolivet et al., 2010). The qz ± cal veins and joint sets that occur within the Kallianos deposit are likewise observed adjacent to the NCDS exposure, with orientations and cross-cutting relationships conserved across both localities (Fig 3c-g, 5e-h). The mode-I veins (V_2, V_3) are orthogonal to the regional sub-horizontal, NE-SW stretching lineations that track ductile deformation related to Miocene extensional tectonics (Figure 4; Gautier and Brun, 1994; Jolivet et al., 2010). This geometric relationship provides strong evidence that the veins in the Kallianos are

developed within the regional stress field expected to coincide with the ductile-then-brittle strain history accommodating extension along the NCDS.

En-echelon vein sets (in the Kallianos deposit) and sigmoidal vein geometries (in the immediate footwall of the NCDS) demonstrate local sinistral shearing and left-lateral strike-slip components (Figure 3e, 5f, g). Sigmoidal vein tips are oriented NW-SE (i.e., parallel to V_2), with corresponding cores rotated by 90°, striking NE-SW. En-echelon veins in the Kallianos area are geometrically linked with NNW-striking (i.e., V_3-parallel) shear surfaces, together defining a sinistral, left-lateral pull-apart geometry. The shared occurrence of structures apparently recording sinistral transcurrent deformation provides another structural commonality between the Kallianos deposit and the NCDS. Moreover, these structures clearly exhibit characteristics consistent with ductile or brittle-ductile deformation, and the inference that V_2 and V_3 veins opened under brittle-ductile conditions is supported by numerous other structures in the Kallianos area. For instance, wall rock at vein margins is commonly deflected (Figure 3d, f), suggesting ductile deformation of wall rock in response to opening or subsequent rotation of the veins. Conjugate joint sets are separated by an acute angle approaching 90°, consistent with Von Mises rather than Mohr-Coulomb behavior, which likewise evinces ductile rather than brittle strain accommodation mechanisms (Figure 3i). Kink bands are commonly developed parallel to vein sets, further suggesting these structures accommodated complementary shortening to the dilation associated with tension gash formation via brittle-ductile mechanisms (Figure 3d, 5h). Veins, including some layer-parallel carbonate replacement type veins associated with the Kallianos mineralization (Tombros et al., 2021), are locally dissected by shear bands, or stretched into pinch-and-swell and boudinage structures (Figure 3b). Moreover, microstructures observed in vein quartz and calcite suggest both phases underwent minor dynamic recrystallization, accommodated in quartz

principally by grain boundary bulging and in calcite by type-III and type-IV deformation twins. These microstructures are consistent with deformation at temperatures of 300-350°C and 170-300°C, respectively, conditions that likely reflect brittle-ductile strain accommodated in the quartz-, calcite- and phyllosilicate-rich rocks hosting the Kallianos mineralization. The observations outlined here overwhelmingly indicate that the mineralized veins developed within the brittle-ductile transition zone in response to transitory fluid overpressure, consistent with veins documented elsewhere on southern Evia (Ducharme et al., 2024; Nüchter and Stöckhert, 2007), and with conditions at which orogenic gold mineralization typically occurs (e.g., Goldfarb and Groves, 2015).

Structures apparently related to strike-slip deformation do not typically develop in the stress field coinciding with extension and low-angle detachment faulting. Nevertheless, the ductile to brittle-ductile style of deformation evident in the sinistral sigmoidal and en-echelon veins clearly indicates these structures pre-date the latest (brittle) stages of deformation associated with the NCDS. A possible explanation for these brittle-ductile structures would require that the NCDS produced a strain geometry that departed from ideal monoclinic simple shear, as is considered likely for most naturally deformed systems (Oriolo et al., 2024). A coaxial strain component could induce formation of conjugate sets of strike-slip shear planes orthogonal to the slip (detachment) plane. However, the conjugate dextral set of shear surfaces was not observed within the field area. Menant et al. (2013) described such a situation from Mykonos, where a conjugate set of mineralized dextral and sinistral shears is developed below the NCDS exposed on the island. These authors likewise explain this phenomenon using either a coaxial component of strain, or alternatively suggest a stress field rotation within the detachment such that σ_1 became oriented (sub-)parallel to the detachment plane. Because of the central position of Mykonos relative to the

strike length of the NCDS, the absence of conjugate dextral structures on Evia may simply be due to its distal, northerly location along strike of the structure, preferentially developing the sinistral-sense planes. Moreover, mineralized NW-SE striking barite veins on Mykonos were emplaced contemporaneously with the c. 14 Ma monzogranitic to granodioritic intrusion, crossing the brittle-ductile transition between c. 14-9 Ma during unroofing, which was facilitated by exhumation accommodated by the NCDS (Brichau et al., 2007; Menant et al., 2013). The striking similarities in structure and timing (see below) at these two mineralized exposures of the NCDS suggest that the two occurrences developed within analogous deformation regimes, controlled by the overlying major structure. Likewise, in Lavrion, a c. 10 Ma granodioritic stock is accompanied by WNW-ESE and WSW-ENE-trending dikes, which are perpendicular to the stretching lineations associated with the WCDS (Berger et al., 2013; Skarpelis, 2002). These comparable examples underscore the geometric dependence of local brittle tensile to brittle-ductile structures during detachment-accommodated extension.

Timing of deformation and vein formation

White mica $^{40}Ar/^{39}Ar$ and $^{87}Rb/^{87}Sr$ geochronometers are sensitive to isotopic resetting due to factors such as recrystallization (deformation), thermal diffusion (metamorphism), and neocrystallization (hydrothermal activity), making them useful tools to date these phenomena (e.g., Barnes et al., 2023; Cossette et al., 2015; Dunlap et al., 1991; Freeman et al., 1997; Larson et al., 2023). Using the $^{40}Ar/^{39}Ar$ and $^{87}Rb/^{87}Sr$ systems in tandem can further elucidate the timing of these processes, as the chronometers may exhibit differential sensitivity to resetting (Gyomlai et al., 2023; Barnes et al., 2024). New white mica $^{40}Ar/^{39}Ar$ and $^{87}Rb/^{87}Sr$ geochronology has yielded

dates from the Kallianos deposit that largely conform to the understanding of the deformation history of the CBU and the timing of the vein emplacement.

Host rocks preserve white mica that record $^{40}Ar/^{39}Ar$ single grain dates that span from early Eocene (c. 45 Ma) to early Miocene (c. 19 Ma, Figure 9). Whereas most samples exhibit one predominant population of single-grain dates, some samples display considerable scatter that typically manifests as a dispersion of older (i.e., Eocene) $^{40}Ar/^{39}Ar$ dates. A kernel density plot of the $^{40}Ar/^{39}Ar$ ages from the Kallianos deposit host rock (Figure 12) shows largely a single population, which displays slightly more variability than the vein halo white mica dates. There is excellent agreement between the mean age of the host rock white mica $^{40}Ar/^{39}Ar$ data and the $^{87}Rb/^{87}Sr$ isochron date of 25.7 ± 2.7 Ma. The Rb-Sr data yielded a robust MSWD value but larger error compared to the $^{40}Ar/^{39}Ar$ data. The host rock white mica are relatively (visually) homogeneous and define the dominant foliation (Figure 3a), suggesting that the mica formed during regional greenschist deformation (Cossette et al., 2015). The CBU accommodated progressive deformation throughout its Miocene greenschist facies overprint, and the $^{40}Ar/^{39}Ar$ dates from the Cyclades are widely interpreted as reflecting deformation-induced recrystallization and resetting (e.g., Ducharme et al., 2022; Laurent et al., 2021; Schneider et al., 2018, Uunk et al., 2018). The dispersion in the white mica $^{40}Ar/^{39}Ar$ dates could be explained in two ways. First, the host rocks contain some smaller decussate white mica (Figure 3a, S1b). Since the rock samples were crushed during preparation, the microstructural context of the phase is lost and it is possible that mica from a subordinate population was selected and analyzed, potentially contributing to the observed age variation. A second explanation would be that a subpopulation of the white mica did not undergo Miocene isotopic resetting during greenschist facies metamorphism (thermal diffusion) and deformation (recrystallization). This would result in older white mica dates (e.g.,

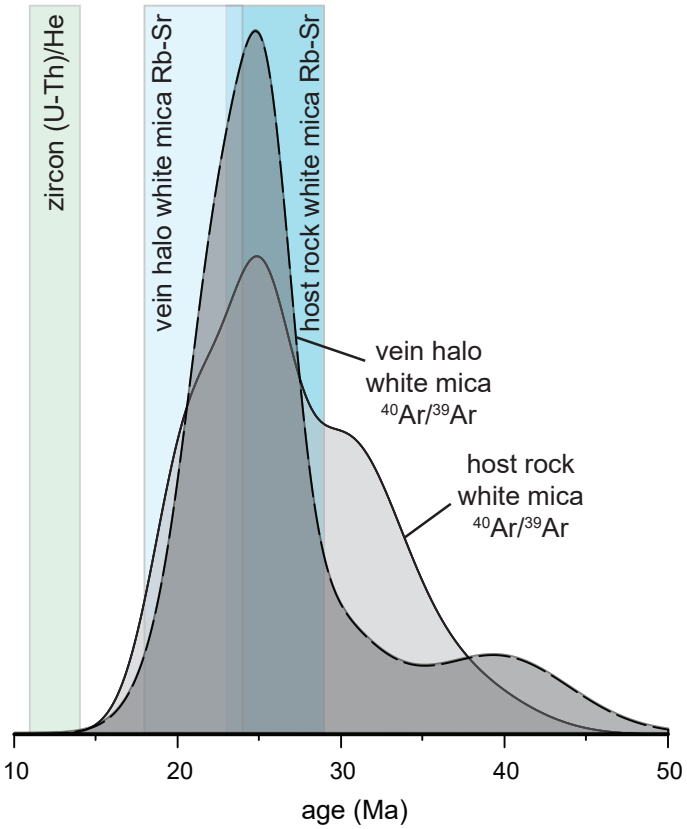

Figure 12. Kernel density curve for $^{40}Ar/^{39}Ar$ geochronology data of vein halo white mica (dark grey dashed, n: 48) and host rock white mica (light grey, n: 48). Both vein halo white mica and host rock white mica have kernel bandwidths of 2. Green box represents zircon (U-Th)/He cooling dates (10.8 ± 0.3 Ma to 14.1 ± 0.6 Ma). Light blue and darker blue boxes correspond to in-situ white mica $^{87}Rb/^{87}Sr$ data for vein halo white mica (21.2 ± 2.9 Ma) and host rock white mica (25.7 ± 2.7 Ma).

sample 23-19A, Figure 9) that preserve a HP-LT metamorphic signature dated at 52-40 Ma (Bröcker et al., 2004; Jolivet and Brun, 2010; Lagos et al., 2007; Putlitz et al., 2005; Schneider et al., 2011; Wijbrans et al., 1990). Nevertheless, the host rock white mica $^{40}Ar/^{39}Ar$ data yielded a dominant population of early Miocene dates that likely reflects the timing of greenschist facies deformation on southern Evia during exhumation facilitated by the NCDS (Ducharme et al., 2022; Ring et al., 2010; Schliestedt and Matthews 1987; Shaked et al., 2000).

The white mica $^{40}Ar/^{39}Ar$ vein halo data resulted in less age dispersion than the host rock data, reflected in the kernel density plot, ranging from c. 21-26 Ma (Figure 9, 12). $^{87}Rb/^{87}Sr$ isochron dates for the white mica vein halo provides an age of 21.3 ± 2.9 Ma which is within error of the age provided by the $^{40}Ar/^{39}Ar$ (Figure 9, 12). Sample 23-05A provides older and more dispersed single crystal $^{40}Ar/^{39}Ar$ dates, between c. 28 Ma and c. 42 Ma, highlighted as the smaller, second population on the kernel density diagram (Figure 9, 12). This particular single vein exhibits highly irregular and non-planar boundaries, unlike most veins from the deposit, and is concordant to foliation. The age of c. 39 Ma likely corresponds to the earliest V_1 vein generation, which developed as layer-parallel structures. The microstructures of V_2 and V_3 indicate that these veins developed near simultaneously in a single fluid event, and the physical aspects of the vein halo white mica also reflects a single event. The undeformed and decussate white mica within the vein margins lack schistosity, and formed syn- or post-greenschist metamorphism, when recrystallization and foliation development would have occurred, such as in the host rock. The physical and structural characteristics of the veins and white mica within the vein halo, combined with less dispersed $^{40}Ar/^{39}Ar$ data that are concordant with the $^{87}Rb/^{87}Sr$ data, strongly suggests that the veins crystallized in a single event, and therefore the ages represent the timing of white mica neocrystallization. Similar conclusions have been drawn from other mica-bearing veins in

the Cyclades, reflecting the timing of hydrothermal fluid flow (Ducharme et al., 2024; Muñoz-Montecinos et al., 2024).

Considering the dispersion, the vein halo and host rock dates are within error of each other. The host rock contains shear bands that formed under brittle-ductile conditions during greenschist facies deformation - the same conditions under which the white mica recrystallized. Previous studies have linked the CBU host rock deformation to exhumation along detachment fault systems such as the NCDS (Grasemann et al., 2012; Jolivet et al., 2010, Laurent et al., 2015; Mehl et al., 2005; Menant et al., 2013). Structural observations indicate that V_2 and V_3 veins also formed under brittle-ductile conditions, likely influenced by the overlying detachment system. These observations suggest that the neocrystallization of white mica in the vein halos occurred during the same tectonic events that triggered deformation-induced recrystallization of white mica in the host rock, which explains their statistically comparable dates.

Zircon (U-Th)/He weighted mean ages reported here of 10.8 ± 0.3 Ma and 14.1 ± 0.6 Ma are used to evaluate the relative timing of cooling to upper crustal temperatures (~200°C), corresponding in this case with the onset of brittle deformation. If the white mica dates have resolved the timing of ductile deformation and vein emplacement during the earliest Miocene, the zircon (U-Th)/He dates suggest cooling to brittle conditions, c. 10 Myr after the Kallianos deposit formed. Cooling and exhumation at this time on southeastern Evia is comparable to cooling recorded on Andros and Tinos, ranging from c. 14-9 Ma, but is slightly later than the brittle conditions recorded in central Evia at c. 18-15 Ma (Ducharme et al., 2022; Shin, 2014).

To summarize, these new data reveal that $^{87}Rb/^{87}Sr$ and $^{40}Ar/^{39}Ar$ dates resolve the formation of the veins (V_2, V_3) in the early Miocene, at c. 21-26 Ma, while the rocks resided in the brittle-ductile regime. These ages are consistent with the brittle-ductile deformation sustained by the host

rock during greenschist metamorphism between c. 20-30 Ma, comparable to the timing of deformation accommodated in the Cyclades by the NCDS throughout the Miocene (Huet et al., 2015; Jolivet et al., 2010). Lower temperature cooling ages indicate the CBU on southeastern Evia, and consequently the Kallianos deposit, were exhumed into the brittle crust by the late Miocene. Consequently, the 8 Ma pyrite Rb-Sr date of Tombros et al. (2021) is far too young to fit into this framework, and likely does not reflect the timing of magmatic activity nor the deposition of the Kallianos deposit. The conformity between structures in the deposit and in the vicinity of the NCDS, coupled with evidence that these structures overwhelmingly record brittle-ductile deformation that was only sustained until the middle Miocene, provides compelling evidence that the veins formed during post-orogenic exhumation, with the NCDS playing a significant role in creating structural traps and channelizing the fluids.

Fluid source

Most deposits within the CMD have been spatially and temporally linked to Miocene magmatism, with notable examples including Lavrion, Mykonos, and Tinos (Figure 1; Berger et al., 2013; Bonsall et al., 2011; Skarpelis, 2002; Tombros et al., 2008; Wind et al., 2020). These deposits are directly surrounding, if not intimately part of, their parent intrusion, and compounding geochemical evidence implies a genetic relationship between the two (Berger and al., 2013; Bonsall et al., 2011; Menant et al., 2013; Skarpelis, 2002). A similar relationship has been proposed for the Kallianos Au-Ag-Te deposit, either with a yet undiscovered intrusion below current erosional levels, or with the distal Plaka granodiorite of Lavrion, were detachment-related structures serve as fluid conduits in the latter scenario (Tombros et al., 2021; Vavelidis and Michailidis, 1990; Voudouris et al, 2011). Notably, field-based evidence of such a granitoid body

has not been reported on southeastern Evia or northern Andros, nor even peripheral evidence of Miocene intrusive activity (i.e., dikes; Latsoudas et al., 1997), despite such small-volume intrusions being well represented on Tinos and Lavrion (Berger et al., 2013; Bonsall et al., 2011; Skarpelis, 2002). The nearest magmatic activity on Evia is the relatively small (~10 km^2) Miocene Oxylithos volcanic complex in east-central Evia, located ~60 km NW of the Kallianos deposit (Figure 2, Pe-Piper and Piper, 1994), effectively as distant as the Lavrion (~60 km) and Tinos (~85 km) intrusions. Furthermore, host rocks of the Kallianos deposit do not display pervasive alteration typically observed at intrusion-related deposits. For instance, the Plaka deposit exhibits propylitic and sericitic alteration within the contact aureole of the granodiorite, which also generated garnet-hedenbergite exoskarns up to several kilometres away (Berger et al., 2013; Skarpelis, 2002; Skarpelis and Lüders, 2007). On Mykonos, the granitic wall rock is sericitized and the presence of silica breccia and a silica cap implies a deeply eroded epithermal system (Menant et al., 2013; Skarpelis, 2002). Unlike these deposits, chloritic alteration within the Kallianos deposit is weak and limited to occasional half-metre-scale haloes adjacent to veins (Figure 3c-g), with no evidence of a contact aureole like those described elsewhere in the Cyclades (Skarpelis, 2002).

Numerous studies have conducted Pb-isotopic analyses on the Kallianos deposit and its surrounding deposits in the CMD (e.g., Bonsall et al., 2011; Scheffer et al., 2017; Tombros et al., 2007, 2008, 2015, 2021; Vavelidis et al., 1985; Voudouris et al., 2011; Wind et al., 2020). Galena $^{206}Pb/^{204}Pb$ isotopes throughout the Cyclades reported in Wind et al. (2020) revealed a geographical division of Pb-isotope values that track the fluid source(s) through the CBU that correlates well with the inferred trace of the TCT (Figure 1, Grasemann et al., 2017). The Pb-isotope data from Kallianos are comparatively less radiogenic and have distinct $^{206}Pb/^{204}Pb$ signatures (Tombros et al., 2021) comparable to deposits proposed to have been derived from fluid

interaction with the Cycladic Basement (Wind et al., 2020). By contrast, the more radiogenic deposits of the western Cyclades, which include Lavrion, Serifos, and Milos, likely attained their isotopic signature from interaction with the Lower Cycladic Blueschist Nappe (Figure 1, Wind et al., 2020). It is therefore improbable that mineralizing fluids of the Kallianos deposit were derived from the Plaka granodiorite, as proposed by Tombros et al. (2021). Instead, Pb-isotope data (Tombros et al., 2021; Wind et al., 2020) are consistent with fluid interaction with the deeper Cycladic Basement.

Sulphide mineral chemistry maps point to a two-stage paragenesis and metal enrichment for the Kallianos veins. Tombros et al. (2021) likewise described two generations of quartz and calcite (Figure 8). Core-to-rim variations in pyrite chemistry (Figure 7) illustrate the changing metal contents of the fluids. Pyrite that crystallized during stage II is more concentrated in metalloids such as As and comparatively enriched in heavy metals like Co and Ni demonstrating the evolution and enrichment of the fluids during the formation of the veins. Enrichment of base and heavy metal content, when taken as an isolated characteristic, does not alone support a magmatic fluid input into orogenic gold deposits (Goldfarb and Pitcairn, 2022). It may instead reflect the local wall rock alteration reactions with sulfur in the hydrothermal fluids (Goldfarb and Pitcairn, 2022), which corresponds with the presence of more mafic protoliths locally, such as in the adjacent nappe of the Ochi Unit.

Calcite C- and O-isotopic data provide further insight into the vein fluid interaction with the wall rock. Despite calcite C- and O-isotope data of the Kallianos deposit plotting within the mineralized and ankeritized fields of other Cycladic deposits (Figure 11), the heaviest isotopic values also overlap with host rock isotopic data from the CBU, defining a trend toward lighter signatures that follows processes predicted to accompany Rayleigh devolatilization (Figure 11).

Although Tombros et al. (2021) suggested a limited interaction with the CBU wall rock during vein sealing, the observed shift toward lighter $\delta^{13}C$ values can be associated with increased fluid-rock interaction of graphite-bearing metasedimentary rock, which is a common component of the CBU (Figure 11; Baziotis et al., 2020; Bowman, 1998; Rice and Grasemann, 2016). Siebenaller et al. (2013) explained a similar scenario for quartz veins on Naxos. They defined three generations of brittle to ductile veins in the host rock that formed at different stages of Miocene exhumation. The authors proposed, as fluid source for the veins, an interaction between decarbonation reactions of the marbles and oxidation of small amounts of graphite from the schists, similar to the marbles and schists occurring in the Styra Unit on Evia. They attest that this could be the most effective process to produce their slightly negative $\delta^{13}C$ values in disequilibrium with surrounding host rocks. we envision a similar scenario at the Kallianos deposit, with lighter $\delta^{18}O$ values compared to the CBU (host rock) field, possibly indicating greater interaction with meteoric water.

Overall, the available isotopic data do not offer a definitive indication of source of the mineralizing fluids, and thus do not strictly require a magmatic source as proposed by Tombros et al. (2021). Since the isotope data from Kallianos conform to the general trends throughout the northern CMD (Berger et al., 2013; Scheffer et al., 2017; Wind et al., 2020), it appears that the Kallianos mineralizing fluids were likely subjected to protracted interaction and isotope exchange with metamorphic host rocks. This thereby strengthens the argument in favor of a trend in lighter C- and O-isotope compositions as a result of Rayleigh devolatilization. The CBU host rock of the Kallianos deposit is abundant in volatile-bearing minerals, such as phyllosilicates and carbonates. These volatiles are a necessary component of the ore generation and mobilization process during the devolatilization of a carbonated greenschist facies rock. Supposing, however, that a magmatic source is in fact necessary - given that most deposits in the CMD have compelling links to late

Miocene plutonism - the structural data and geochronology favour a relatively older intrusion within the northern Cyclades as the more probable fluid source, such as the 19-14 Ma Tinos granodiorite.

Orogenic gold deposits and intrusion-related gold deposits (IRGD) exhibit numerous similarities, and distinguishing the two deposit types can be challenging (Goldfarb and Pitcairn, 2023; Groves et al., 1998; Sillitoe and Thompson, 1998). Intrusion-related gold has been documented in diverse tectonic settings, including active subduction zones and post-orogenic extensional environments, typically forming at shallow depths of 3-4 km (Sillitoe, 1991; Sillitoe and Thompson, 1998; Hart, 2007). Orogenic deposits can form at depths of up to 20 km and may likewise be syn- or post-orogenic (Groves et al., 1998). Although there are subtle differences in fluid compositions between the two deposit types - orogenic gold deposits typically possess low-salinity, CO_2-rich fluids, whereas IRGD are associated with saline fluids and variable CO_2 content (Phillips and Powell, 2010; Sillitoe and Thompson, 1998; Tomkins, 2013) - these criteria are rarely conclusive. Furthermore, neither orogenic gold deposits nor IRGDs produce alteration zones of any significant size, and alteration associated with either deposit is controlled by sheeted veins associated with low-grade mineralization. Both deposit types can also transport gold as reduced sulfur complexes (Sillitoe, 1991; Sillitoe and Thompson, 1998; Hart, 2007). Due to these similarities, it is difficult to assess to which of the classifications the Kallianos deposit belongs using paragenesis or geochemistry alone. The deposit's key characteristics (ore controlled by sheeted quartz veins featuring gold, tellurides, pyrite, and other sulfides) are shared by both orogenic gold deposits and IRGDs. However, we have demonstrated here that ore-controlling structures were most likely generated while the host rocks to the deposit transited the brittle-ductile transition zone (250-300°C), coinciding with their exhumation below a major post-orogenic

detachment. Whereas the implied back-arc setting makes a typical orogenic gold deposit unlikely (Jolivet et al., 2010), a typical back-arc geotherm of ~30°C/km would position the brittle-ductile transition zone at a depth of ~10 km, suggesting that the ore-controlling structures at Kallianos formed too deep to represent a typical IRGD. Because the existing geochemical data are unable to conclusively distinguish the two deposit types, the structural observations here strongly suggest that the Kallianos deposit likely represents an orogenic-style gold deposit formed during post-orogenic tectonics, for which several recent examples have been described (e.g., Lawley et al., 2023).

Recent studies outside the Cyclades challenge the traditional subduction metamorphic devolatilization models of orogenic gold deposits. Other examples include the Phanerozoic hypozonal deposit at Danba in China, as well as the Archean Kanowna Belle orogenic gold deposit in Western Australia, where these deposits dispute the classic model due to complex, multistage histories, and where gold mineralization events are thought to have occurred both before and after peak metamorphism (Sugiono et al., 2021; Wang et al., 2022). In Canada, deposits like the Malartic-Val-d'Or Camp (MVC) and the MacLellan gold deposit are also less consistent with the traditional model (Herzog et al., 2023; Lawley et al., 2015, 2023). These deposits show a complex history involving multiple hydrothermal and (pre- to post-) deformation stages, inconsistent with the model of a single metallogenic event. The MVC yields gold deposition ages that post-date peak metamorphism by tens to hundreds of millions of year. The MacLellan deposit's gold deposition appears linked to the exhumation of chemically reactive trap rocks, where far-field tectonics are interpreted as the drivers of post-orogenic auriferous fluids. These deposits are just a couple of examples of that invoke fluid sources and transport mechanisms beyond the simple metamorphic devolatilization model and can often connect temporal and spatial evolution of orogenic gold

mineralization to episodes of extension and exhumation. Herein, the new observations align with modern models, which propose the remobilization or formation of new gold in a post-peak metamorphism setting, often linked to far-field tectonic events (Henley et al., 1976; Lawley et al., 2020, 2023; Molnár et al., 2018; Stüwe et al., 1993).

Summary

The data presented in this study provide new, valuable insights into the timing, nature of fluids, and deformation style within the Kallianos Au-Ag-Te deposit. The structural analysis of veins highlights distinct deformation mechanisms and fluid interaction, with V_1 occurring during early, layer-parallel deformation during peak metamorphism, and V_2 and V_3 reflecting later stages of fluid infiltration and deformation in a brittle-ductile environment (Figure 13). Top-to-NE shear bands, accompanied by NW-SE to NNW-SSE strike-slip shear, show en-echelon veins (V_2) which are likely the result of coaxial strain components recorded during mineral deposition due to the NE-SW extension of the NCDS (Figure 13). Mica $^{40}Ar/^{39}Ar$ and $^{87}Rb/^{87}Sr$ geochronology indicates that greenschist facies deformation of the host rock occurred between c. 20-31 Ma, with fluid flow occurring between c. 21-26 Ma. The ZHe suggests cooling of the host rock to below ~200°C occurred between c. 14-11 Ma, aligning with the onset of brittle deformation related to progressive extension. By examining Cenozoic deposits that have not witnessed subsequent tectonism, we were able to obtain high-precision geochronology to better quantify the timing and rates of mineralization before any significant overprinting has occurred. Although the C-O isotope data exhibit significant wall rock-fluid interaction, the precise source of the fluids remains uncertain. Importantly, the lack of major alteration halos or skarn-like features and the absence of nearby magmatic activity in the deposit area, suggest that the dominate fluids were not likely derived from

typical magmatic sources. Overall, these results contribute to a better understanding of the tectonic and fluid history of the region, offering new insights into the interplay between metamorphism, fluid migration, and exhumation in a complex tectonic setting. A thorough geochemial comparison of the deposit with the nearby plutons, such as Tinos, Oxylithos, and Skiros, would help evaluate possible genetic links to the Kallianos Au-Ag-Te deposit. Further detailed mapping of the area to uncover the existence of a dextral conjugate vein set such as that observed on Mykonos would be valuable to strengthen the coaxial strain model. Comprehensive investigations of the structural architecture of younger Cenozoic orogenic deposits like the one on Evia, where mineralizing structures sustained minimal subsequent deformation, will clarify the original structural controls of older polydeformed systems such as many Precambrian orogenic gold deposits.

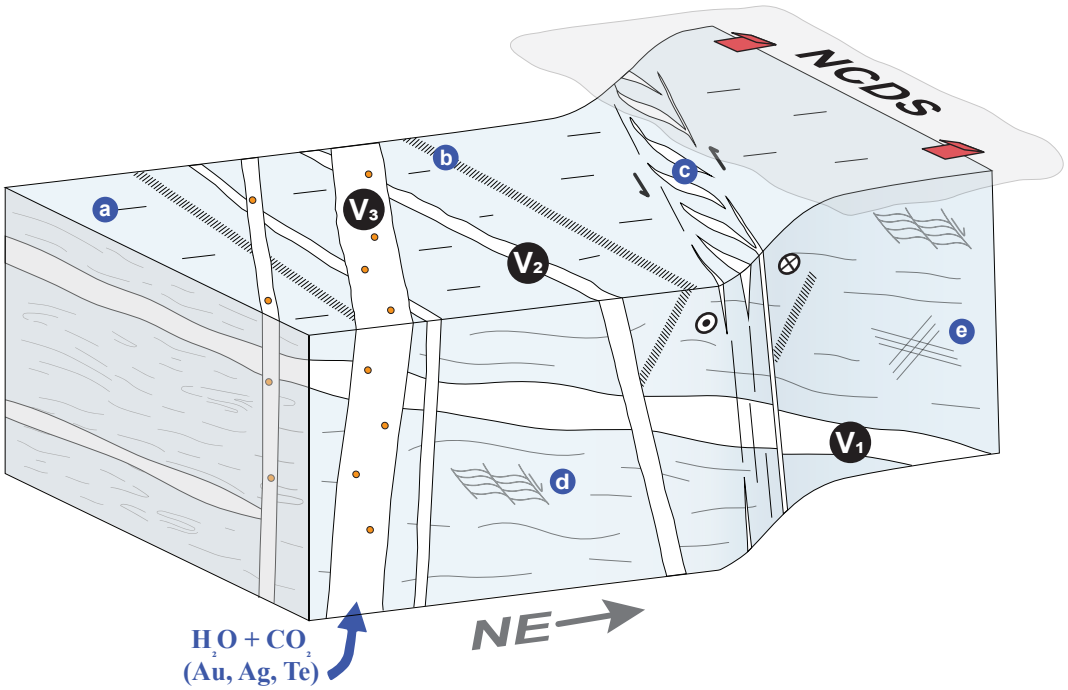

Figure 13. Synoptic diagram summarizing key structural features of the Kallianos Au-Ag-Te deposit on southeastern Evia, Greece. The host rock is undifferentiated CBU in the footwall of the North Cycladic Detachment System (NCDS). Schematic representation of qz ± cal veins cross-cutting relationships between V_1 (carbonate replacement veins) with V_2 and V_3 (e.g., Agia Barbara) with relative mineralization content (orange circles). Additional structures show a) stretching lineations orthogonal to the veins; b) kink bands; c) sinistral en-echelon veins; d) brittle-ductile top-to-NE shear bands in the host rock; and e) joints.

References

Alexouli-Livaditi, K., 1978. Mixed sulphide ores of Kallianou area, southern Evia. PhD thesis, National Technical University of Athens (in Greek).

Avigad, D., Garfunkel, Z., Jolivet, L., Azañón, J.M., 1997. Back arc extension and denudation of Mediterranean eclogites. Tectonics 16, 924-941. https://doi.org/10.1029/97TC02003

Baker, J., Matthews, A., 1995. The stable isotopic evolution of a metamorphic complex, Naxos, Greece. Contributions to Mineralogy and Petrology 120, 391-403. https://doi.org/10.1007/BF00306516

Bakowsky, C., Schneider, D.A., Grasemann, B., Soukis, K., 2023. Miocene ductile thinning below the Folegandros Detachment System, Cyclades, Greece. Terra Nova 35, 220-229. https://doi.org/10.1111/ter.12646

Barnes, C., Schneider, D.A., Majka, J., Camacho, A., Bukała, M., Włodek, A., 2023. $^{40}Ar/^{39}Ar$ dates controlled by white mica deformation and strain localization: Insights from comparing in situ laser ablation and single-grain fusion techniques. Journal of Metamorphic Geology 41(9), 1142-1166. https://doi.org/10.1111/jmg.12739

Barnes, C., Zack, T., Bukała, M., Rösel, D., Mark, C., Schneider, D.A., 2024. Dating metamorphic processes and identifying $^{87}Sr/^{86}Sr$ inheritance using volume-coupled Rb/Sr geochronology and geochemistry of in situ white mica: A demonstration with HP/LT rocks from Syros, Greece. Chemical Geology 660, 122149. https://doi.org/10.1016/j.chemgeo.2024.122149

Baziotis, I., Mposkos, E., Windley, B.F., Lamont, T.N., 2020. Exhumation of Attica high-pressure rocks in a subduction channel: New metamorphic PT constraints from Attica, NW Cyclades, Greece. Lithos 354-355, 105266. https://doi.org/10.1016/j.lithos.2019.105266

Berger, A., Schneider, D.A., Grasemann, B., Stockli, D., 2013. Footwall mineralization during Late Miocene extension along the West Cycladic Detachment System, Lavrion, Greece. Terra Nova 25, 181-191. https://doi.org/10.1111/ter.12016

Best, M.G., Christiansen, E.H., Deino, A.L., Grommé, C.S., Tingey, D.G., 1995. Correlation and emplacement of a large, zoned, discontinuously exposed ash flow sheet: The $^{40}Ar/^{39}Ar$ chronology, paleomagnetism, and petrology of the Pahranagat Formation, Nevada. Journal of Geophysical Research: Solid Earth 100, 24593-24609. https://doi.org/10.1029/95JB01690

Bickford, M.E., Mock, T.D., Steinhart III, W.E., Collerson, K.D., Lewry, J.F., 2005. Origin of the Archean Sask craton and its extent within the Trans-Hudson orogen: evidence from Pb and Nd isotopic compositions of basement rocks and post-orogenic intrusions. Canadian Journal of Earth Sciences 42, 659-684. https://doi.org/10.1139/e04-064

Bonneau, M., 1984. Correlation of the Hellenide nappes in the south-east Aegean and their tectonic reconstruction. Geological Society, London, Special Publications 17, 517-527. https://doi.org/10.1144/GSL.SP.1984.017.01.38

Bonneau, M., 1982. Evolution geodynamique de l'arc egeen depuis le Jurassique superieur jusqu'au Miocene. Bulletin de la Société Géologique de France S7-XXIV, 229-242. https://doi.org/10.2113/gssgfbull.S7-XXIV.2.229

Bonsall, T.A., Spry, P., Voudouris, P., KSt, S., Tombros, S., Melfos, V., 2011. The Geochemistry of carbonate-replacement Pb-Zn-Ag mineralization in the Lavrion District, Attica, Greece: Fluid inclusion, stable isotope, and rare earth element studies. Economic Geology 106, 619-651. https://doi.org/10.2113/econgeo.106.4.619

Bowman, J. R. 1998. Stable-isotope systematics of skarn, in: Lentz, D.R. (Ed.), Mineralized Intrusion-Related Skarn Systems. Mineralogical Association of Canada. Short Course, Ottawa 26, pp. 99-145.

Bradley, K.E., Vassilakis, E., Hosa, A., Weiss, B.P., 2013. Segmentation of the Hellenides recorded by Pliocene initiation of clockwise block rotation in Central Greece. Earth and Planetary Science Letters 362, 6-19. https://doi.org/10.1016/j.epsl.2012.11.043

Brichau, S., Ring, U., Ketcham, R., Carter, A., Stockli, D., Brunel, M., 2006. Constraining the long-term evolution of the slip rate for a major extensional fault system in the central Aegean, Greece, using thermochronology. Earth and Planetary Science Letters 241, 293-306. https://doi:10.1016/j.epsl.2005.09.065

Brichau, S., Ring, U., Carter, A., Monié, P., Bolhar, R., Stockli, D., Brunel, M., 2007. Extensional faulting on Tinos Island, Aegean Sea, Greece: How many detachments? Tectonics 26. https://doi.org/10.1029/2006TC001969

Bröcker, M., Bieling, D., Hacker, B., Gans, P., 2004. High-Si phengite records the time of greenschist facies overprinting: implications for models suggesting mega-detachments in the Aegean Sea. Journal of Metamorphic Geology 22, 427-442. https://doi.org/10.1111/j.1525-1314.2004.00524.x

Camacho, A., Lee, J., Fitz Gerald, J. D., Zhao, J., Abdu, Y., Jenkins, D., Hawthorne, F., Creaser, R., Armstrong, R., 2012. Planar defects as Ar traps in trioctahedral micas: A mechanism for increased Ar retentivity in phlogopite. Earth and Planetary Science Letters 341, 255-267. https://doi.org/10.1016/j.epsl.2012.05.041

Coleman, M., Schneider, D.A., Grasemann, B., Soukis, K., Lozios, S., Hollinetz, M., 2020. Lateral Termination of a Cycladic-Style Detachment System (Hymittos, Greece). Tectonics 39, e2020TC006128. https://doi.org/10.1029/2020TC006128

Coplen, T.B., Holden, N.E., Ding, T., Meijer, H.A.J., Vogl, J., Zhu, X., 2022. The table of standard atomic weights—an exercise in consensus. Rapid Communications in Mass Spectrometry 36, e8864. https://doi.org/10.1002/rcm.8864

Cossette, E., Schneider, D.A., Warren, C., Grasemann, B., 2015. Lithological, rheological, and fluid infiltration control on $^{40}Ar/^{39}Ar$ ages in polydeformed rocks from the West Cycladic detachment system, Greece. Lithosphere 7, 189-205. https://doi.org/10.1130/L416.1

Dazé, A., Lee, J.K.W., Villeneuve, M., 2003. An intercalibration study of the Fish Canyon sanidine and biotite $^{40}Ar/^{39}Ar$ standards and some comments on the age of the Fish Canyon Tuff. Chemical Geology 199, 111-127. https://doi.org/10.1016/S0009-2541(03)00079-2

Denèle, Y., Lecomte, E., Jolivet, L., Lacombe, O., Labrousse, L., Huet, B., Le Pourhiet, L., 2011. Granite intrusion in a metamorphic core complex: The example of the Mykonos laccolith (Cyclades, Greece). Tectonophysics 501, 52-70. https://doi.org/10.1016/j.tecto.2011.01.013

Doutsos, T., Pe-Piper, G., Boronkay, K., Koukouvelas, I., 1993. Kinematics of the central Hellenides. Tectonics 12, 936-953. https://doi.org/10.1029/93TC00108

Ducharme, T.A., Schneider, D.A., Grasemann, B., Bukała, M., Camacho, A., Larson, K., Soukis, K., 2024. Syn-exhumation metasomatic glaucophane-phengite-quartz veins formed at moderate pressures: exploring the control of fO_2 and bulk composition on nominally HP metamorphic assemblages. Contributions to Mineralogy and Petrology 179. https://doi.org/10.1007/s00410-024-02101-8

Ducharme, T.A., Schneider, D.A., Grasemann, B., Klonowska, I., 2022. Stretched Thin: Oligocene Extrusion and Ductile Thinning of the Basal Unit Along the Evia Shear Zone, NW Cyclades, Greece. Tectonics 41, e2022TC007561. https://doi.org/10.1029/2022TC007561

Ducharme, T.A., Schneider, D.A., Grasemann, B., Scoging, V., Bakowsky, C., Larson, K.P., Camacho, A., 2024. Strain Partitioning in a Flattening Shear Zone: Re-Evaluation of a Cycladic Style Detachment. Tectonics 43, e2024TC008412. https://doi.org/10.1029/2024TC008412

Ducoux, M., Branquet, Y., Jolivet, L., Arbaret, L., Grasemann, B., Rabillard, A., Gumiaux, C., Drufin, S., 2017. Synkinematic skarns and fluid drainage along detachments: The West Cycladic Detachment System on Serifos Island (Cyclades, Greece) and its related mineralization. Tectonophysics 695, 1-26. https://doi.org/10.1016/j.tecto.2016.12.008

Dunlap, W.J., Teyssier, C., McDougall, I., Baldwin, S., 1991. Ages of deformation from K/Ar and $^{40}Ar/^{39}Ar$ dating of white micas. Geology 19, 1213-1216. https://doi.org/10.1130/0091-7613(1991)019<1213:AODFKA>2.3.CO;2

Dürr, S., Altherr, R., Keller, J., Okrusch, M., and Seidel, E., 1978. The median Aegean crystalline belt: Stratigraphy, structure, metamorphism, magmatism, in Cloos , H., Roeder, D., and Schmidt, K. (Eds.), Alps, Apennines, Hellenides, v. 38: Stuttgart, Schweizerbart, pp. 455-476

Ferrill, D.A., Morris, A.P., Evans, M.A., Burkhard, M., Groshong, R.H., Onasch, C.M., 2004. Calcite twin morphology: a low-temperature deformation geothermometer. Journal of Structural Geology 26, 1521–1529. https://doi.org/10.1016/j.jsg.2003.11.028

Flansburg, M.E., Stockli, D.F., Poulaki, E.M., Soukis, K., 2019. Tectono-magmatic and Stratigraphic Evolution of the Cycladic Basement, Ios Island, Greece. Tectonics 38, 2291-2316. https://doi.org/10.1029/2018TC005436

Freeman, S.R., Inger, S., Butler, R.W.H., Cliff, R.A., 1997. Dating deformation using Rb-Sr in white mica: Greenschist facies deformation ages from the Entrelor shear zone, Italian Alps. Tectonics 16, 57-76. https://doi.org/10.1029/96TC02477

Ganor, J., Matthews, A., Schliestedt, M., 1994. Post-metamorphic low delta ^{13}C calcite in the Cycladic Complex (Greece) and their implications for modeling fluid infiltration processes using carbon isotope compositions. European Journal of Mineralogy 6, 365-379.

Ganor, J., Matthews, A., Schliestedt, M., Garfunkel, Z., 1996. Oxygen isotopic heterogeneities of metamorphic rocks; an original tectonostratigraphic signature, or an imprint of exotic fluids? A case study of Sifnos and Tinos islands (Greece). European Journal of Mineralogy 8, 719-732.

Gautier, P., Brun, J.-P., 1994. Crustal-scale geometry and kinematics of late-orogenic extension in the central Aegean (Cyclades and Ewia Island). Tectonophysics 238, 399-424. https://doi.org/10.1016/0040-1951(94)90066-3

Gautier, P., Brun, J.-P., Jolivet, L., 1993. Structure and kinematics of Upper Cenozoic extensional detachment on Naxos and Paros (Cyclades Islands, Greece). Tectonics 12, 1180-1194. https://doi.org/10.1029/93TC01131

Goldfarb, R.J., Groves, D.I., 2015. Orogenic gold: Common or evolving fluid and metal sources through time. Lithos 233, 2-26. https://doi.org/10.1016/j.lithos.2015.07.011

Goldfarb, R.J., Groves, D.I., Gardoll, S., 2001. Orogenic gold and geologic time: a global synthesis. Ore Geology Reviews 18, 1-75. https://doi.org/10.1016/S0169-1368(01)00016-6

Goldfarb, R.J., Pitcairn, I., 2023. Orogenic gold: is a genetic association with magmatism realistic? Mineralium Deposita 58, 5-35. https://doi.org/10.1007/s00126-022-01146-8

Grasemann, B., Huet, B., Schneider, D.A., Rice, A., Lemonnier, N., Tschegg, C., 2017. Miocene postorogenic extension of the Eocene synorogenic imbricated Hellenic subduction channel: New constraints from Milos (Cyclades, Greece). GSA Bulletin 130, 238-262. https://doi.org/10.1130/B31731.1

Grasemann, B., Schneider, D.A., Stöckli, D.F., Iglseder, C., 2012. Miocene bivergent crustal extension in the Aegean: Evidence from the western Cyclades (Greece). Lithosphere 4, 23-39. https://doi.org/10.1130/L164.1

Groves, D.I., Goldfarb, R.J., Gebre-Mariam, M., Hagemann, S.G., Robert, F., 1998. Orogenic gold deposits: A proposed classification in the context of their crustal distribution and relationship to other gold deposit types. Ore Geology Reviews 13, 7-27. https://doi.org/10.1016/S0169-1368(97)00012-7

Groves, D.I., Santosh, M., Deng, J., Wang, Q., Yang, L., Zhang, L., 2020. A holistic model for the origin of orogenic gold deposits and its implications for exploration. Mineralium Deposita 55, 275-292. https://doi.org/10.1007/s00126-019-00877-5

Gyomlai, T., Agard, P., Herviou, C., Jolivet, L., Monié, P., Mendes, K., Iemmolo, A., 2023. In situ Rb-Sr and ^{40}Ar-^{39}Ar dating of distinct mica generations in the exhumed subduction complex of the Western Alps. Contributions to Mineralogy and Petrology 178. https://doi.org/10.1007/s00410-023-02042-8

Hart, C., 2007. Reduced Intrusion-related Gold Systems, in: Mineral Deposits of Canada: A Synthesis of Major Deposit-Types, District Metallogeny, the Evolution of Geological Provinces, and Exploration Methods. (Eds.) Special Publication 5. Geological Association of Canada, Mineral Deposits Division, pp. 95-112.

Henjes-Kunst, F., Kreuzer, H., 1982. Isotopic dating of pre-Alpidic rocks from the island of Ios (Cyclades, Greece). Contributions to Mineralogy and Petrology 80, 245-253. https://doi.org/10.1007/BF00371354

Henley, R.W., Norris, R.J., Paterson, C.J., 1976. Multistage ore genesis in the New Zealand geosyncline a history of post-metamorphic lode emplacement. Mineralium Deposita 11, 180-196. https://doi.org/10.1007/BF00204480

Herzog, M., LaFlamme, C., Beaudoin, G., Marsh, J., Guilmette, C., 2023. U-Pb vein xenotime geochronology constraints on timing and longevity of orogenic gold mineralization in the Malartic-Val-d'Or Camp, Abitibi Subprovince, Canada. Mineralium Deposita 58, 105-133. https://doi.org/10.1007/s00126-022-01131-1

Hogmalm, K.J., Zack, T., Karlsson, A.K.-O., Sjöqvist, A.S.L., Garbe-Schönberg, D., 2017. In situ Rb-Sr and K-Ca dating by LA-ICP-MS/MS: an evaluation of N_2O and SF_6 as reaction gases. Journal of Analytical Atomic Spectroscopy 32, 305-313. https://doi.org/10.1039/C6JA00362A

Huet, B., Labrousse, L., Monié, P., Malvoisin, B., Jolivet, L., 2015. Coupled phengite ^{40}Ar-^{39}Ar geochronology and thermobarometry: P-T-t evolution of Andros Island (Cyclades, Greece). Geological Magazine 152, 711-727. https://doi.org/10.1017/S0016756814000661

Iglseder, C., Grasemann, B., Schneider, D.A., Petrakakis, K., Miller, C., Klötzli, U.S., Thöni, M., Zámolyi, A., Rambousek, C., 2009. I and S-type plutonism on Serifos (W-Cyclades, Greece). Tectonophysics 473, 69-83. https://doi.org/10.1016/j.tecto.2008.09.021

Jacobshagen, V., 1986. Geologie von Griechland. Borntraeger, Stuttgart, Germany, pp. 279.

Jolivet, L., Brun, J.-P., 2010. Cenozoic Geodynamic Evolution of the Aegean. International Journal of Earth Sciences 99, 109-138. https://doi.org/10.1007/s00531-008-0366-4

Jolivet, L., Faccenna, C., 2000. Mediterranean extension and the Africa-Eurasia collision. Tectonics 19, 1095-1106. https://doi.org/10.1029/2000TC900018

Jolivet, L., Famin, V., Mehl, C., Parra, T., Aubourg, C., Hébert, R., Philippot, P., 2004. Strain localization during crustal-scale boudinage to form extensional metamorphic domes in the

Aegean Sea, in: Whitney, D.L., Teyssier, C., Siddoway, C.S. (Eds.), Gneiss Domes in Orogeny. Geological Society of America, 185-210. https://doi.org/10.1130/0-8137-2380-9.185

Jolivet, L., Lecomte, E., Huet, B., Denèle, Y., Lacombe, O., Labrousse, L., Le Pourhiet, L., Mehl, C., 2010. The North Cycladic Detachment System. Earth and Planetary Science Letters 289, 87-104. https://doi.org/10.1016/j.epsl.2009.10.032

Jolivet, L., Patriat, M., 1999. Ductile extension and the formation of the Aegean Sea. Geological Society, London, Special Publications 156, 427-456. https://doi.org/10.1144/GSL.SP.1999.156.01.20

Katsikatsos, G., 1978. The mineral wealth of the area of the Euboea prefecture. Athens: Institute of Geological and Mining Research International Report 7, 29.

Katzir, Y., Avigad, D., Matthews, A., Garfunkel, Z., Evans, B.W., 2000. Origin, HP/LT metamorphism and cooling of ophiolitic mélanges in southern Evia (NW Cyclades), Greece. Journal of Metamorphic Geology 18, 699-718. https://doi.org/10.1046/j.1525-1314.2000.00281.x

Keller, D.R., 1984. Archampolis: An early Iron Age Settlement And Sanctuary in Southern Euboea. American Journal of Archaeology 88, 249.

Kuiper, K.F., Deino, A., Hilgen, F.J., Krijgsman, W., Renne, P.R., Wijbrans, J.R., 2008. Synchronizing Rock Clocks of Earth History. Science 320, 500-504. https://doi.org/10.1126/science.1154339

Lagos, M., Scherer, E.E., Tomaschek, F., Münker, C., Keiter, M., Berndt, J., Ballhaus, C., 2007. High precision Lu-Hf geochronology of Eocene eclogite-facies rocks from Syros, Cyclades, Greece. Chemical Geology 243, 16-35. https://doi.org/10.1016/j.chemgeo.2007.04.008

Lanari, P., Vho, A., Bovay, T., Airaghi, L., Centrella, S., 2019. Quantitative compositional mapping of mineral phases by electron probe micro-analyser. Geological Society, London, Special Publications 478, 39-63. https://doi.org/10.1144/SP478.4

Lanari, P., Vidal, O., De Andrade, V., Dubacq, B., Lewin, E., Grosch, E.G., Schwartz, S., 2014. XMapTools: A MATLAB©-based program for electron microprobe X-ray image processing and geothermobarometry. Computers & Geosciences 62, 227-240. https://doi.org/10.1016/j.cageo.2013.08.010

Larson, K.P., Button, M., Shrestha, S., Camacho, A., 2023. A comparison of $^{87}Rb/^{87}Sr$ and $^{40}Ar/^{39}Ar$ dates: Evaluating the problem of excess ^{40}Ar in Himalayan mica. Earth and Planetary Science Letters 609, 118058. https://doi.org/10.1016/j.epsl.2023.118058

Latsoudas, CH., Triantaphyllis, M., 1997. Geological map of Greece, Karistos-Platanistos sheet, scale 1:50,000. Institute of Geology and Mineral Exploration.

Laurent, V., Beaudoin, A., Jolivet, L., Arbaret, L., Augier, R., Rabillard, A., Menant, A., 2015. Interrelations between extensional shear zones and synkinematic intrusions: The example of Ikaria Island (NE Cyclades, Greece). Tectonophysics 651-652, 152-171. https://doi.org/10.1016/j.tecto.2015.03.020

Laurent, V., Scaillet, S., Jolivet, L., Augier, R., Roche, V., 2021. ^{40}Ar behaviour and exhumation dynamics in a subduction channel from multi-scale $^{40}Ar/^{39}Ar$ systematics in phengite. Geochimica et Cosmochimica Acta 311, 141-173. https://doi.org/10.1016/j.gca.2021.06.001

Lawley, C.J.M., Dubé, B., Mercier-Langevin, P., Kjarsgaard, B., Knight, R., Vaillancourt, D., 2015. Defining and mapping hydrothermal footprints at the BIF-hosted Meliadine gold district, Nunavut, Canada. Journal of Geochemical Exploration 155, 33-55. https://doi.org/10.1016/j.gexplo.2015.04.001

Lawley, C.J.M., Schneider, D.A., Camacho, A., McFarlane, C.R.M., Davis, W.J., Yang, X.-M., 2023. Post-orogenic exhumation triggers gold mineralization in the Trans-Hudson orogen: New geochronology results from the Lynn Lake greenstone belt, Manitoba, Canada. Precambrian Research 395, 107127. https://doi.org/10.1016/j.precamres.2023.107127

Lawley, C.J.M., Yang, X.M., Selby, D., Davis, W., Zhang, S., Petts, D.C., Jackson, S.E., 2020. Sedimentary basin controls on orogenic gold deposits: New constraints from U-Pb detrital zircon and Re-Os sulphide geochronology, Lynn Lake greenstone belt, Canada. Ore Geology Reviews 126, 103790. https://doi.org/10.1016/j.oregeorev.2020.103790

Lister, G.S., Banga, G., Feenstra, A., 1984. Metamorphic core complexes of Cordilleran type in the Cyclades, Aegean Sea, Greece. Geology 12, 221-225. https://doi.org/10.1130/0091-7613(1984)12<221:MCCOCT>2.0.CO;2

Maluski, H., Bonneau, M., Kienast, J.R., 1987. Dating the metamorphic events in the Cycladic area; $^{39}Ar/^{40}$ Ar data from metamorphic rocks of the Island of Syros (Greece). Bulletin de la Société Géologique de France III, 833-842. https://doi.org/10.2113/gssgfbull.III.5.833

Matthews, A., L., L., Avigad, D., Garfunkel, Z., 1999. Fluid-rock interaction and thermal evolution during thrusting of an Alpine metamorphic complex (Tinos island, Greece). Contributions to Mineralogy and Petrology 135, 212-224. https://doi.org/10.1007/s004100050507

Mehl, C., Jolivet, L., Lacombe, O., 2005. From ductile to brittle: Evolution and localization of deformation below a crustal detachment (Tinos, Cyclades, Greece). Tectonics 24, TC4017. https://doi.org/10.1029/2004TC001767

Menant, A., Jolivet, L., Augier, R., Skarpelis, N., 2013. The North Cycladic Detachment System and associated mineralization, Mykonos, Greece: Insights on the evolution of the Aegean domain. Tectonics 32, 433-452. https://doi.org/10.1002/tect.20037

Molnár, F., Middleton, A., Stein, H., O`Brien, H., Lahaye, Y., Huhma, H., Pakkanen, L., Johanson, B., 2018. Repeated syn- and post-orogenic gold mineralization events between 1.92 and 1.76 Ga along the Kiistala Shear Zone in the Central Lapland Greenstone Belt, northern Finland. Ore Geology Reviews 101, 936-959. https://doi.org/10.1016/j.oregeorev.2018.08.015

Muñoz-Montecinos, J., Giuliani, A., Oesch, S., Volante, S., Peters, B., Behr, W., 2024. In situ rubidium-strontium geochronology of white mica in young metamafic and metasomatic rocks from Syros: testing the limits of laser-ablation triple-quadrupole inductively coupled plasma mass spectrometer mica dating using different anchoring approaches. Geochronology 6, 585-605. https://doi.org/10.5194/gchron-6-585-2024

Nüchter, J.-A., Stöckhert, B., 2007. Vein quartz microfabrics indicating progressive evolution of fractures into cavities during postseismic creep in the middle crust. Journal of Structural Geology 29, 1445-1462. https://doi.org/10.1016/j.jsg.2007.07.011

Oriolo, S., Gómez, A.L.R., Maffini, M.N., Oyhantçabal, P., Demarco, M.M., Vargas Perucca, M.S., Bastías Torres, M.V., Rubinstein, N.A., 2024. Transtension, brittle-ductile shear zones and hydrothermal ore deposits: Towards quantitative structural and kinematic models. Journal of Structural Geology 185, 105173. https://doi.org/10.1016/j.jsg.2024.105173

Pe-Piper, G., Piper, D.J.W., 1994. Miocene magnesian andesites and dacites, Evia, Greece: adakites associated with subducting slab detachment and extension. Lithos 31, 125-140. https://doi.org/10.1016/0024-4937(94)90004-3

Pettke, T., Diamond, L.W., Villa, I.M., 1999. Mesothermal gold veins and metamorphic devolatilization in the northwestern Alps: The temporal link. Geology 27, 641-644. https://doi.org/10.1130/0091-7613(1999)027<0641:MGVAMD>2.3.CO;2

Phillips, G.N., Powell, R., 2010. Formation of gold deposits: a metamorphic devolatilization model. Journal of Metamorphic Geology 28, 689-718. https://doi.org/10.1111/j.1525-1314.2010.00887.x

Phillips, G.N., Powell, R., 1993. Link between gold provinces. Economic Geology 88, 1084-1098. https://doi.org/10.2113/gsecongeo.88.5.1084

Poulaki, E.M., Stockli, D.F., Flansburg, M.E., Soukis, K., 2019. Zircon U-Pb Chronostratigraphy and Provenance of the Cycladic Blueschist Unit and the Nature of the Contact With the Cycladic Basement on Sikinos and Ios Islands, Greece. Tectonics 38, 3586-3613. https://doi.org/10.1029/2018TC005403

Powell, R., Will, T.M., Phillips, G.N., 1991. Metamorphism in Archaean greenstone belts: calculated fluid compositions and implications for gold mineralization. Journal of Metamorphic Geology 9, 141-150. https://doi.org/10.1111/j.1525-1314.1991.tb00510.x

Putlitz, B., Cosca, M.A., Schumacher, J.C., 2005. Prograde mica $^{40}Ar/^{39}Ar$ growth ages recorded in high pressure rocks (Syros, Cyclades, Greece). Chemical Geology 214, 79-98. https://doi.org/10.1016/j.chemgeo.2004.08.056

Reiners, P.W., Spell, T.L., Nicolescu, S., Zanetti, K.A., 2004. Zircon (U-Th)/He thermochronometry: He diffusion and comparisons with $^{40}Ar/^{39}Ar$ dating. Geochimica et Cosmochimica Acta 68, 1857-1887. https://doi.org/10.1016/j.gca.2003.10.021

Renne, P.R., Norman, E.B., 2001. Determination of the half-life of ^{37}Ar by mass spectrometry. Physical Review C 63, 047302. https://doi.org/10.1103/PhysRevC.63.047302

Renne, P.R., Swisher, C.C., Deino, A.L., Karner, D.B., Owens, T.L., DePaolo, D.J., 1998. Intercalibration of standards, absolute ages and uncertainties in $^{40}Ar/^{39}Ar$ dating. Chemical Geology 145, 117-152. https://doi.org/10.1016/S0009-2541(97)00159-9

Rice, A.H.N., Grasemann, B., 2016. Field Guide to the West Cycladic Detachment System on Kythnos, Greece. The Journal of the Virtual Explorer 50.

Ring, U., Glodny, J., Will, T., Thomson, S., 2010. The Hellenic Subduction System: High-Pressure Metamorphism, Exhumation, Normal Faulting, and Large-Scale Extension.

Annual Review of Earth and Planetary Sciences 38, 45-76. https://doi.org/10.1146/annurev.earth.050708.170910

Ring, U., Glodny, J., Will, T., Thomson, S., 2007. An Oligocene extrusion wedge of blueschist-facies nappes on Evia, Aegean Sea, Greece: Implications for the early exhumation of high-pressure rocks. Journal of the Geological Society 164, 637-652. https://doi.org/10.1144/0016-76492006-041

Ring, U., Layer, P.W., 2003. High-pressure metamorphism in the Aegean, eastern Mediterranean: Underplating and exhumation from the Late Cretaceous until the Miocene to Recent above the retreating Hellenic subduction zone. Tectonics 22. https://doi.org/10.1029/2001TC001350

Roddick, J.C., 1983. High precision intercalibration of ^{40}Ar-^{39}Ar standards. Geochimica et Cosmochimica Acta 47, 887-898. https://doi.org/10.1016/0016-7037(83)90154-0

Rösel, D., Zack, T., 2022. LA-ICP-MS/MS Single-Spot Rb-Sr Dating. Geostandards and Geoanalytical Research 46, 143-168. https://doi.org/10.1111/ggr.12414

Rosenbaum, G., Avigad, D., Sánchez-Gómez, M., 2002. Coaxial flattening at deep levels of orogenic belts: evidence from blueschists and eclogites on Syros and Sifnos (Cyclades, Greece). Journal of Structural Geology 24, 1451-1462. https://doi.org/10.1016/S0191-8141(01)00143-2

Scheffer, C., Tarantola, A., Vanderhaeghe, O., Voudouris, P., Rigaudier, T., Photiades, A., Morin, D., Alloucherie, A., 2017. The Lavrion Pb-Zn-Fe-Cu-Ag detachment-related district (Attica, Greece): Structural control on hydrothermal flow and element transfer-deposition. Tectonophysics 717, 607-627. https://doi.org/10.1016/j.tecto.2017.06.029

Schliestedt, M., Matthews, A., 1987. Transformation of blueschist to greenschist facies rocks as a consequence of fluid infiltration, Sifnos (Cyclades), Greece. Contributions to Mineralogy and Petrology 97, 237-250.

Schneider, D.A., Grasemann, B., Lion, A., Soukis, K., Draganits, E., 2018. Geodynamic significance of the Santorini Detachment System (Cyclades, Greece). Terra Nova 30, 414-422. https://doi.org/10.1111/ter.12357

Schneider, D.A., Heizler, M.T., Bickford, M.E., Wortman, G.L., Condie, K.C., Perilli, S., 2007. Timing constraints of orogeny to cratonization: Thermochronology of the Paleoproterozoic

Trans-Hudson orogen, Manitoba and Saskatchewan, Canada. Precambrian Research 153, 65-95. https://doi.org/10.1016/j.precamres.2006.11.007

Schneider, D.A., Senkowski, C., Vogel, H., Grasemann, B., Iglseder, Ch., Schmitt, A.K., 2011. Eocene tectonometamorphism on Serifos (western Cyclades) deduced from zircon depth-profiling geochronology and mica thermochronology. Lithos 125, 151-172. https://doi.org/10.1016/j.lithos.2011.02.005

Shaked, Y., Avigad, D., Garfunkel, Z., 2000. Alpine high-pressure metamorphism at the Almyropotamos window (southern Evia, Greece). Geological Magazine 137, 367-380. https://doi.org/10.1017/S001675680000426X

Shin, T.A., 2014. Tectonic evolution of Aegean metamorphic core complexes, Andros and Tinos Islands, Greece. PhD thesis, University of Texas at Austin.

Siebenaller, L., Boiron, M.-C., Vanderhaeghe, O., Hibsch, C., Jessell, M.W., Andre-Mayer, A.-S., France-Lanord, C., Photiades, A., 2013. Fluid record of rock exhumation across the brittle-ductile transition during formation of a Metamorphic Core Complex (Naxos Island, Cyclades, Greece). Journal of Metamorphic Geology 31, 313-338. https://doi.org/10.1111/jmg.12023

Sillitoe, R.H., 1991. Intrusion-related gold deposits, in: Gold Metallogeny and Exploration. Blackie and Son Ltd., Glasgow, pp. 165-209.

Sillitoe, R.H., Thomson, J.F.H., 1998. Intrusion-Related Vein Gold Deposits: Types, Tectono-Magmatic Settings and Difficulties of Distinction from Orogenic Gold Deposits. Resource Geology 48, 237-250. https://doi.org/10.1111/j.1751-3928.1998.tb00021.x

Skarpelis, N., 2002. Geodynamics and evolution of the Miocene mineralization in the Cycladic-Pelagonian belt, Hellenides. Bulletin of the Geological Society of Greece 34, 2191-2206. https://doi.org/10.12681/bgsg.16862

Skarpelis, N., Lüders, V., 2007. Fluid inclusions, REE and sulfur isotope geochemistry of the Lavrion carbonate hosted ore deposit, SE Attica, Greece. 8th Goldschmidt Conference Abstracts, 2007, A945.

Soukis, K., Stockli, D.F., 2013. Structural and thermochronometric evidence for multi-stage exhumation of southern Syros, Cycladic islands, Greece. Tectonophysics 595-596, 148-164. https://doi.org/10.1016/j.tecto.2012.05.017

Spell, T.L., McDougall, I., 2003. Characterization and calibration of $^{40}Ar/^{39}Ar$ dating standards. Chemical Geology 198, 189-211. https://doi.org/10.1016/S0009-2541(03)00005-6

Steiger, R.H., Jäger, E., 1977. Subcommission on geochronology: Convention on the use of decay constants in geo- and cosmochronology. Earth and Planetary Science Letters 36, 359-362. https://doi.org/10.1016/0012-821X(77)90060-7

Stüwe, K., 1998. Tectonic constraints on the timing relationships of metamorphism, fluid production and gold-bearing quartz vein emplacement. Ore Geology Reviews 13, 219-228. https://doi.org/10.1016/S0169-1368(97)00019-X

Stüwe, K., Will, T.M., Zhou, S., 1993. On the timing relationship between fluid production and metamorphism in metamorphic piles: Some implications for the origin of post-metamorphic gold mineralisation. Earth and Planetary Science Letters 114, 417-430. https://doi.org/10.1016/0012-821X(93)90073-I

Sugiono, D., Thébaud, N., LaFlamme, C., Fiorentini, M., Martin, L., Rogers, J., Lorusso, G., McFarlane, C., 2021. Integration of multiple sulfur isotopes with structural analysis unveils the evolution of ore fluids and source of sulfur at the Kanowna Belle Archean orogenic gold deposit, Yilgarn Craton, Western Australia. Mineralium Deposita 56, 1471-1490. https://doi.org/10.1007/s00126-020-01032-1

Tomaschek, F., Kennedy, A.K., Villa, I.M., Lagos, M., Ballhaus, C., 2003. Zircons from Syros, Cyclades, Greece—Recrystallization and Mobilization of Zircon During High-Pressure Metamorphism. Journal of Petrology 44, 1977-2002. https://doi.org/10.1093/petrology/egg067

Tombros, S. F., Kokkalas, S., St.Seymour, K., Voudouris, P., Williams-Jones, A., Zhai, D., Liu, J., Fitros, M., 2021. The Kallianos Au-Ag-Te mineralization, Evia Island, Greece: a detachment-related distal hydrothermal deposit of the Attico-Cycladic Metallogenetic Massif. Mineralium Deposita 56, 665-684. https://doi.org/10.1007/s00126-020-00989-3

Tombros, S. F., St. Seymour, K., Williams-Jones, A.E., Spry, P.G., 2007. The Genesis of Epithermal Au-Ag-Te Mineralization, Panormos Bay, Tinos Island, Cyclades, Greece. Economic Geology 102, 1269-1294. https://doi.org/10.2113/gsecongeo.102.7.1269

Tombros, S.F., St. Seymour, K., Williams-Jones, A.E., Zhai, D., Liu, J., 2015. Origin of a barite-sulfide ore deposit in the Mykonos intrusion, Cyclades: Trace element, isotopic, fluid

inclusion and raman spectroscopy evidence. Ore Geology Reviews 67, 139-157. https://doi.org/10.1016/j.oregeorev.2014.11.016

Tombros, S.F., St. Seymour, K., Williams-Jones, A.E., Spry, P.G., 2008. Later stages of evolution of an epithermal system: Au-Ag mineralizations at Apigania Bay, Tinos Island, Cyclades, Hellas, Greece. Mineralogy and Petrology 94, 175-194. https://doi.org/10.1007/s00710-008-0019-0

Tomkins, A.G., 2013. On the source of orogenic gold. Geology 41, 1255-1256. https://doi.org/10.1130/focus122013.1

Uunk, B., Brouwer, F., De Paz-Álvarez, M., Van Zuilen, K., Huybens, R., Veer, R., Wijbrans, J.R., 2022. Consistent detachment of supracrustal rocks from a fixed subduction depth in the Cyclades. Earth and Planetary Sciences Letters 584, 117479. https://doi.org/10.1016/j.epsl.2022.117479

Uunk, B., Brouwer, F., ter Voorde, M., Wijbrans, J., 2018. Understanding phengite argon closure using single grain fusion age distributions in the Cycladic Blueschist Unit on Syros, Greece. Earth and Planetary Science Letters 484, 192-203. https://doi.org/10.1016/j.epsl.2017.12.031

Vavelidis, M., Bassiakos, Y., Begeman, F., Patriarcheas, K., Pernickai, E., Schmitt-Strecker, S., Wagner, G., 1985. 1. Geologie und Erzvorkommen (auf Sifnos) 3.

Vavelidis, M., Michailidis, M., 1990. Composition in the Fe-Pb-Cu-(Ag Zn) hydrothermal quartz veins of Kallianou area, Southern Euboea. Bulletin of Geological Society of Greece 22, 87-96.

Vaxevanopoulos, M., Davis, G., Milot, J., Blichert-Toft, J., Malod-Dognin, C., Albarède, F., 2022. Narrowing provenance for ancient Greek silver coins using Ag isotopes and Sb contents of potential ores. Journal of Archaeological Science 145, 105645. https://doi.org/10.1016/j.jas.2022.105645

Vermeesch, P., 2018. IsoplotR: A free and open toolbox for geochronology. Geoscience Frontiers 9, 1479-1493. https://doi.org/10.1016/j.gsf.2018.04.001

Voudouris, P., Mavrogonatos, C., Spry, P.G., Baker, T., Melfos, V., Klemd, R., Haase, K., Repstock, A., Djiba, A., Bismayer, U., Tarantola, A., Scheffer, C., Moritz, R., Kouzmanov, K., Alfieris, D., Papavassiliou, K., Schaarschmidt, A., Galanopoulos, E., Galanos, E., Kołodziejczyk, J., Stergiou, C., Melfou, M., 2019. Porphyry and epithermal deposits in

Greece: An overview, new discoveries, and mineralogical constraints on their genesis. Ore Geology Reviews 107, 654-691. https://doi.org/10.1016/j.oregeorev.2019.03.019

Voudouris, P.C., Spry, P.G., Sakellaris, G.A., Mavrogonatos, C., 2011. A cervelleite-like mineral and other Ag-Cu-Te-S minerals [Ag_2CuTeS and $(Ag,Cu)_2TeS$] in gold-bearing veins in metamorphic rocks of the Cycladic Blueschist Unit, Kallianou, Evia Island, Greece. Mineralogy and Petrology 101, 169-183. https://doi.org/10.1007/s00710-011-0144-z

Wang, Q., Yang, L., Zhao, H., Groves, D.I., Weng, W., Xue, S., Li, H., Dong, C., Yang, L., Li, D., Deng, J., 2022. Towards a universal model for orogenic gold systems: A perspective based on Chinese examples with geodynamic, temporal, and deposit-scale structural and geochemical diversity. Earth-Science Reviews 224, 103861. https://doi.org/10.1016/j.earscirev.2021.103861

Wijbrans, J.R., Schliestedt, M., York, D., 1990. Single grain argon laser probe dating of phengites from the blueschist to greenschist transition on Sifnos (Cyclades, Greece). Contributions to Mineralogy and Petrology 104, 582-593.

Wind, S.C., Schneider, D.A., Hannington, M.D., McFarlane, C.R.M., 2020. Regional similarities in lead isotopes and trace elements in galena of the Cyclades Mineral District, Greece with implications for the underlying basement. Lithos 366-367, 105559. https://doi.org/10.1016/j.lithos.2020.105559

Xypolias, P., Iliopoulos, I., Chatzaras, V., Kokkalas, S., 2012. Subduction- and exhumation-related structures in the Cycladic Blueschists: Insights from south Evia Island (Aegean region, Greece). Tectonics 31, TC2001. https://doi.org/10.1029/2011TC002946

Zack, T., Hogmalm, K.J., 2016. Laser ablation Rb/Sr dating by online chemical separation of Rb and Sr in an oxygen-filled reaction cell. Chemical Geology 437, 120-133. https://doi.org/10.1016/j.chemgeo.2016.05.027

Appendix

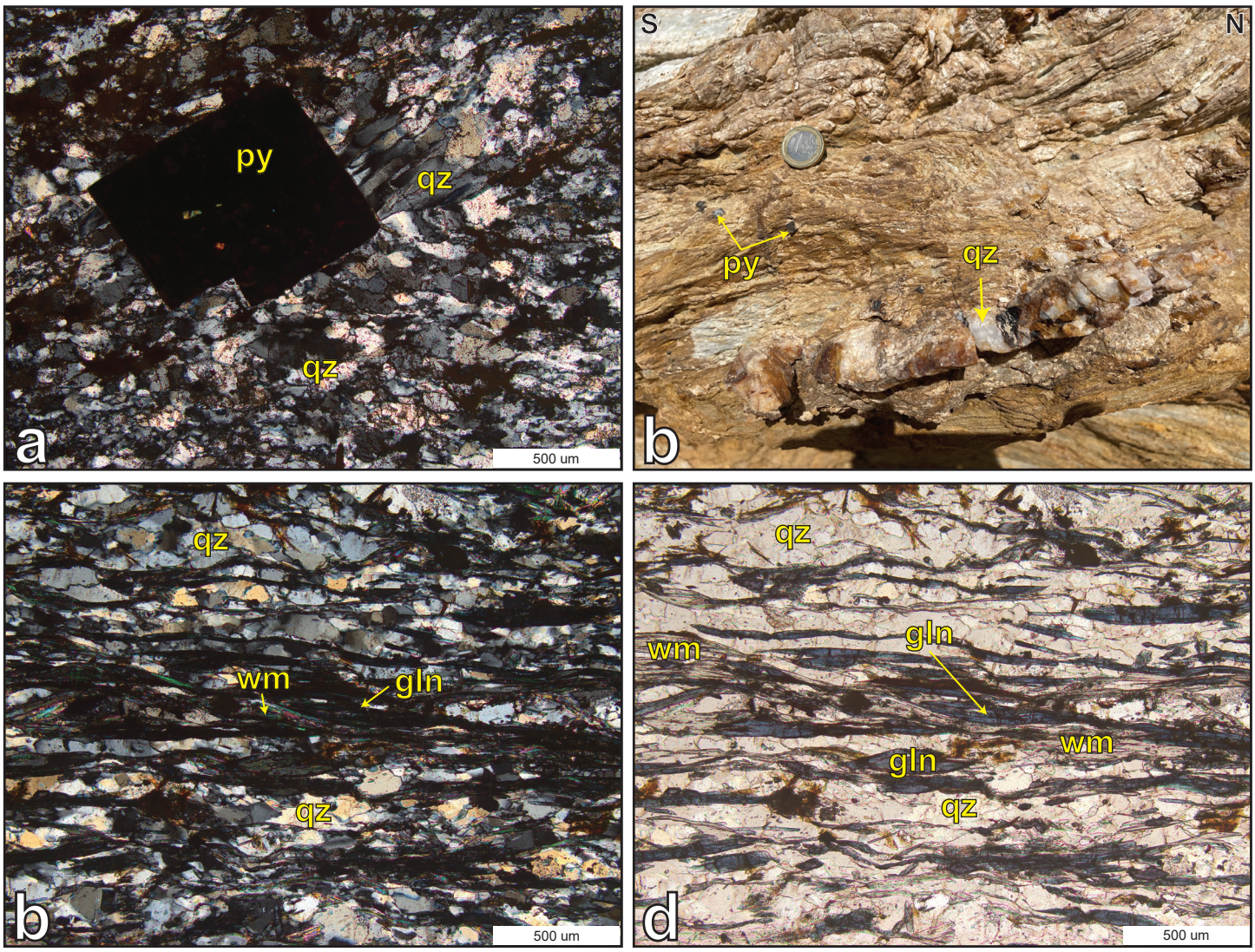

Figure S1. Field photos and photomicrographs adjacent to the NCDS on southern Evia. (a; 288436 E, 4226169 N) Photomicrograph in cross-polarized light of a mineralized cataclastic quartzite adjacent to the NCDS (23-19B). (b, 288436 E, 4226169 N) Field photo of the mineralized cataclastic quartzite block. (c, 288436 E, 4226169 N) Photomicrograph in cross-polarized light of a separate metatuff(?) block within the schist at the NCDS location (23-19C) (d, 288436 E, 4226169 N). Photomicrograph in plane-polarized light of a separate metatuff(?) block within the schist at the NCDS location (23-19C). Abbreviations: gln, glaucophane; py, pyrite; qz, quartz; wm, white mica.

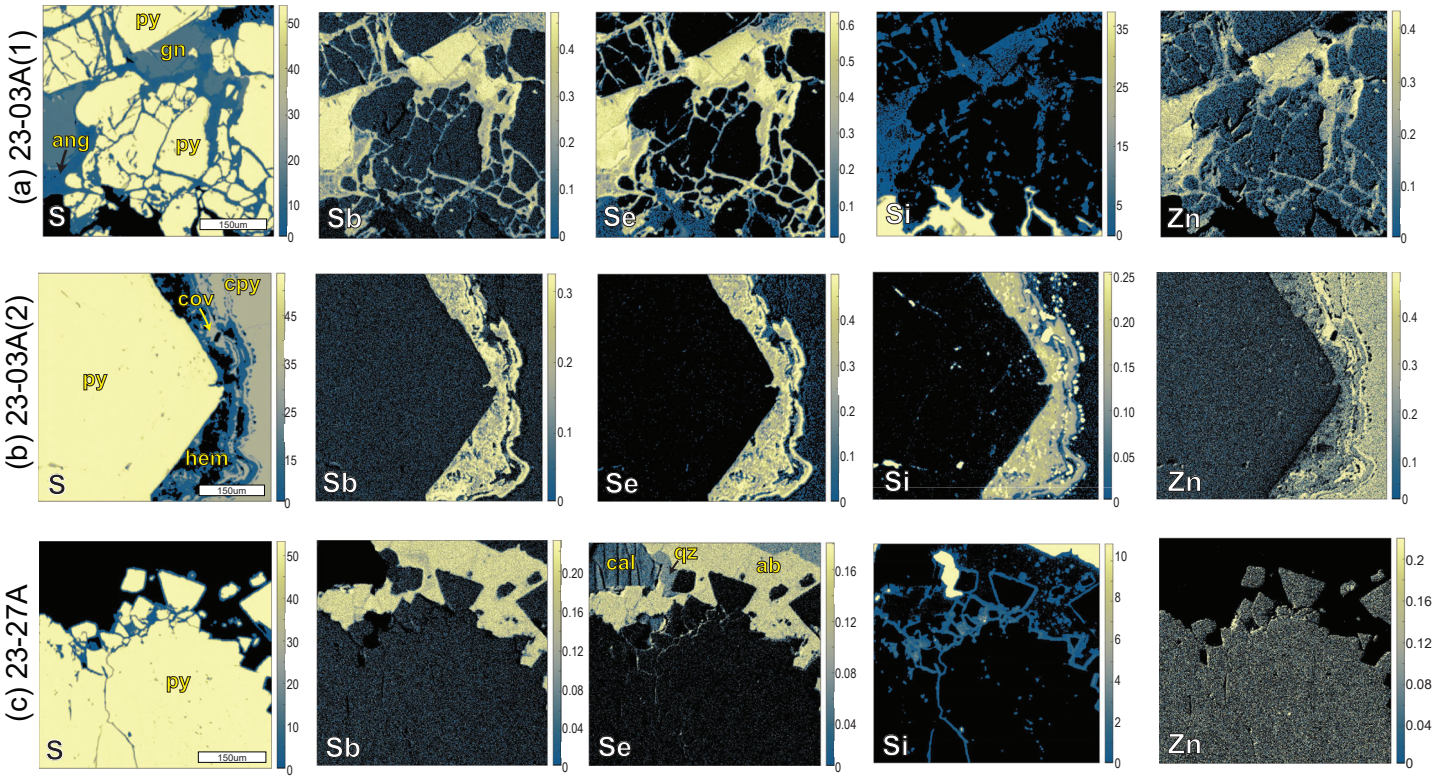

Figure S2. Elemental maps of pyrite grains found in qz ± cal ± ab veins of the Kallianos ore deposit for sample 23-03A and 23-27A for elements S, Sb, Se, Si, Zn. Scale bars are in wt% and black represents areas where element concentrations are below detection limits. Abbreviations: ab, albite; ang, anglesite; cal, calcite; ccp, chalcopyrite; cv; covellite; hem, hematite; qz, quartz; py, pyrite.

Table S1. Analytical results for white mica total fusion $^{40}Ar/^{39}Ar$ geochronology for samples from south-eastern Evia (Greece).

	Sample *Grain*	Age (Ma)	±1σ	^{40}Ar (fA)	±1σ	^{39}Ar (fA)	±1σ	^{38}Ar (fA)	±1σ	^{37}Ar (fA)	±1σ	^{36}Ar (fA)	±1σ	Ca/K	±1σ	Cl/K	±1σ	$\%^{40}Ar^*$	$^{40}Ar^*/^{39}Ar_K$	±1σ
Host rock white mica	**23-03a**	carbonate-mica schist (J: 0.017)																		
	Grain 1	28.8	1.8	2.126	0.034	1.144	0.014	0.070	0.015	0.008	0.013	0.004	0.000	0.048	0.073	0.140	0.039	50.890	0.945	0.059
	Grain 2	24.6	2.0	3.035	0.034	1.048	0.013	-0.001	0.015	0.024	0.013	0.007	0.000	0.153	0.085	-0.042	0.041	27.830	0.805	0.066
	Grain 3	29.4	1.7	1.935	0.029	1.084	0.014	0.002	0.015	0.008	0.013	0.003	0.000	0.046	0.083	-0.031	0.041	54.142	0.966	0.057
	Grain 4	20.3	0.8	2.844	0.030	2.471	0.013	0.037	0.015	0.010	0.014	0.004	0.000	0.027	0.037	0.007	0.017	57.895	0.666	0.026
	Grain 5	23.5	1.0	4.919	0.033	2.745	0.012	0.046	0.017	0.008	0.013	0.009	0.000	0.019	0.033	0.012	0.018	42.963	0.770	0.032
	Grain 6	20.1	1.1	1.818	0.031	1.513	0.013	-0.005	0.015	0.024	0.015	0.003	0.000	0.106	0.064	-0.046	0.029	54.668	0.657	0.038
	Grain 7	19.3	1.2	2.077	0.029	1.602	0.014	0.026	0.016	-0.009	0.013	0.004	0.000	-0.037	0.056	0.011	0.029	48.746	0.631	0.038
	Grain 8	25.8	1.4	2.263	0.032	1.371	0.012	0.003	0.014	-0.001	0.013	0.004	0.000	-0.005	0.065	-0.031	0.030	51.263	0.846	0.046
	23-07a	quartz-mica-epidote schist (J: 0.017)																		
	Grain 1	25.4	0.1	50.505	0.032	55.065	0.017	0.697	0.016	0.287	0.014	0.016	0.000	0.035	0.002	0.001	0.001	90.868	0.833	0.002
	Grain 2	37.4	0.1	39.442	0.036	29.837	0.016	0.402	0.016	0.008	0.015	0.009	0.000	0.001	0.003	0.003	0.002	93.111	1.230	0.003
	Grain 3	32.1	0.1	55.572	0.033	49.013	0.017	0.611	0.016	0.012	0.013	0.013	0.000	0.001	0.002	0.001	0.001	92.781	1.052	0.002
	Grain 4	32.1	0.1	34.681	0.033	30.400	0.017	0.363	0.015	-0.010	0.014	0.009	0.000	-0.003	0.003	-0.001	0.001	92.217	1.052	0.003
	Grain 5	30.0	0.0	88.434	0.038	83.081	0.022	1.037	0.014	0.032	0.013	0.022	0.000	0.002	0.001	0.001	0.000	92.597	0.985	0.001
	Grain 6	30.4	0.1	47.651	0.034	44.495	0.018	0.549	0.017	0.044	0.013	0.011	0.000	0.006	0.002	0.000	0.001	93.267	0.998	0.002
	Grain 7	29.4	0.1	44.074	0.033	40.955	0.017	0.515	0.016	0.032	0.013	0.016	0.000	0.005	0.002	0.001	0.001	89.556	0.963	0.002
	Grain 8	29.6	0.1	47.959	0.036	45.271	0.016	0.574	0.015	-0.006	0.012	0.013	0.000	-0.001	0.002	0.001	0.001	91.773	0.972	0.002
	23-10a	quartz-carbonate-mica schist (J: 0.017)																		
	Grain 1	25.6	0.0	253.249	0.044	262.115	0.029	3.130	0.014	-0.007	0.014	0.095	0.001	-0.003	0.005	-0.001	0.000	88.859	0.857	0.001
	Grain 2	26.4	0.0	177.953	0.044	162.789	0.025	1.967	0.015	0.015	0.011	0.115	0.001	0.009	0.007	-0.001	0.000	80.938	0.884	0.002
	Grain 3	34.1	0.1	95.228	0.034	57.460	0.017	0.716	0.015	0.012	0.014	0.099	0.001	0.021	0.024	0.000	0.001	69.190	1.145	0.005
	Grain 4	24.8	0.1	178.105	0.039	157.597	0.026	1.931	0.015	0.118	0.013	0.161	0.001	0.076	0.008	0.000	0.000	73.438	0.829	0.002
	Grain 5	25.2	0.1	181.897	0.042	157.577	0.023	1.934	0.016	0.077	0.012	0.167	0.001	0.050	0.008	0.000	0.000	72.987	0.841	0.002
	Grain 6	27.8	0.1	96.350	0.039	80.744	0.018	0.982	0.016	0.025	0.012	0.072	0.001	0.031	0.016	-0.001	0.001	78.087	0.930	0.003
	Grain 7	34.4	0.2	99.753	0.037	46.930	0.015	0.572	0.014	0.012	0.014	0.154	0.001	0.025	0.030	-0.002	0.001	54.390	1.154	0.007
	Grain 8	33.0	0.2	93.071	0.034	47.228	0.017	0.607	0.015	-0.026	0.014	0.137	0.001	-0.057	0.029	0.000	0.001	56.256	1.107	0.006
	23-13b	quartz-carbonate-mica schist (J: 0.017)																		
	Grain 1	20.0	0.0	391.368	0.050	547.969	0.051	6.594	0.016	-0.005	0.013	0.077	0.001	-0.001	0.001	-0.001	0.000	94.112	0.671	0.001
	Grain 2	20.4	0.0	316.288	0.046	394.890	0.040	4.792	0.015	0.018	0.013	0.151	0.001	0.002	0.002	0.000	0.000	85.788	0.686	0.001
	Grain 3	20.0	0.1	54.544	0.035	66.482	0.019	0.827	0.015	0.002	0.013	0.033	0.001	0.001	0.010	0.000	0.001	82.163	0.673	0.003
	Grain 4	19.8	0.0	449.072	0.053	628.161	0.051	7.597	0.015	0.042	0.012	0.100	0.001	0.003	0.001	0.000	0.000	93.300	0.666	0.000
	Grain 5	31.5	0.0	231.881	0.044	186.736	0.028	2.270	0.015	0.000	0.013	0.113	0.001	0.000	0.003	0.000	0.000	85.574	1.061	0.002
	Grain 6	20.7	0.0	215.299	0.044	289.927	0.035	3.476	0.014	0.131	0.014	0.044	0.001	0.022	0.002	-0.001	0.000	93.997	0.697	0.001
	Grain 7	20.9	0.0	342.030	0.050	439.610	0.042	5.287	0.015	0.030	0.012	0.110	0.001	0.003	0.001	-0.001	0.000	90.428	0.703	0.001
	Grain 8	21.9	0.0	195.673	0.038	233.579	0.030	2.805	0.013	-0.030	0.014	0.078	0.001	-0.007	0.003	-0.001	0.000	88.061	0.737	0.001
	23-18a	schistose marble (J: 0.017)																		
	Grain 1	23.3	0.3	20.088	0.031	20.370	0.014	0.240	0.014	4.412	0.014	0.044	0.001	10.826	0.036	-0.002	0.002	79.513	0.786	0.011
	Grain 2	24.0	0.1	35.652	0.032	38.521	0.016	0.481	0.016	0.020	0.012	0.015	0.000	0.026	0.016	0.001	0.001	87.389	0.808	0.004
	Grain 3	23.2	0.1	51.155	0.033	48.757	0.016	0.583	0.015	0.011	0.013	0.044	0.001	0.011	0.013	-0.001	0.001	74.680	0.783	0.004
	Grain 4	24.1	0.1	51.419	0.033	51.919	0.016	0.649	0.014	0.002	0.013	0.031	0.001	0.002	0.012	0.000	0.001	82.183	0.813	0.003
	Grain 5	21.6	0.3	11.510	0.032	12.498	0.013	0.191	0.014	0.017	0.013	0.008	0.000	0.068	0.052	0.009	0.003	79.163	0.728	0.011
	Grain 6	26.7	0.1	36.507	0.031	35.813	0.015	0.420	0.014	0.033	0.013	0.014	0.000	0.046	0.019	-0.002	0.001	88.525	0.901	0.004
	Grain 7	25.2	0.1	57.152	0.034	57.372	0.017	0.703	0.014	0.020	0.012	0.028	0.001	0.017	0.010	0.000	0.001	85.470	0.850	0.003
	Grain 8	22.6	0.1	65.694	0.032	62.914	0.019	0.764	0.014	0.118	0.013	0.061	0.001	0.094	0.010	-0.001	0.001	73.066	0.762	0.003
	23-19a	quartz-mica schist (J: 0.017)																		
	Grain 1	32.7	0.0	264.092	0.040	213.682	0.029	2.596	0.015	-0.014	0.013	0.099	0.001	-0.008	0.007	0.000	0.000	88.887	1.097	0.001
	Grain 2	27.9	0.0	121.487	0.035	117.309	0.022	1.443	0.016	-0.016	0.012	0.039	0.001	-0.015	0.012	0.000	0.000	90.441	0.935	0.002
	Grain 3	26.2	0.1	88.025	0.034	86.475	0.020	1.049	0.015	0.040	0.013	0.041	0.001	0.051	0.016	0.000	0.001	86.377	0.878	0.002
	Grain 4	37.9	0.0	292.679	0.046	211.855	0.029	2.542	0.014	0.007	0.012	0.076	0.001	0.003	0.006	-0.001	0.000	92.308	1.273	0.001
	Grain 5	38.6	0.0	328.097	0.049	210.313	0.030	2.559	0.014	0.038	0.013	0.187	0.001	0.020	0.007	-0.001	0.000	83.122	1.295	0.002
	Grain 6	35.2	0.1	116.126	0.037	91.400	0.020	1.117	0.014	0.025	0.011	0.027	0.001	0.031	0.014	0.000	0.000	93.092	1.181	0.002
	Grain 7	31.1	0.0	240.822	0.045	212.875	0.033	2.529	0.014	0.017	0.013	0.064	0.001	0.008	0.007	-0.001	0.000	92.157	1.041	0.001
	Grain 8	25.4	0.1	107.448	0.036	108.642	0.022	1.317	0.014	0.013	0.012	0.050	0.001	0.013	0.013	-0.001	0.000	86.164	0.851	0.002
	23-05a	chlorite schist (J: 0.017)																		
	Grain 1	39.3	0.0	152.660	0.044	108.733	0.026	1.367	0.014	0.082	0.014	0.040	0.000	0.005	0.001	0.001	0.000	92.182	1.294	0.001
	Grain 2	34.5	0.1	53.582	0.035	43.577	0.016	0.553	0.016	0.001	0.013	0.014	0.000	0.000	0.002	0.001	0.001	92.308	1.135	0.002
	Grain 3	36.9	0.0	151.848	0.043	116.677	0.024	1.421	0.016	0.037	0.012	0.035	0.000	0.002	0.001	0.000	0.000	93.216	1.213	0.001
	Grain 4	40.6	0.0	158.093	0.042	109.906	0.026	1.360	0.015	0.011	0.013	0.037	0.000	0.000	0.001	0.000	0.000	92.987	1.337	0.001
	Grain 5	27.9	0.1	43.568	0.033	42.884	0.015	0.516	0.014	0.026	0.013	0.015	0.000	0.004	0.002	-0.001	0.001	90.030	0.914	0.002

	Grain 6	38.0	0.1	85.136	0.035	63.411	0.018	0.788	0.016	0.026	0.013	0.020	0.000	0.002	0.001	0.000	0.001	93.037	1.249	0.002
	Grain 7	42.1	0.1	67.580	0.037	45.172	0.019	0.564	0.016	0.135	0.014	0.017	0.000	0.020	0.002	0.001	0.001	92.763	1.387	0.002
	Grain 8	41.7	0.1	79.893	0.036	54.100	0.017	0.663	0.015	-0.015	0.014	0.019	0.000	-0.002	0.002	0.000	0.001	93.036	1.373	0.002
	23-09a	quartz-mica-schist (J: 0.017)																		
	Grain 1	22.7	0.0	251.271	0.045	305.693	0.036	3.711	0.015	0.028	0.012	0.063	0.001	0.010	0.004	0.000	0.000	92.577	0.760	0.001
	Grain 2	22.3	0.0	108.937	0.036	133.236	0.025	1.629	0.015	0.011	0.013	0.031	0.001	0.009	0.011	0.000	0.000	91.567	0.748	0.001
	Grain 3	19.8	0.0	419.404	0.051	579.081	0.074	7.009	0.015	0.016	0.013	0.121	0.001	0.003	0.002	0.000	0.000	91.417	0.661	0.001
	Grain 4	20.5	0.0	136.803	0.040	184.018	0.026	2.262	0.014	0.020	0.012	0.035	0.001	0.012	0.007	0.000	0.000	92.374	0.686	0.001
	Grain 5	19.4	0.0	93.304	0.036	127.844	0.024	1.549	0.015	0.008	0.012	0.035	0.001	0.006	0.010	0.000	0.000	88.871	0.648	0.001
	Grain 6	21.1	0.0	483.494	0.059	637.160	0.072	7.671	0.016	0.020	0.013	0.108	0.001	0.003	0.002	-0.001	0.000	93.345	0.707	0.000
	Grain 7	20.6	0.0	479.333	0.050	658.047	0.082	7.960	0.016	0.009	0.014	0.088	0.001	0.001	0.002	0.000	0.000	94.507	0.687	0.000
	Grain 8	21.9	0.0	701.057	0.069	909.425	0.192	10.985	0.016	0.057	0.013	0.112	0.001	0.006	0.002	0.000	0.000	95.212	0.733	0.000
	23-15a	quartz-mica schist (J: 0.017)																		
	Grain 1	25.5	0.0	359.265	0.056	390.289	0.072	4.757	0.016	0.042	0.012	0.087	0.001	0.011	0.003	0.000	0.000	92.846	0.853	0.001
	Grain 2	24.4	0.0	486.512	0.057	564.183	0.063	6.829	0.016	0.026	0.013	0.085	0.001	0.005	0.002	0.000	0.000	94.745	0.816	0.000
	Grain 3	25.1	0.0	514.647	0.060	572.380	0.066	6.919	0.015	0.019	0.012	0.108	0.001	0.003	0.002	0.000	0.000	93.747	0.842	0.001
	Grain 4	25.5	0.0	308.295	0.042	322.262	0.047	3.924	0.014	-0.013	0.013	0.109	0.001	-0.005	0.004	0.000	0.000	89.442	0.854	0.001
	Grain 5	25.5	0.0	498.878	0.054	534.786	0.059	6.493	0.016	0.018	0.013	0.138	0.001	0.003	0.003	0.000	0.000	91.742	0.855	0.001
	Grain 6	25.8	0.0	335.762	0.051	362.938	0.047	4.390	0.015	0.008	0.013	0.074	0.001	0.002	0.004	0.000	0.000	93.387	0.863	0.001
	Grain 7	25.7	0.0	598.740	0.063	649.720	0.094	7.872	0.017	-0.005	0.012	0.126	0.001	-0.001	0.002	0.000	0.000	93.696	0.862	0.001
	Grain 8	25.3	0.0	639.831	0.065	677.165	0.098	8.251	0.015	0.017	0.013	0.218	0.002	0.002	0.002	0.000	0.000	89.844	0.848	0.001
	23-22a	chlorite-mica schist (J: 0.017)																		
	Grain 1	24.5	0.0	414.788	0.050	477.193	0.045	5.738	0.016	0.030	0.012	0.074	0.001	0.006	0.003	-0.001	0.000	94.648	0.822	0.001
	Grain 2	24.8	0.0	159.999	0.038	174.100	0.027	2.075	0.016	0.021	0.013	0.052	0.001	0.012	0.008	-0.001	0.000	90.354	0.829	0.001
	Grain 3	23.1	0.0	286.503	0.047	348.320	0.039	4.196	0.015	0.042	0.014	0.056	0.001	0.012	0.004	-0.001	0.000	94.239	0.774	0.001
	Grain 4	29.2	0.0	286.392	0.045	258.054	0.033	3.119	0.015	-0.001	0.013	0.113	0.001	-0.001	0.005	-0.001	0.000	88.254	0.978	0.001
	Grain 5	23.2	0.0	492.253	0.056	595.616	0.054	7.193	0.016	0.003	0.012	0.095	0.001	0.000	0.002	0.000	0.000	94.212	0.778	0.000
	Grain 6	30.2	0.0	348.771	0.045	314.703	0.040	3.804	0.015	-0.005	0.014	0.099	0.001	-0.002	0.005	-0.001	0.000	91.572	1.013	0.001
	Grain 7	28.6	0.0	606.887	0.058	590.691	0.086	7.139	0.016	0.032	0.013	0.135	0.001	0.005	0.002	-0.001	0.000	93.391	0.958	0.001
	Grain 8	22.7	0.0	569.133	0.060	706.168	0.179	8.548	0.017	0.035	0.013	0.106	0.001	0.005	0.002	0.000	0.000	94.416	0.760	0.001
	23-23b	quartz-mica schist (J: 0.017)																		
	Grain 1	25.9	0.0	482.958	0.054	479.555	0.086	5.882	0.016	0.028	0.013	0.226	0.001	0.006	0.003	0.000	0.000	86.125	0.866	0.001
	Grain 2	22.4	0.0	273.549	0.045	312.511	0.040	3.824	0.015	0.124	0.013	0.132	0.001	0.042	0.004	0.000	0.000	85.841	0.750	0.001
	Grain 3	22.2	0.0	232.954	0.040	270.324	0.041	3.300	0.015	0.021	0.012	0.106	0.001	0.008	0.005	0.000	0.000	86.480	0.744	0.001
	Grain 4	23.1	0.0	281.979	0.045	317.278	0.047	3.829	0.014	0.145	0.013	0.122	0.001	0.048	0.004	-0.001	0.000	87.317	0.775	0.001
	Grain 5	21.9	0.0	279.315	0.041	345.914	0.040	4.191	0.015	0.136	0.013	0.088	0.001	0.041	0.004	0.000	0.000	90.812	0.732	0.001
	Grain 6	31.1	0.0	461.953	0.056	393.141	0.047	4.807	0.015	0.011	0.012	0.171	0.001	0.003	0.003	0.000	0.000	89.007	1.044	0.001
	Grain 7	21.1	0.0	190.313	0.044	223.744	0.035	2.748	0.016	0.038	0.012	0.109	0.001	0.018	0.006	0.000	0.000	83.105	0.706	0.001
	Grain 8	24.2	0.0	321.537	0.048	349.332	0.043	4.264	0.014	0.013	0.013	0.128	0.001	0.004	0.004	0.000	0.000	88.134	0.810	0.001
	23-28a	quartz-chlorite-mica schist (J: 0.017)																		
	Grain 1	21.8	0.2	232.177	0.042	124.633	0.023	1.618	0.015	0.016	0.012	0.478	0.002	0.013	0.011	0.000	0.000	39.173	0.729	0.005
	Grain 2	30.3	0.1	123.921	0.040	110.684	0.023	1.340	0.016	0.094	0.012	0.039	0.001	0.090	0.012	-0.001	0.000	90.916	1.016	0.002
	Grain 3	26.2	0.0	150.124	0.036	159.613	0.028	1.900	0.015	0.027	0.013	0.033	0.001	0.018	0.009	-0.001	0.000	93.489	0.878	0.001
	Grain 4	26.2	0.1	95.314	0.039	97.794	0.022	1.198	0.015	0.220	0.014	0.035	0.001	0.241	0.015	0.000	0.000	90.129	0.877	0.002
	Grain 5	26.4	0.0	171.451	0.039	173.621	0.026	2.129	0.015	0.539	0.013	0.066	0.001	0.333	0.008	0.000	0.000	89.853	0.886	0.002
	Grain 6	25.2	0.1	68.102	0.035	62.739	0.018	0.741	0.015	0.180	0.012	0.054	0.001	0.309	0.021	-0.002	0.001	77.768	0.843	0.003
	Grain 7	25.4	0.0	139.507	0.045	151.542	0.029	1.815	0.016	0.099	0.013	0.036	0.001	0.070	0.009	-0.001	0.000	92.670	0.852	0.001
Vein-proximal white mica	*Grain 8*	25.2	0.1	171.145	0.037	172.384	0.026	2.122	0.015	0.161	0.013	0.089	0.001	0.100	0.008	0.000	0.000	84.975	0.842	0.002

Table S2. Analytical results for zircon (U-Th)/He geochronology for samples from south-eastern Evia (Greece).

Sample *Grain*	Corrected Date (Ma)	2σ	Length measurment 1 (µm)	Width 1 measurment (µm)	Length 2 measurment (µm)	Width 2 measurment (µm)	Ft	Mass (µg)	Effective spherical radius (µm)	Rs (µm)	4He (nmol/g)	±	U (ppm)	±	Th (ppm)	±	Sm (ppm)	±	eU (ppm)	±	Uncorr Date (Ma)	Uncorr date analytic unc. (Ma) 2σ
23-08A	mica schist																					
Grain 1	11.7	0.3	264	134	262	103	0.84	11.9	73.3	73.3	515.91	1.98	212.3	5.6	21.5	4.0	0	0	219.0	32.8	9.8	0.3
Grain 2	9.6	0.4	129	70	127	57	0.71	1.6	39.8	39.8	1503.47	6.01	915.4	38.0	14.3	4.7	0	0	925.5	138.8	6.8	0.3
Grain 3	10.6	0.2	119	61	118	63	0.70	1.4	38.6	38.6	1275.68	5.95	696.4	16.0	74.7	4.3	0	0	719.2	107.9	7.4	0.2
Grain 4	12.4	0.7	140	70	138	76	0.74	2.3	45.1	45.1	1408.61	7.28	589.6	35.1	189.6	6.3	0	0	639.0	95.8	9.2	0.5
23-19A	quartz-mica schist																					
Grain 1	11.9	0.6	110	60	112	79	0.69	1.4	38.7	38.7	504.71	2.67	192.2	13.2	256.9	7.4	0	0	254.7	38.2	8.2	0.4
Grain 2	13.2	0.6	153	72	152	82	0.75	2.8	48.0	48.0	459.46	2.84	155.0	6.4	158.2	31.3	0	0	193.8	29.1	9.9	0.5
Grain 3	14.0	0.9	101	62	100	64	0.67	1.1	36.1	36.1	559.85	2.56	195.6	14.8	211.0	23.0	0	0	247.2	37.1	9.4	0.6
Grain 4	15.9	0.8	103	59	105	53	0.57	0.5	27.1	27.1	734.30	4.99	274.5	16.0	254.6	18.8	0	0	337.1	50.6	9.1	0.4
Grain 5	15.1	0.4	129	64	129	58	0.69	1.6	38.7	38.7	1653.33	6.86	501.5	16.6	648.5	42.8	0	0	659.5	98.9	10.4	0.3

Table S3.1 Analytical results for in situ $^{87}Rb/^{87}Sr$ geochronology from the CBU host rock and vein-proximal white mica

	Analysis	Rb (ppm)	Sr (ppm)	Rb^{87}/Sr^{86}	2σ (%)	Sr^{87}/Sr^{86}	2σ (%)	rho
host rock white mica	07A-1	103.00	3.3	74.50	3.100	0.721	3.300	0.36
	07A-2	95.60	2.1	110.60	2.400	0.755	4.000	0.20
	07A-3	96.70	4.4	52.80	3.500	0.740	3.000	0.23
	07A-4	0.02	420.0	0.00	10.000	0.718	0.990	0.30
	07A-5	99.00	2.5	95.90	3.000	0.742	2.600	0.41
	07A-6	4.61	220.0	0.05	3.200	0.720	1.200	0.50
	07A-7	0.001	330.0	0.00	12.000	0.716	1.000	0.42
	07A-8	93.30	2.9	77.30	3.000	0.741	4.100	0.57
	07A-9	47.20	0.8	143.60	3.600	0.766	7.900	0.23
	07A-10	95.30	1.5	151.40	3.900	0.774	3.300	0.66
	07A-11	94.60	3.2	71.10	3.100	0.759	2.900	0.93
	07A-12	54.70	1.4	91.50	3.600	0.729	4.000	0.32
	07A-13	88.00	1.2	180.00	3.800	0.806	5.200	0.26
	07A-14	83.70	2.2	92.80	3.400	0.764	3.500	0.25
	07A-15	96.30	3.0	77.10	2.500	0.740	3.200	0.16
	07A-16	97.40	2.2	104.80	2.900	0.741	3.400	0.29
	07A-17	95.40	1.1	204.70	3.700	0.809	5.100	0.45
	07A-18	91.90	2.0	111.40	2.500	0.756	3.400	0.42
	07A-19	97.90	3.5	67.40	2.500	0.729	3.100	0.34
	07A-20	87.80	2.8	74.10	2.500	0.735	3.100	0.10
	07A-21	75.70	2.1	86.10	3.200	0.755	4.100	0.51
	07A-22	68.00	1.3	125.50	3.000	0.758	4.100	0.33
	07A-23	83.30	1.2	165.20	3.500	0.775	4.100	0.49
	07A-24	88.20	2.2	94.60	2.500	0.707	3.100	0.22
	07A-25	63.00	1.3	114.10	3.000	0.741	4.600	0.26
	07A-26	95.70	2.3	98.20	3.400	0.764	4.400	0.29
	07A-27	94.90	2.6	88.60	2.000	0.746	3.100	0.16
	07A-28	91.10	2.0	110.60	3.000	0.734	4.400	0.41
	07A-29	93.20	2.3	98.50	2.200	0.750	3.700	0.29
	07A-30	94.60	3.5	64.70	2.400	0.737	3.000	0.22
	07A-31	74.70	1.9	95.10	3.000	0.748	3.500	0.37
	07A-32	89.00	1.2	171.40	2.400	0.778	4.000	0.28
	07A-33	95.70	2.9	80.00	3.300	0.744	2.700	0.38
	07A-34	91.80	3.3	67.00	2.500	0.737	2.600	0.19
	07A-35	90.00	2.4	88.60	2.800	0.732	3.000	0.43
	07A-36	86.10	2.3	90.50	2.400	0.761	2.700	0.15
	07A-37	87.60	2.8	73.90	2.300	0.745	2.800	0.40
	07A-38	87.30	1.3	160.70	3.000	0.771	3.600	0.48
	07A-39	95.80	1.9	122.50	3.000	0.774	3.400	0.22
	07A-40	82.00	0.9	220.90	3.600	0.802	4.100	0.22

07A-41	85.80	2.0	103.30	2.600	0.726	3.000	0.52
07A-42	82.50	1.2	165.50	2.800	0.788	4.300	0.26
07A-43	0.002	7.6	0.01	7.600	0.709	2.100	0.18
07A-44	0.013	400.0	0.00	12.000	0.711	0.820	0.33
07A-45	0.144	310.0	0.00	16.000	0.725	1.800	-0.05
07A-46	0.040	13.0	0.01	16.000	0.716	1.700	-0.07
07A-47	0.082	5.7	0.04	17.000	0.706	3.500	0.05
07A-48	92.00	2.4	90.10	1.900	0.746	2.700	0.62
07A-49	92.80	2.1	107.00	2.500	0.755	3.700	0.20
07A-50	90.90	2.2	98.70	2.600	0.765	3.100	0.27
07A-51	0.01	330.0	0.00	15.000	0.714	1.000	0.42
07A-52	0.00	320.0	0.00	11.000	0.713	0.930	0.05
07A-53	0.23	410.0	0.00	10.000	0.713	0.750	-0.08
07A-54	94.20	3.3	70.20	4.300	0.783	6.400	0.58
07A-55	4.92	920.0	0.01	2.300	0.711	0.860	0.48
07A-56	0.39	480.0	0.00	10.000	0.722	1.700	0.16
07A-57	1.94	400.0	0.01	8.700	0.709	1.100	0.28
07A-58	51.60	9.1	13.91	6.200	0.771	11.000	0.77
07A-59	75.10	2.8	62.30	4.200	0.733	9.200	0.29
07A-60	100.00	1.6	146.50	2.600	0.763	3.800	0.60
07A-61	101.00	1.6	151.00	2.300	0.745	3.600	0.50
07A-62	98.00	1.7	137.20	3.900	0.779	4.200	0.15
07A-63	95.60	2.1	110.00	2.600	0.760	3.700	0.40
07A-64	97.50	2.6	88.50	2.600	0.730	3.000	0.31
07A-65	91.50	2.4	94.10	2.100	0.774	3.300	0.20
07A-66	0.23	8.2	0.07	15.000	0.716	2.000	0.11
07A-67	40.80	1.0	103.50	3.900	0.783	6.000	0.12
07A-68	95.60	2.5	92.60	3.100	0.759	3.900	0.62
07A-69	95.00	2.7	84.30	2.200	0.725	2.900	0.68
07A-70	94.00	2.3	96.70	3.000	0.749	3.400	0.53
09A-1	58.80	0.9	161.90	3.900	0.755	5.100	0.35
09A-2	60.30	1.1	128.70	2.400	0.729	4.000	0.45
09A-3	64.40	0.9	172.00	3.400	0.771	4.600	0.69
09A-4	119.00	4.1	69.90	2.200	0.743	2.500	0.42
09A-5	112.00	5.4	49.30	2.000	0.732	1.900	0.54
09A-6	122.00	5.1	57.80	1.900	0.731	2.200	0.64
09A-7	118.00	7.3	38.46	1.700	0.737	1.700	0.54
09A-8	112.00	8.2	32.13	1.700	0.715	1.900	0.46
09A-9	111.00	5.0	52.90	2.400	0.738	2.400	0.10
09A-10	103.00	6.0	41.10	2.500	0.719	2.200	0.31
09A-11	102.00	3.8	63.10	2.200	0.729	2.400	0.20
09A-12	114.00	4.4	60.80	2.200	0.736	2.300	0.59
09A-13	123.00	5.4	53.30	2.000	0.728	2.100	0.59
09A-14	99.90	5.4	43.90	3.100	0.723	2.900	0.60

vein-proximal white mica	09A-15	114.00	3.4	77.50	2.800	0.746	2.900	0.27
	09A-16	105.00	6.7	37.18	1.800	0.724	2.400	0.63
	09A-17	103.00	4.3	57.10	1.800	0.729	2.300	0.39
	09A-18	115.00	4.7	57.80	2.200	0.728	2.400	0.39
	09A-19	112.00	2.2	119.40	2.800	0.741	2.700	0.41
	09A-20	98.00	1.8	128.00	2.700	0.744	3.700	0.34
	09A-21	96.90	2.6	89.20	2.300	0.737	3.100	0.22
	09A-22	119.00	11.0	24.99	1.700	0.722	1.900	0.47
	09A-23	115.00	5.7	47.78	2.000	0.735	2.500	-0.03
	09A-24	71.00	1.7	98.10	2.900	0.741	3.900	0.26
	09A-25	84.60	3.4	58.60	2.400	0.732	2.000	0.53
	09A-26	115.00	2.1	131.00	3.300	0.798	4.500	0.43
	09A-27	123.00	1.5	190.60	2.600	0.779	4.200	0.33
	09A-28	95.10	1.9	121.30	3.100	0.752	3.100	0.46
	09A-29	98.00	1.1	215.90	2.400	0.777	3.800	0.37
	09A-30	130.00	1.9	167.60	2.900	0.788	4.100	0.39
	09A-31	88.40	2.6	81.10	2.200	0.742	3.000	0.54
	09A-32	126.00	5.7	53.30	3.200	0.737	2.000	0.45
	09A-33	77.00	3.8	48.90	2.100	0.747	2.900	0.57
	09A-34	95.60	5.4	42.52	2.100	0.722	2.300	0.37
	09A-35	85.60	1.8	114.80	3.100	0.736	4.500	0.58
	09A-36	118.00	7.4	38.58	2.000	0.723	1.900	0.51
	09A-37	101.00	4.1	58.30	2.200	0.739	2.500	0.53
	09A-38	108.00	3.5	74.00	2.500	0.741	3.400	0.56
	09A-39	83.70	1.6	128.00	2.400	0.733	3.800	0.54
	09A-40	90.40	2.0	107.40	2.700	0.737	3.100	0.45
	09A-41	111.00	1.2	212.90	3.700	0.773	4.500	0.45
	09A-42	109.00	1.6	163.90	2.500	0.782	3.100	0.19
	09A-43	80.20	1.6	119.90	3.500	0.744	3.900	0.45
	09A-44	122.00	5.3	55.40	2.000	0.726	2.400	0.37
	09A-45	108.00	3.9	66.10	2.800	0.734	2.800	0.39
	09A-46	121.00	1.3	227.70	3.900	0.835	5.100	0.65
	09A-47	109.00	1.5	175.80	2.600	0.751	3.000	0.43
	09A-48	76.70	2.1	85.80	4.400	0.721	3.000	0.11
	09A-49	89.90	4.3	49.80	2.500	0.728	2.800	0.46
	09A-50	96.40	3.5	65.30	2.500	0.729	2.600	0.59
	09A-51	83.40	2.0	99.00	2.400	0.741	3.100	0.39
	09A-52	78.00	1.1	177.40	3.700	0.793	5.300	0.36
	09A-53	95.10	3.1	73.90	2.300	0.736	2.600	0.24
	09A-54	73.80	1.3	136.30	2.500	0.762	3.900	0.35
	09A-55	86.10	3.6	58.10	2.700	0.742	2.800	0.34
	09A-56	105.00	1.0	242.90	3.300	0.812	4.100	0.30
	09A-57	100.00	2.5	94.80	3.000	0.738	3.000	0.30
	09A-58	82.80	3.6	55.00	2.300	0.722	3.400	0.35

	09A-59	100.00	5.8	41.50	2.500	0.726	2.000	0.63
	09A-60	97.40	5.2	44.70	2.300	0.710	2.500	0.41
	09A-61	115.00	2.9	95.80	2.700	0.737	2.300	0.33
	09A-62	95.50	1.7	133.80	3.100	0.733	3.600	0.44
	09A-63	101.00	1.2	197.80	4.100	0.771	4.900	0.64
	09A-64	102.00	1.2	202.30	3.500	0.729	4.500	0.40
	09A-65	113.00	2.2	124.60	3.500	0.746	3.200	0.33
	09A-66	111.00	3.1	84.60	2.800	0.744	3.100	0.64
	09A-67	-0.007	0.7	0.10	14.000	0.645	12.000	0.31
	09A-68	0.013	1.7	0.04	12.000	0.748	7.500	0.12
	09A-69	0.002	5.3	0.01	19.000	0.706	5.900	-0.07
	09A-70	-0.002	0.5	0.11	22.000	0.707	12.000	0.13
	09A-71	0.001	2.5	0.03	25.000	0.739	4.800	0.17
	09A-72	0.015	0.9	0.09	11.000	0.744	9.300	0.10
	09A-74	0.018	940.0	0.00011	8.300	0.711	1.100	0.22
	09A-75	0.024	1200.0	0.00010	7.200	0.719	1.600	0.44
	09A-76	0.006	800.0	0.00008	11.000	0.717	1.500	0.14
	09A-77	0.009	880.0	0.00010	7.600	0.710	1.400	0.09
	09A-78	0.011	1100.0	0.00006	10.000	0.714	1.700	0.18
	09A-79	0.028	700.0	0.00016	8.400	0.711	1.500	0.42
	09A-80	0.012	700.0	0.00012	11.000	0.713	1.600	0.12

Table S3.2 *Reference material data for in situ $^{87}Rb/^{87}Sr$ geochronology.*

Analysis	x (um)	y (um)	Approx Rb ppm	Approx Sr ppm	Rb^{87}/Sr^{86}	2σ (%)	Sr^{87}/Sr^{86}	2σ (%)	rho	Approx Fe ppm	Approx Mg ppm	Approx Ti ppm	Mg#	Ti apfu	Ti in Biotite Temp
G_NIST610-1	78999.7	17656.2	426	520	1.969	1.5	0.7131	1.20	0.47	460	435	458	0.49	0.0089	-
G_NIST610-2	79102.5	17698.9	423	510	1.958	1.5	0.7054	0.91	0.78	456	429	444	0.48	0.0086	-
G_NIST610-3	79205.8	17752.3	427	520	1.969	1.3	0.7118	0.79	0.76	459	432	449	0.48	0.0087	-
G_NIST610-4	79346.4	17787.3	426	520	1.96	1.4	0.7107	0.84	0.79	458	434	459	0.49	0.0089	-
G_NIST610-5	79260.8	17870.1	424	510	1.969	1.5	0.7071	0.90	0.61	458	429	450	0.48	0.0087	-
G_NIST610-6	79136.3	17821.2	427	520	1.963	1.3	0.7109	0.84	0.8	458	437	456	0.49	0.0088	-
G_NIST610-7	79189.1	17904.5	420	510	1.973	1.7	0.7114	0.99	0.72	458	423	446	0.48	0.0086	-
G_NIST610-8	79053.6	17883.4	430	520	1.961	1.4	0.7076	1.00	0.72	458	442	454	0.49	0.0088	-
G_NIST610-9	79265.8	17976.7	428	520	1.967	1.4	0.7071	0.98	0.81	458	432	457	0.49	0.0088	-
G_NIST610-10	79125.8	17989.0	425	520	1.963	1.5	0.7094	0.98	0.81	458	433	443	0.49	0.0086	-
G_NIST610-11	79028.6	17989.5	426	510	1.971	1.7	0.7115	1.00	0.82	458	429	455	0.48	0.0088	-
G_NIST610-12	78933.6	17955.6	425	520	1.96	1.5	0.7095	0.96	0.86	458	433	449	0.49	0.0087	-
G_NIST610-13	78930.8	18060.6	425	510	1.969	1.5	0.7127	1.00	0.88	458	431	456	0.48	0.0088	-
G_NIST610-14	79049.7	18080.1	434	520	1.962	1.7	0.7087	1.00	0.87	458	435	448	0.49	0.0087	-
G_NIST610-15	79161.3	18069.5	422	510	1.966	1.6	0.7084	1.20	0.83	458	430	453	0.48	0.0088	-
G_NIST612-1	90122.5	12604.0	30.3	73	0.924	1.8	0.7115	1.20	0.59	60	52	50	0.47	0.00098	-
G_NIST612-2	90160.9	12749.1	28.6	68	0.938	1.6	0.7132	0.93	0.57	64	50	49	0.44	0.00095	-
G_NIST612-3	90251.4	12800.7	28.9	69	0.932	1.5	0.7149	0.94	0.75	80	50	56	0.38	0.0011	-
G_NIST612-4	90358.6	12776.8	29.1	70	0.932	1.5	0.7137	0.97	0.8	84	51	76	0.38	0.0015	-
G_NIST612-5	90331.4	12867.4	29.1	69	0.933	1.5	0.7118	1.10	0.61	80	52	74	0.39	0.0014	-
G_NIST612-6	90245.9	12927.4	28.5	67	0.934	1.4	0.7096	1.00	0.75	67	49	49	0.42	0.00095	-
G_NIST612-7	90424.8	12917.9	27.6	66	0.917	1.4	0.7053	0.95	0.67	81	49	94	0.38	0.0018	-
G_NIST612-8	90348.6	12978.0	28.4	67	0.933	1.5	0.7073	0.92	0.79	74	49	50	0.40	0.00097	-
G_NIST612-9	90158.6	12942.4	28.7	67	0.935	1.4	0.7081	1.00	0.74	70	50	73	0.42	0.0014	-
G_NIST612-10	90444.1	13003.5	28.5	68	0.916	1.6	0.7054	1.00	0.66	74	50	85	0.41	0.0016	-
G_NIST612-11	90268.0	13020.7	28.5	67	0.926	1.6	0.7099	0.99	0.69	74	49	52	0.40	0.001	-
G_NIST612-12	90365.2	13066.8	29.1	69	0.931	1.7	0.7069	1.10	0.75	62	50	62	0.45	0.0012	-
G_NIST612-13	90279.7	13139.6	28.7	68	0.93	1.6	0.7102	0.98	0.6	63	49	47	0.44	0.00091	-
G_NIST612-14	90390.2	13150.7	29	68	0.921	1.5	0.7071	1.10	0.77	75	51	74	0.41	0.0014	-
G_NIST612-15	90327.5	13238.5	27.3	66	0.922	1.5	0.7106	1.10	0.65	77	48	62	0.38	0.0012	-
Mica Fe-1	66462.3	33924.5	1430	2	1557	3.7	7.37	3.10	0.75	97610	13347	8339	0.12	0.16	484
Mica Fe-2	66494.6	34047.3	1430	1.9	1761	3.5	8.23	3.50	0.81	94451	13311	7871	0.12	0.15	467
Mica Fe-3	66621.6	34076.5	1420	1.9	1680	3.2	7.75	2.90	0.81	89553	12957	7208	0.13	0.14	436
Mica Fe-4	66750.6	34092.1	1380	2	1576	4.0	7.34	3.90	0.84	84210	13132	6885	0.13	0.13	419
Mica Fe-5	66863.0	34104.6	1340	1.8	1653	2.6	7.75	2.40	0.89	82107	12814	6698	0.13	0.13	408
Mica Fe-6	66996.3	34103.5	1300	1.7	1692	3.7	7.80	3.50	0.78	80757	12251	6705	0.13	0.13	408
Mica Fe-7	66925.5	34018.2	1410	2	1586	4.7	7.21	4.50	0.89	92160	13269	7977	0.13	0.15	471
Mica Fe-8	66813.1	34011.9	1410	1.9	1621	3.8	7.68	3.40	0.85	86904	13620	7096	0.14	0.14	431
Mica Fe-9	66691.3	33996.3	1400	2	1588	3.5	7.50	3.40	0.66	88505	13468	7170	0.13	0.14	435
Mica Fe-10	66578.9	33954.7	1500	2.2	1555	4.3	7.55	3.80	0.89	100698	14902	8652	0.13	0.17	495
Mica Fe-11	66528.9	33856.8	1500	2.2	1474	3.4	7.14	2.60	0.82	104149	15760	8787	0.13	0.17	500
Mica Fe-12	66367.6	33853.7	1430	1.9	1610	3.7	7.66	3.30	0.87	97946	14247	7591	0.13	0.15	455
Mica Fe-13	66454.0	33756.9	1500	2.2	1496	3.9	7.10	3.80	0.88	96737	14920	8253	0.13	0.16	482
Mica Fe-14	66577.8	33749.6	1540	2.1	1632	3.5	7.35	3.30	0.67	97823	14839	8666	0.13	0.17	496
Mica Fe-15	66665.3	33854.7	1410	2.1	1475	4.1	7.05	3.50	0.78	91336	13627	7371	0.13	0.14	445
	Primary matrix calibration - 306 ± 2 Ma (MSWD = 1.9, n = 13/15)														
Mica MA1-1	51241.3	15574.0	532	1.8	662	3.5	3.900	4.20	0.16	9555	1834	476	0.16	0.0092	-
Mica MA1-2	51300.0	15707.0	478	1.7	624	3.5	3.790	3.60	0.60	8266	1625	399	0.16	0.0077	-
Mica MA1-3	51409.1	15441.7	484	1.8	610	3.1	3.820	2.70	0.59	8398	1747	426	0.17	0.0082	-
Mica MA1-4	51376.0	15579.7	471	1.7	603	2.5	3.827	2.20	0.74	7983	1699	408	0.18	0.0079	-
Mica MA1-5	51293.4	15826.8	500	1.8	600	3.3	3.730	3.00	0.59	8552	1867	412	0.18	0.0080	-
Mica MA1-6	51419.0	15730.1	568	2.0	651	3.2	3.950	3.30	0.54	9669	2101	465	0.18	0.0090	-
Mica MA1-7	51412.4	15878.0	493	1.8	646	3.5	4.000	2.80	0.70	8604	1791	472	0.17	0.0091	-
Mica MA1-8	51568.5	15831.8	517	1.8	623	3.0	3.758	2.40	0.76	8491	1852	417	0.18	0.0081	-
Mica MA1-9	51555.3	15707.8	511	1.8	613	3.5	3.770	2.80	0.60	8686	1823	433	0.17	0.0084	-
Mica MA1-10	51510.7	15574.8	504	1.8	601	3.1	3.782	2.30	0.48	8625	1851	472	0.18	0.0091	-
Mica MA1-11	51576.0	15458.3	462	1.7	615	3.2	3.880	2.80	0.62	7821	1712	442	0.18	0.0085	-
Mica MA1-12	51635.5	15582.2	485	1.7	614	2.6	3.826	2.40	0.34	8614	1752	419	0.17	0.0081	-
Mica MA1-13	51718.1	15830.9	520	1.8	615	2.9	3.760	2.40	0.49	8545	1846	444	0.18	0.0086	-
Mica MA1-14	51760.2	15639.2	556	1.9	636	2.9	3.756	2.30	0.57	9884	2000	524	0.17	0.0100	-
Mica MA1-15	51715.6	15488.8	520	1.9	609	2.9	3.714	2.00	0.61	9030	1943	483	0.18	0.0093	-
	355 ± 3 (MSWD = 2.2, n = 14/15, intercept = 0.750); expected = ca. 350-360 A. Camacho Pers. Comm.														
Mica Mg-1	30456.5	34227.1	922	13	149.5	4.0	1.843	3.6	0.74	41545	69938	6339	0.63	0.120	526
Mica Mg-2	30560.6	34221.5	921	13	154.2	2.6	1.845	1.9	0.32	38433	65484	5836	0.63	0.110	505
Mica Mg-3	30668.4	34218.7	889	12	157.3	1.8	1.848	1.4	0.62	36996	64305	5254	0.63	0.100	477
Mica Mg-4	30808.8	34294.0	883	13	158.6	2.2	1.859	1.8	0.58	35186	64566	5138	0.65	0.099	479
Mica Mg-5	30678.7	34327.4	910	13	159.8	2.2	1.838	1.4	0.15	36451	68787	5159	0.65	0.100	484
Mica Mg-6	30565.3	34320.9	942	13	153.9	2.5	1.841	1.9	0.56	37437	71284	5486	0.66	0.110	503
Mica Mg-7	30425.8	34325.6	901	13	162.5	2.0	1.844	1.9	0.63	37955	66102	5871	0.64	0.110	510
Mica Mg-8	30344.0	34233.6	893	13	155.0	1.9	1.843	1.5	0.46	35746	66677	5520	0.65	0.110	502
Mica Mg-9	30316.2	34339.5	884	12	155.7	3.4	1.835	1.7	0.78	34572	63598	4856	0.65	0.094	461
Mica Mg-10	30338.5	34467.8	851	12	160.3	2.1	1.872	1.5	0.71	34417	61425	5233	0.64	0.100	480
Mica Mg-11	30454.6	34456.6	810	11	151.5	1.9	1.83	1.7	0.36	32976	61127	5180	0.65	0.100	483
Mica Mg-12	30568.0	34455.7	889	12	160.4	2.4	1.829	1.4	0.45	38151	65231	5314	0.63	0.100	479
Mica Mg-13	30687.0	34451.1	941	13	159.8	2.1	1.864	1.7	0.75	37738	69592	5699	0.65	0.110	509
Mica Mg-14	30832.0	34437.1	866	13	151.2	1.7	1.835	1.3	0.36	35144	64947	5583	0.65	0.110	504
Mica Mg-15	30955.7	34427.8	850	12	155.5	2.3	1.844	1.9	0.89	33753	62570	4985	0.65	0.096	471
	512 ± 3 (MSWD = 1.4 n = 13/15, intercept = 0.726); expected = 519 ± 7 Ma Hogmalm et al. 2017														
Mica _MA2-1	44810.0	13924.0	522	2.0	575	4.1	3.620	4.0	0.57	9384	1942	472	0.17	0.0091	-
Mica _MA2-2	44562.2	14059.3	536	2.0	614	3.6	3.730	2.6	0.68	9426	1988	464	0.17	0.0090	-
Mica _MA2-3	44738.5	14141.3	497	2.0	544	2.8	3.662	2.6	0.68	8609	1928	382	0.18	0.0074	-
Mica _MA2-4	44940.1	14036.6	556	2.1	567	3.8	3.580	3.4	0.31	9213	2120	431	0.19	0.0084	-
Mica _MA2-5	44728.0	14016.5	559	2.2	579	3.8	3.700	3.2	0.38	9442	2225	452	0.19	0.0088	-

Mica _MA2-6	44624.2	14262.6	502	1.9	584	4.1	3.660	3.2	0.80	8739	2031	436	0.19	0.0084	-
Mica _MA2-7	44994.0	14212.3	514	2.2	544	2.8	3.707	2.4	0.68	9763	2158	548	0.18	0.0110	-
Mica _MA2-8	44987.0	14385.1	576	2.4	535	2.5	3.604	2.5	0.78	9983	2348	530	0.19	0.0100	-
Mica _MA2-9	44716.5	14510.7	537	2.1	558	3.9	3.560	3.5	0.79	9081	2015	443	0.18	0.0086	-
Mica _MA2-10	44591.7	14460.1	563	2.1	603	3.1	3.687	2.5	0.52	9894	2122	541	0.18	0.0100	-
Mica _MA2-11	44623.2	14370.2	527	1.9	607	2.6	3.750	3.5	0.56	9075	2115	491	0.19	0.0095	-
Mica _MA2-12	44634.5	14617.2	586	2.2	593	3.1	3.660	3.0	0.78	10581	2363	513	0.18	0.0099	-
Mica _MA2-13	44946.9	14486.3	588	2.4	547	3.7	3.667	2.6	0.59	10141	2334	495	0.19	0.0096	-
Mica _MA2-14	44891.9	14572.7	622	2.4	541	2.6	3.629	2.2	0.90	11248	2578	618	0.19	0.0120	-
Mica _MA2-15	44823.0	14667.8	600	2.4	567	2.3	3.623	2.3	0.70	11047	2501	537	0.18	0.0100	-
	355 ± 3 (MSWD = 1.3, n = 10/15, intercept = 0.750); expected = ca. 350-360 A. Camacho Pers. Comm.														
Mica_1B-1	88229.1	21901.0	187	5.3	85.7	2.0	1.851	2.3	0.34	49229	69231	1815	0.58	0.035	-
Mica_1B-2	88324.2	22022.5	194	6.1	76.7	2.9	1.756	2.5	0.66	49893	68534	1732	0.58	0.034	-
Mica_1B-3	88240.7	22137.3	183	5.8	74.0	2.7	1.758	2.1	0.56	47712	67702	1614	0.59	0.031	-
Mica_1B-4	88069.7	22181.9	179	4.9	85.2	2.7	1.983	2.7	0.88	44832	66910	1564	0.60	0.030	-
Mica_1B-5	87958.1	22129.1	198	4.7	100.8	2.5	2.175	2.8	0.76	48168	71998	1788	0.60	0.035	-
Mica_1B-6	88557.0	21691.9	182	6.9	64.1	2.1	1.629	2.7	0.28	47013	69419	1711	0.60	0.033	-
Mica_1B-7	88381.8	21691.9	173	6.3	66.6	1.9	1.670	2.5	0.76	47248	70535	1753	0.60	0.034	-
Mica_1B-8	88751.4	21591.9	172	6.3	65.7	2.2	1.654	2.4	0.52	42254	65685	1596	0.61	0.031	-
Mica_1B-9	88884.4	21676.2	180	6.8	64.3	2.2	1.587	1.9	0.85	46664	66330	1563	0.59	0.030	-
Mica_1B-10	88757.2	21702.6	192	6.9	67.8	2.7	1.674	2.0	0.63	48937	70390	1827	0.59	0.035	-
Mica_1B-11	88728.3	21881.1	193	6.7	69.9	3.3	1.647	3.0	0.72	51659	73698	1844	0.59	0.036	-
Mica_1B-12	88774.6	22016.6	180	5.5	78.5	2.3	1.746	1.9	0.60	45908	65415	1528	0.59	0.030	-
Mica_1B-13	88627.5	22005.1	180	6.4	68.5	2.6	1.675	3.0	0.63	45330	67424	1754	0.60	0.034	-
Mica_1B-14	88515.9	21841.5	195	7.2	65.1	2.9	1.611	3.8	0.50	50505	75470	1955	0.60	0.038	-
Mica_1B-15	88513.5	22038.1	180	6.2	69.9	2.0	1.692	1.7	0.80	49842	70731	1661	0.59	0.032	-
	994 ± 8 (MSWD = 4.4, n = 14/15, intercept = 0.7035); expected = 990 ± 5 Ma Camacho et al. 2012														
Mica_1O-13	79777.2	12479.8	177	0.35	1220	5.6	16.5	6.6	0.78	47192	69734	4565	0.60	0.088	398
Mica_1O-14	79651.4	12477.6	179	0.35	1234	7.3	17.8	7.4	0.90	50231	70601	5062	0.58	0.098	432
Mica_1O-15	79748.7	12034.6	180	0.33	1359	6.1	19.8	5.2	0.90	51429	71322	4124	0.58	0.080	330
	979 ± 18 (MSWD = 5.5, n = 3/3, intercept = 0.7035); expected = 986 ± 5 Ma Camacho et al. 2020														

Table S4. Analytical results for $\delta^{13}C$ and $\delta^{18}O$ isotopes of veins from the Kallianos deposit

Sample ID	**$\delta^{13}C$**	**$\delta^{18}O$**	**Weight (mg)**
3D	-0.73	-16	0.509
5A	-1.96	-14.66	0.509
6A	-0.58	-15.32	0.492
9A	-0.13	-11.26	0.501
16A	-0.77	-11.92	0.517
16A QCD	-0.72	-11.88	0.492
17A	-3.31	-9.83	0.510
22B	-0.89	-13.18	0.502
23A	0.4	-13.2	0.520
27A	-0.55	-15.58	0.504
*27B**	-	-	0.505

*No peaks

** Blind standard: C-44 (calcite)

δ13C = -1.9, n=2, st.dev.=0.09 Expected value to date: -1.8

δ18O = -21.9, n=2, st.dev.=0.1 Expected value to date: -22.0

Analytical precision (2σ): ± 0.1/ml

Analytical errors: 0.4‰